HOKKAIDO UNIVERSITY

Title	Development of New Electrodeposition Methods for Corrosion Resistive Less-noble Metal Alloy Coatings
Author(s)	佐藤, 祐輔
Degree Grantor	北海道大学
Degree Name	博士(工学)
Dissertation Number	甲第12336号
Issue Date	2016-03-24
DOI	https://doi.org/10.14943/doctoral.k12336
Doc URL	https://hdl.handle.net/2115/61931
Type	doctoral thesis
File Information	Yusuke_Sato.pdf



Hokkaido University Collection of Scholarly and Academic Papers : HUSCAP

Development of new electrodeposition methods for corrosion resistive less-noble metal alloy coatings

卑金属合金耐食性コーティングの

新規電析法の開発に関する研究

北海道大学大学院 総合化学院 総合化学専攻

博士後期課程 3 年

佐藤 祐輔

Table of contents

Abstract

Chapter 1. Background and aim of the study

1.1. Overview

1.1.1. Costs issue related to corrosion of metals

1.1.2. Production and consumption of metal resources

1.2. Theory of corrosion phenomena

1.2.1. Mechanism of corrosion

1.2.2. Definition of coupling potential and current

1.2.2.1. Coupling current in single electrode

1.2.2.2. Coupling current between divided-electrodes

1.3. Type of corrosion

1.3.1. Uniform corrosion

1.3.2. Non-uniform corrosion

1.3.2.1. Atmospheric corrosion

1.4. Galvanized steel

1.4.1. Corrosion inhibition mechanism

1.4.1.1. Sacrificial effect

1.4.1.2. Inhibition by corrosion products

1.4.2. Manufacturing method

1.4.2.1. Hot-dip plating

1.4.2.2. Electrodeposition

1.5. Aim of this study

Chapter 2. Evaluation of localized corrosion on Zn galvanized steel by using 100-multichannel electrode array

2.1. Introduction

2.2. Experimental

2.2.1. Fabrication of 100-multichannel electrode array

2.2.2. Multichannel coupling current measurement system

2.2.3. Atmospheric corrosion test

2.2.4. Data analysis

2.2.5. Microscopic Raman spectroscopy

2.3. Results and discussion

2.3.1. Time series of coupling current map

2.3.2. Time series transition of coupling current on individual electrodes
2.3.3. Areal categorization of the corroding surface
2.3.4. Corrosion process on Zn-coated Fe
2.4. Conclusions
References

Chapter 3. Co-electrodeposition of Al-Zn coatings from an $AlCl_3$-$ZnCl_2$-1-ethyl-3-methylimidazolium chloride ionic liquid bath
3.1. Introduction
3.2. Experimental
3.2.1. Preparation and characterization of an $AlCl_3$-$ZnCl_2$-EMIC ionic liquid bath
3.2.2. Electrochemical experiments
3.2.3. Heat treatment
3.2.4. Characterization of coatings
3.3. Results and discussion
3.3.1. Analysis of ionic liquid
3.3.2. Co-electrodeposition of Al and Zn by potentiostatic polarization
3.3.2.1. Property of electrodeposition
3.3.2.2. Microstructure of coatings
3.3.3. Effect of heat treatment
3.4. Conclusions
References

Chapter 4. Al-Zn co-electrodeposition by a double counter electrode electro-deposition system from an $AlCl_3$-1-ethyl-3-methylimidazolium chloride ionic liquid bath
4.1. Introduction
4.2. Material and methods
4.3. Results
4.3.1. Potential transient
4.3.2. Compositional surface profile in the deposits
4.3.3. Compositional depth profile in the deposits
4.3.4. Effect of charge ratio on atomic composition of deposits
4.3.5. Coulometric efficiency of electrodeposition
4.3.6. Efficiency profile of Zn in the DCPED system

4.4. Discussion

4.4.1. Effects of j_C and r_{WC} on X_{Zn}

4.4.2. Effects of d_{WC} on X_{Zn}

4.4.3 Transport mechanism of metal ions in a stagnant thin electrolyte IL bath

4.5. Conclusions

References

Chapter 5. Summary

Chapter 1. Background and aim of the study

1.1 Overview

1.1.1. Costs issue related to corrosion of metals

Sustaining the modern society has been highly dependent on continuous development both in the sociology and engineering that are supporting the foundation of modern civilization composed of various dynamic system of harvesting, conversion, transportation, distribution, recycling and discard of materials, energy and information. Such complex system has been globally expanded and requires currently huge amount of hardware resources named infrastructure such as arterial railway and highway, freight train, automobiles, marine vessels and airplanes for transportation task.

One of the major materials constructing these hardware has been steel because of its superior properties such as easy-refining, high-strength, long-life, low cost and recyclability. These mechanical and chemical properties can be maintained for long period if they are properly treated. However, many metals can not avoid the degradation issue due to corrosion because their thermodynamically stable state is oxidized state on this planet where oxygen of *ca.* 20% in atmosphere and rich water/moisture can easily cause oxidation reaction of these metals except for noble metals. For example, in case of Japan on 1997, almost 40,000 billion yen was consumed and invested for corrosion-related task including corrosion-resistive paint and surface finishing, development and use of corrosion-resistive materials, chemical and electrical protection of metals, etc. (Joint Research Report on Corrosion Cost in Japan, Japan Association of Corrosion Control and Japan Society of Corrosion Engineering) [1]. Frequent replacement of degraded structures requires quite high cost and metal resources that cannot be afforded even for the advanced countries. Proper maintenance of these structural materials and elongation of their lifetime are therefore quite important issue to maintain the modern society.

Table 1. Corrosion cost calculated based on Uhlig method

表１　Uhlig 方式によって推定した腐食コスト

防食対策の内容	1997年		1975年		1997/1975 比率（倍）
	腐食コスト(億円)	構成比(%)	腐食コスト(億円)	構成比(%)	
表面塗装	22994.6	58.4%	15954.8	62.5%	1.441
金属の表面処理	10135.2	25.7%	6476.2	25.4%	1.565
耐食材料	4432.4	11.3%	2388.2	9.4%	1.856
防錆油	636.8	1.6%	156.5	0.6%	4.069
インヒビター	449.0	1.1%	161	0.6%	2.789
電気防食	216.8	0.6%	157.5	0.6%	1.376
腐食研究費	416.5	1.1%	215.1	0.8%	1.936
腐食調査費	95.6	0.2%	-	0.0%	−
計	39376.9	100%	25509.3	100%	1.544

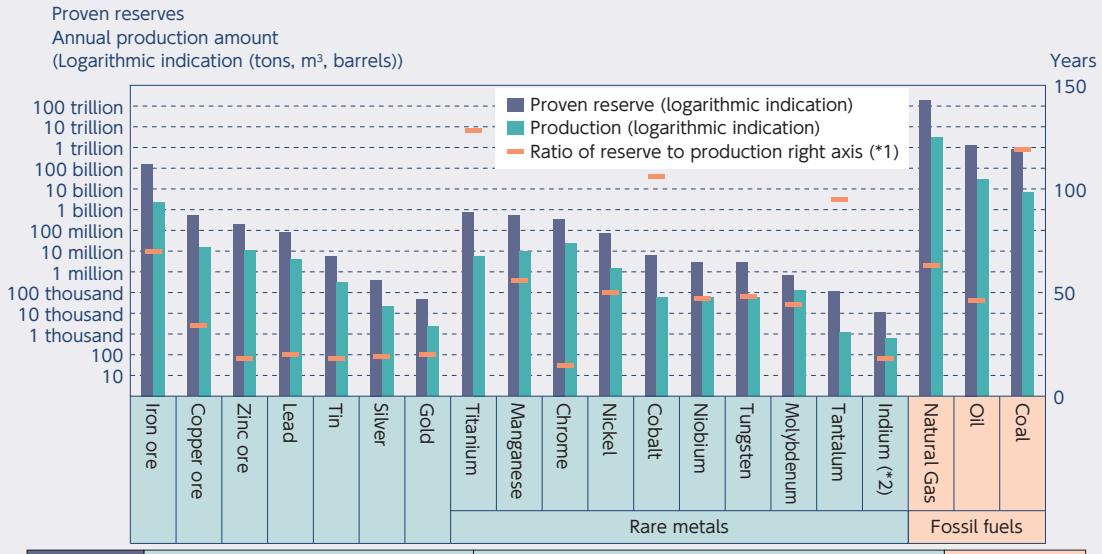
Reprint from "Committee on Cost of Corrosion in Japan, *Zairyo-to-Kankyo*, **50**, 490-512 (2001)"

1.1.2. Production and consumption of metal resources

Depletion of natural resources is an another forthcoming problem. Degradation and failure of social infrastructures must be compensated by fix or replacement of damaged hardware to maintain their functions. These processes consume a lot of natural resources of metals mined as underground mineral resources and are not reproducible. Protection of metal structures from degradation to elongate their lifetime is therefore important strategy. One of typical corrosion protection method for steels that have been mostly applied to structural materials whole in the world has been a coating with corrosion protective zinc layer by means of hot-dip galvanized method because of its moderate operation cost and good adhesivity. Steel is protected from corrosion by slowly corroding Zn coating in practical environment (galvanized steel). Even if the coating is broken by, for example, mechanical damage, substrate steel will be also protected by sacrificial dissolution of Zn layer that can depress electrochemically the corrosion reaction rate of steel. This "sacrificial corrosion protection" technique has also been widely used to protect many marine vessels as large cargo carriers made of steel from corrosion in the corrodible sea water containing aggressive chloride ions. In this operation, metals bars named "sacrificial anode" made of less-noble metals or alloys of Zn Al and Mg is attached to the ship bottom. Dissolution of them during sailing drops the "electrochemical potential" of ship body made of steel (painted, of course) to disable the "anodic dissolution reaction". The sacrificial anodes must be continuously supplied because

the corrosion protection function diminishes when the sacrificial anode dissolved out. The ions dissolved from of sacrificial anodes are dispersed to seawater and uncollectable. The problem comes from the fact that the mineable underground resource of Zn is quite limited. The ministry of the environment, government of Japan, reported that the producible year of mineable reserve of Zn is predicted to be 20 year if the current consumption rate is maintained [2].

Figure 1-2-18 Proven Reserves and Annual Production Amounts (Left Axis, Logarithmic Indication) and Ratio of Reserves to Production (Right Axis) of the World's Main Underground Resources



Major item								Rare metals										Fossil fuels		
Item	Iron ore	Copper ore	Zinc ore	Lead	Tin	Silver	Gold	Titanium	Manganese	Chrome	Nickel	Cobalt	Niobium	Tungsten	Molybdenum	Tantalum	Indium (*2)	Natural gas	Oil	Coal
Ratio of reserves to production(*1)	70	35	18	20	18	19	20	128	56	15	50	106	47	48	44	95	18	63	46	119
Proven(mineral)reserves	160,000	540	200	79,000	5,600	400,000	47,000	730,000	540,000	350	71,000	6,600	2,900	2,800	8,700	110,000	11,000	187,490	1,333	826,000
Production	2,300	15.8	11	3,900	307	21,400	2,350	5,720	9,600	23	1,430	62	62	58	200	1,160	600	2,990	29	6,940
Unit	1 million tons	1 million tons	1 million tons	1 thousand tons	1 thousand tons	Tons	Tons	1 thousand tons	1 thousand tons	1 million tons	1 thousand tons	1 thousand tons	1 thousand tons	1 thousand tons	1 thousand tons	Tons	Tons	1 billion m³	1 billion barrels	1 million tons
Notes	Oxide	Oxide	Oxide	Net	Oxide	Net	Net	Oxide	Oxide	Net	Net	Net	Net	Net	Net	Net	Net			

(*1) The value for ratio of reserves to production is the amount of proven (mineral) reserves divided by the 2009 amount of production. The number of mineable years changes in relation to the confirmed reserves and the amount of production.
(*2) Only for indium, the proven (mineral) reserve is the 2007 value.
Source: Created by the Ministry of the Environment, based on information from the U.S. Geological Survey "Mineral Commodity Summaries 2010"

Reprint from "Ministry of the Environment, Government of Japan, Annual Report on the Environment, the Sound Material-Cycle Society and Biodiversity in Japan 2011,1-1"

Many other metal resources are in the similar situation. Reduction of one-way use of these metal resources is therefore required. To achieve the reduction of Zn use consumed for the corrosion protection, two strategies are considerable. One is an improvement of anti-corrosion performance of Zn coating itself, and the another is alloying of sacrificial anode with the element that is rich in natural resources and possesses the ability to improve

the corrosion protection performance. Pure Zn coating can be dissolved too easily when combined with bare steels due to considerable difference of their redox potentials, *i.e.*, –0.44V for Fe^{2+}/Fe and –0.7628V for Zn^{2+}/Zn. The potential difference between them correspond to the Gibbs energetic difference of their tendency to be oxidized in a given environment. This condition is called "galvanic coupling" in which two different metals are electrically connected. One metal with less-noble redox potential is oxidized (anodic dissolution of Zn; Zn -> Zn + $2e^-$ in the current case) while the other metal (Fe) is forced to be polarized to the less-noble potential more than its redox potential and thus oxidation reaction (Fe -> Fe + $2e^-$) is suppressed (cathodic corrosion protection). In ordinal case, pure Zn is dissolved too much more than the requirement for corrosion protection of steel. Alloying Zn with less-noble Al can improve this problem. For example, typical Zn55Al alloy coating on steels dramatically improved its anti-corrosion performance, *i.e.*, reduction of corrosion loss itself and elongation of coating lifetime. Different property of Zn and Al is thought to be related to the "passivation" property of Zn and "passive" property of Al. Dissolving Zn forms thick surface layer of corrosion products composed of oxide, hydroxide, carbonate, chloride of Zn depending on the environment. This "passivation film" is thick but not dense and thus can not block the transport of ions and species though the film resulting in low corrosion protection performance and continuous dissolution of Zn itself. On the other hand, Al is categorized to be "passive" metal which forms thin and dense surface film in the corrosion process mainly composed of oxide (Al_2O_3 in case of Al) and this passive film can block transport of species and thus suppress the corrosion reaction. However, pure Al coating does not possesses the sacrificial corrosion protection ability for steel because Al does not dissolved with the proper rate necessary to polarize the steel for cathodic corrosion protection. Alloying Zn with Al with proper content combines the proper dissolution rate of coating for corrosion protection performance and longer lifetime.

1.2. Theory of corrosion phenomena

1.2.1. Thermodynamics of corrosion

Corrosion phenomena of metals has been interpreted from the aspect of thermodynamics and kinetics. In the former, phase diagram of metal surface composition in a

electrode potential - pH space so-called "Paurbaix diagram" has been widely accepted by corrosion researcher and engineer in which the most stable metal compound is calculated under the equilibrium condition in a given environment from Gibbs energy of each compound as shown below. Such diagram was calculated for various metals in various aqueous environment and summarized in a book named "Atlas of Electrochemical Equilibria in Aqueous Solutions" published on 1974 by Marcel Paurbaix [3]. Recently many software packages can create the Paurbaix diagram semi-automatically from the database of thermodynamic data. In the case of iron shown below, three typical phases of immune, active dissolution and passive state can be clearly recognized. This approach therefore gives the answer to the question for metals to be or not to be corroded. In a practical scene, however, the corrosion kinetics is more critical because many practical (*i.e.*, not noble) metals are destined to be corroded under the oxidative atmosphere on this planet.

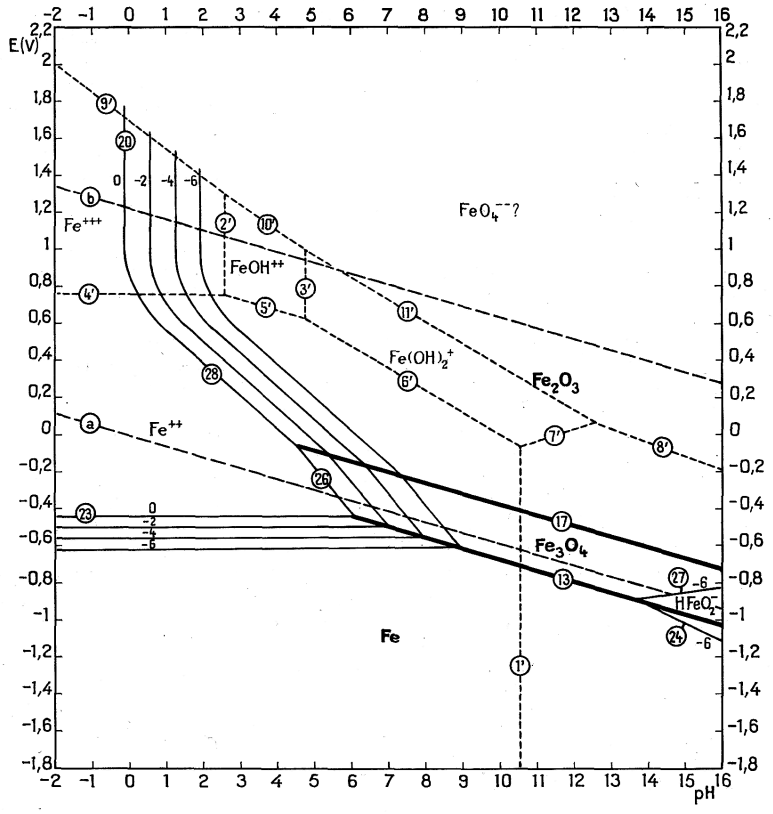


FIG. 3. Potential–pH equilibrium diagram for the iron–water system, at 25°C. (Only solid Fe, Fe_3O_4 and Fe_2O_3 are considered.)

Example of a Pourbaix diagram of iron in aqueous solution. Reprint from "M. Pourbaix, Atlas of Electrochemical Equilibria in. Aqueous Solutions, NACE, Houston, TX. (1974)."

1.2.2. Mechanism of corrosion

Corrosion rate of practical metals is desired to be evaluated to predict their lifetime in the actual conditions. Based on the tons of observation, experiments and knowledge accumulated more than hundred years, corrosion phenomena and their mechanisms have been systematised. A kind of the corrosion mechanism is explained by the "microcell model" based on electrochemical anodic/cathodic reactions on the material surface. In the microcell model, both anodic and cathodic reaction sites, which are generated by non-uniformity on the surface (*e.g.* inclusion, intergranular segregation, stress, welded spot *etc.*) and/or exposed environment (density, pH, temperature *etc.*) distributed on the surface. In anodic site, the electrons are passing from oxidized species to material substrate by oxidation reactions. On the other hand, the electrons are passing from material substrate to reduced species by reduction reactions. Then, the current called "coupling current" is passing from anodic site to cathodic site (opposite to electron flow) via material substrate to maintain electron neutrality (**Fig. 1-2-1**).

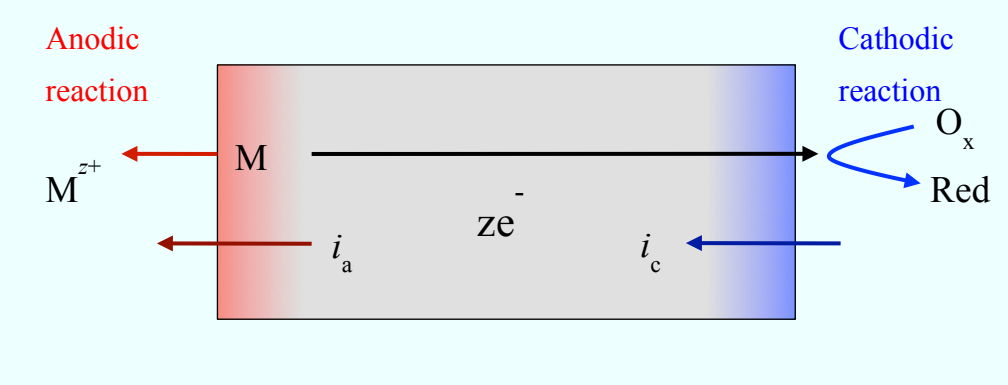


Fig. 1-2-1. Electron flow in individual electrode during corrosion.

1.2.3. Definition of coupling current

The potential of corroded material is explained by concept of coupling potential. Considering the Zn dissolution and hydrogen generation reaction occur at the same single Zn electrode (**Fig. 1-2-2**), the coupling potential and current is defined by following. At the equilibrium potential, both Zn dissolution and deposition take place at the same reaction rate. Likewise, the both hydrogen generation and ionization reaction occur as the same reaction

rate. When the anodic reaction and cathodic reaction, *i.e.* Zn dissolution reaction and hydrogen generation reaction occur at the same time, the steady state is achieved. This point is defined by coupling point, and the potential and current passing through in this situation are defined as coupling potential and coupling current, respectively. Especially in corrosion system, they are so-called corrosion potential, E_{corr}, and corrosion current, i_{corr}.

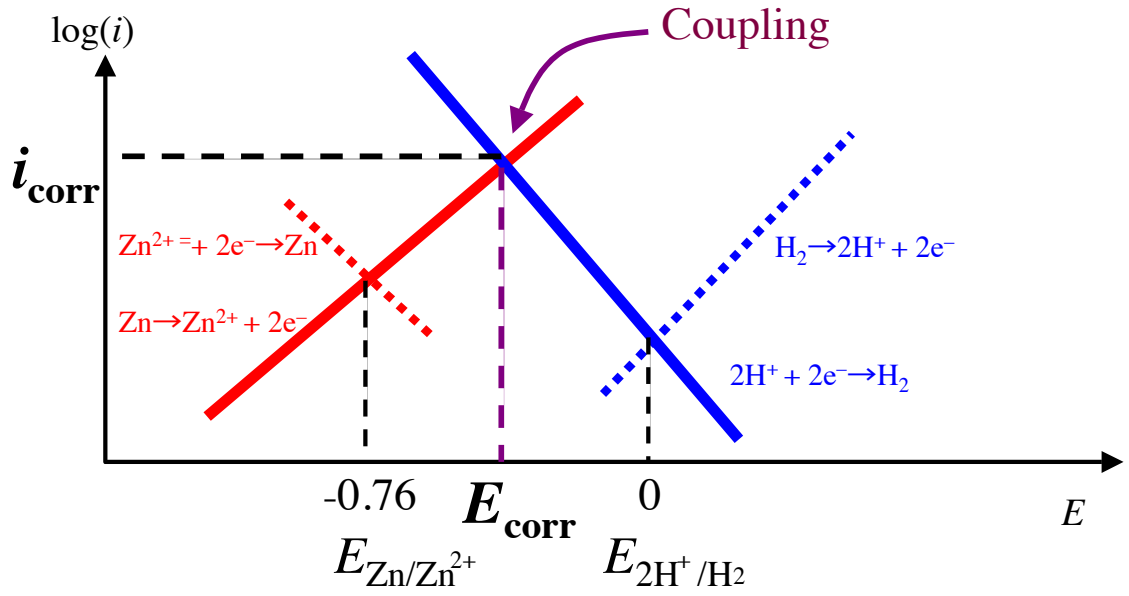


Fig. 1-2-2 An example of coupling of Zn dissolution and hydrogen evolution on individual Zn electrode.

E_{corr} and i_{corr} are quantitatively determined by Tafel equation. **Fig. 1-2-3** shows the E_{corr} and i_{corr} of coupling of iron dissolution and hydrogen generation reactions. In this figure, the E_{corr} and i_{corr} are defined by the cross point of Tafel gradient of anodic current (i_a) and cathodic current (i_c). The Tafel gradients are obtained by following equations;

$$i_a = i_{corr} \exp(\frac{\eta}{\beta_a})$$

$$i_c = i_{corr} \exp(\frac{\eta}{\beta_c})$$

The h is overpotential.

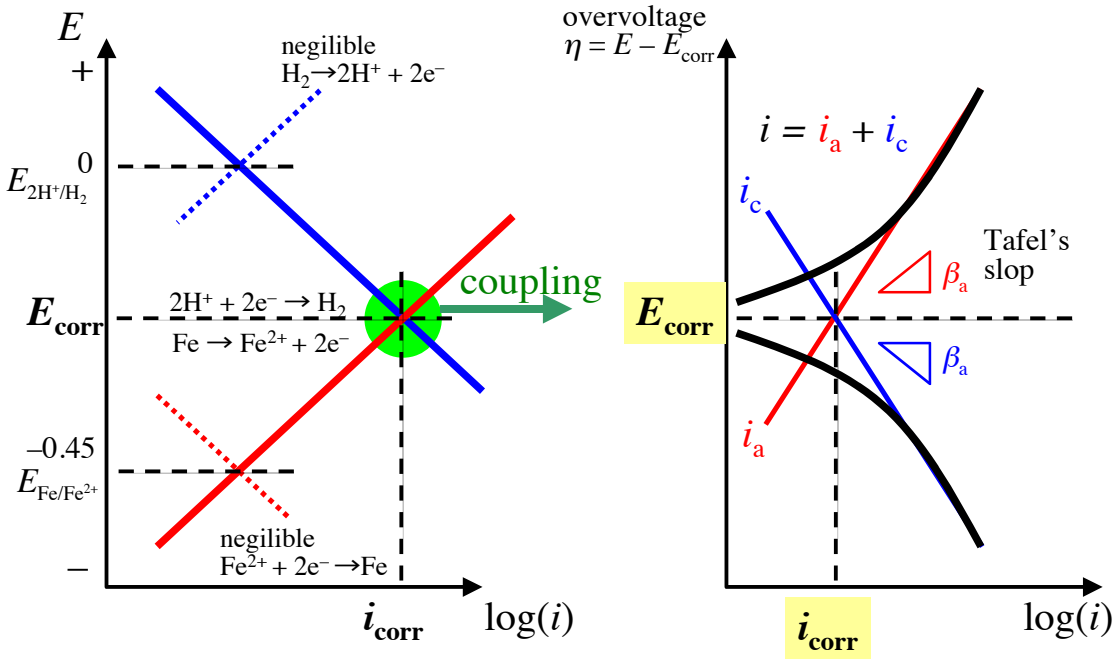


Fig.1-2-3. Decision of E_{corr}, and i_{corr} of Fe by Tafel's low.

To explain priority of reaction in a corrosion system, the concept of mix potential is used. For example, this concept is applied to the system of Fe-Zn corrosion system in aqueous solution (**Fig. 1-2-4**). In the case of no zinc coatings, reaction of iron dissolution and hydrogen evolution reaction are coupled. However, when zinc is exist, the hydrogen evolution reaction couple with zinc dissolution reaction because of its less-noble coupling potential.

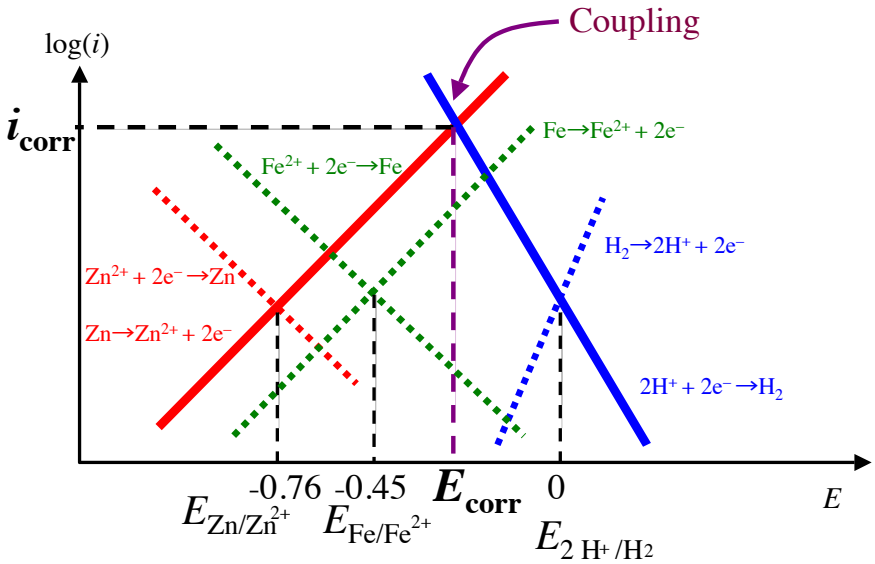


Fig. 1-2-4. An example of sacrificial corrosion protection of Zn for Fe dissolution on individual Fe electrode contacting to Zn.

1.2.4. Coupling current in single electrode

The schematic diagram of coupling current in single electrode is shown in Fig. 1-2-1. When both anodic and cathodic reactions take place simultaneously in corrosion of metal, the dissolution of metal and decomposition of dissolved oxygen or water take place on the metal surface. The anodic and cathodic current, i_a and i_c are displayed by eqs. 1-2-1 and 1-2-2:

$$i_a = z_1 F k_a C_{red} \exp[\frac{-\Delta A_a + \alpha_1 z_1 F(E - E_{corr})}{RT}] = i_{corr} \exp[\frac{\alpha_1 z_1 F(E - E_{corr})}{RT}] \quad (1\text{-}2\text{-}1)$$

$$i_c = z_2 F k_c C_{ox} \exp[\frac{-\Delta A_c - (1-\alpha_2) zF(E - E_{corr})}{RT}] = i_{corr} \exp[\frac{-(1-\alpha_2) z_2 F(E - E_{corr})}{RT}] \quad (1\text{-}2\text{-}2)$$

i_a: anodic current density, i_c: cathodic current density

z_1, z_2: valence of anodic and cathodic reaction, F: Faraday's constant,

k_a, k_c: reaction rate of anodic and cathodic current

C_{red}: concentration of reductant, C_{ox}: concentration of oxidant,

DA_a, DA_c: activation energy of anodic and cathodic reaction,

a_1, a_2: transfer constants of anodic and cathodic reactions,

E: actual potential,

E_{corr}: corrosion potential,

i_{corr}: corrosion current density

In the single electrode system, electrons pass through anode to cathode via electrode. Thus coupling current cannot evaluate.

1.2.5. Coupling current between divided-electrodes

If we can divide anodic and cathodic reaction site, the coupling current can be detected. The schematic diagram of coupling current in divided-electrodes is shown in **Fig. 1-2-5**. In this figure, both anodic and cathodic reaction occurs simultaneously on the same

electrode. However, one electrode is dominated by anodic reaction and other electrodes dominated by cathodic reaction because of the difference of exposed environment and/or non-uniformity of the material. In this case, the difference of anodic and cathodic current, i, pass through as net external current between electrodes (**Fig. 1-2-6**). The net external current can be displayed by Butler-Volmer equation:

$$i = i_a + i_c = i_{corr}\left[\exp\left[\frac{\alpha z F(E - E_{corr})}{RT}\right] + \exp\left[\frac{-(1-\alpha) z F(E - E_{corr})}{RT}\right]\right]$$

When the i_a or i_c is negligible, $i \approx i_C$. Thus the coupling current, i_C, can be detected if the current generated by less-dominant reaction is negligible.

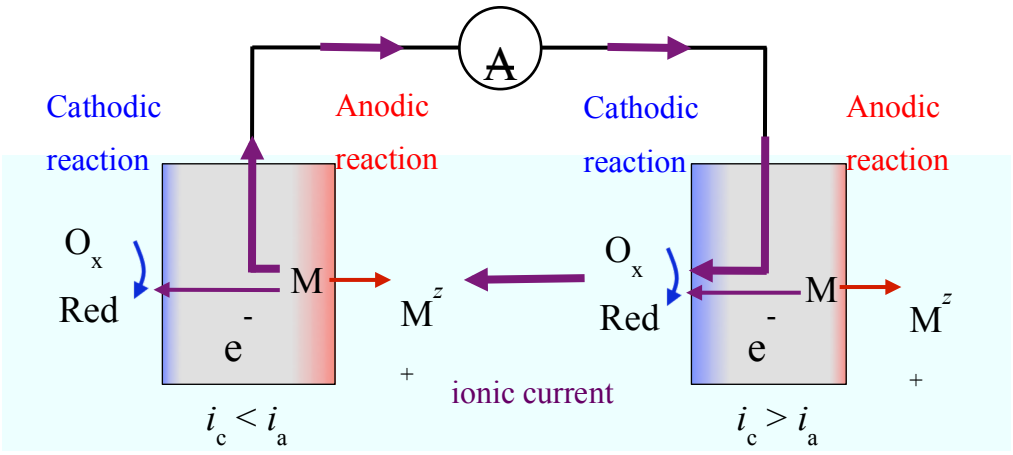


Fig. 1-2-5. Electron flow between divided electrodes during corrosion.

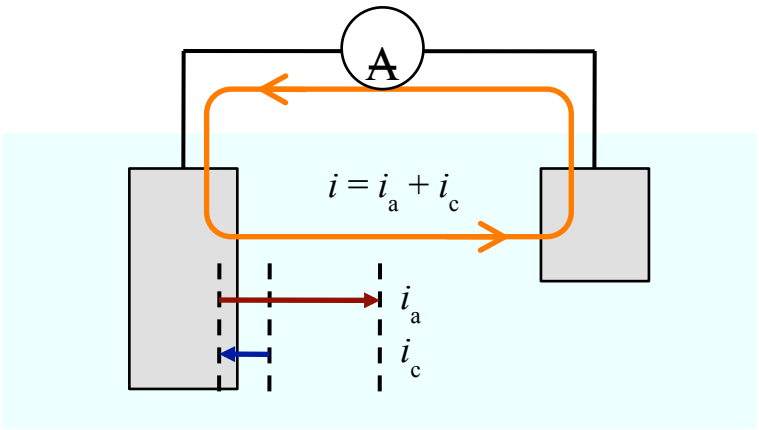


Fig. 1-2-6. Schematic diagram of detected external current.

1.3. Type of corrosion

From the standpoint of spatial distribution of anodic and cathodic reaction, corrosion mechanism can be divided into two types, one is uniform corrosion, and the other is

non-uniform corrosion.

Uniform corrosion

In uniform corrosion, both anodic and cathodic reaction sites occur everywhere on the surface and material is thus corroded uniformly at the same corrosion rate in everywhere. A schematic model of uniform corrosion is shown in **Fig. 1-3-1**. In uniform corrosion, both anode and cathode sites in microcell size distribute uniformly on the surface and their role may switch time by time to each other. For example, corrosion of steel proceeds with dissolution of iron (anodic reaction) and reduction of dissolved oxygen (cathodic reaction) as shown below in acidic and basic aqueous solutions.

Acidic solution:

Anodic reaction: $Fe = Fe^{2+} + 2e^-$

Cathodic reaction: $2H^+ + 2e^- = H_2$

Basic solution:

Anodic reaction: $Fe = Fe^{2+} + 2e^-$

Cathodic reaction: $2H_2O + O_2 + 4e^- = 4OH^-$

In this system, iron dissolves on an anode site but not on a cathode site. Since the location of anode or cathode sites fluctuates with time, corrosion whole on the metal surface proceeds uniformly. In such case, estimation of corrosion rate is rather simple as the weight loss measurement.

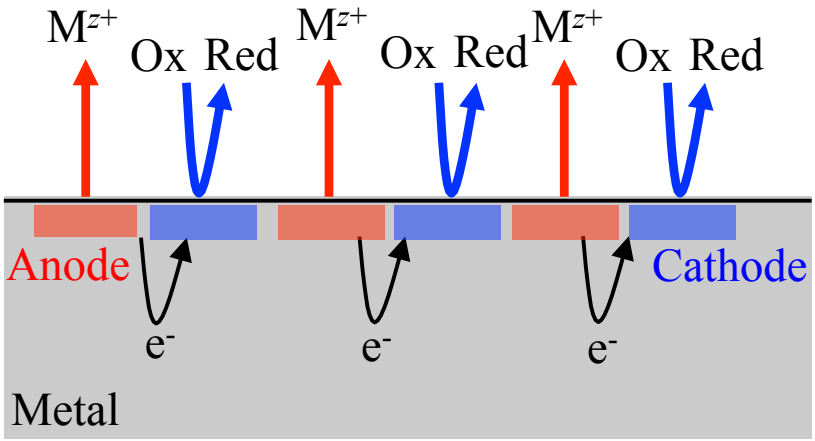


Fig. 1-3-1. Schematic diagram of uniform corrosion.

Non-uniform corrosion

In the corrosion of this type, non-uniformity derived from materials (inclusion, intergranular segregation, stress, welded spot, *etc*.) and from environment (concentration of corrosives, pH, temperature, coatings, *etc*.) can lead the evolution of localized anode or cathode on the metal surface. Evaluation of corrosion progress and lifetime of materials under this non-uniform corrosion is difficult because fatal corrosion such as deep pit and though hole can be progressed on a limited and small (sometimes hidden) anode sites. Evolution of such highly localized corrosion may also evolve in a statistical manner.

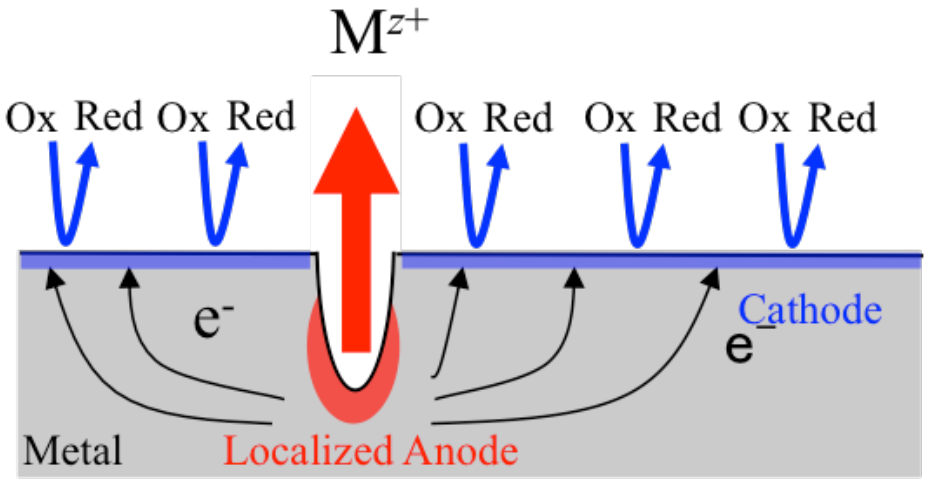


Fig. 1-3-2. Schematic diagram of non-uniform corrosion.

Atmospheric corrosion

The atmospheric corrosion is a kind of corrosion of metals proceeding in the outdoor environment. The outdoor environment contains so many factors such as repetition of daily temperature cycling of high temperature at daytime and low temperature at might, low humidity at daytime and high humidity at midnight to early morning accompanying dew condensation, temporal or seasonal rain and snow, incoming chemicals such as sea salt particles and pollutants, physical damage by collision with sand and pebbles, irradiation with strong UV light inducing degradation of coating paints, *etc*. On the metal surface this water layer may form if relative humidity exceeds some critical level. Thickness of water layer

affects the corrosion rate of metals by changing the diffusion rate of oxygen from water surface to metal substrate, as proposed by Tomashov model shown in **Fig. 1-3-3 [4]**. In this model, corrosion rate is small in region I (dry air), increases with increasing water layer thickness in region II (moist air) and drops in region III (wet air) and IV (immersion). In region II and III, water layer is so thin as diffusion of dissolved oxygen does not limit the corrosion rate. **Fig. 1-3-4** shows the relationship between thickness of water layer and concentration gradient of dissolved oxygen in a thin water layer. Since dissolved oxygen contributes mainly the corrosion rate *via* cathodic reduction reaction of ($2H_2O + O_2 + 4e^- = 4OH^-$), its supply rate from atmosphere to substrate surface through the water layer limits the corrosion rate (diffusion limit). Cathodic current (i_C) of oxygen reduction is thus given by the following equation;

$$i_c = 4FD(C_O / l)$$

where F is the Faraday constant, D is a diffusion coefficient, C_0 is the solubility of oxygen in water, l is a water layer thickness, respectively. The i_C is thus inverse-proportional to the water layer thickness. On the other hand, i_c depends on the water thickness when it becomes less than the thickness of diffusion layer of dissolved oxygen, and displayed by following equation:

$$i_c = 4FD(C_O / h_s)$$

Drop of the corrosion rate in region III and IV in the Tomashov's plot is thus explained by the increase in water layer thickness that lessens the diffusion rate of oxygen.

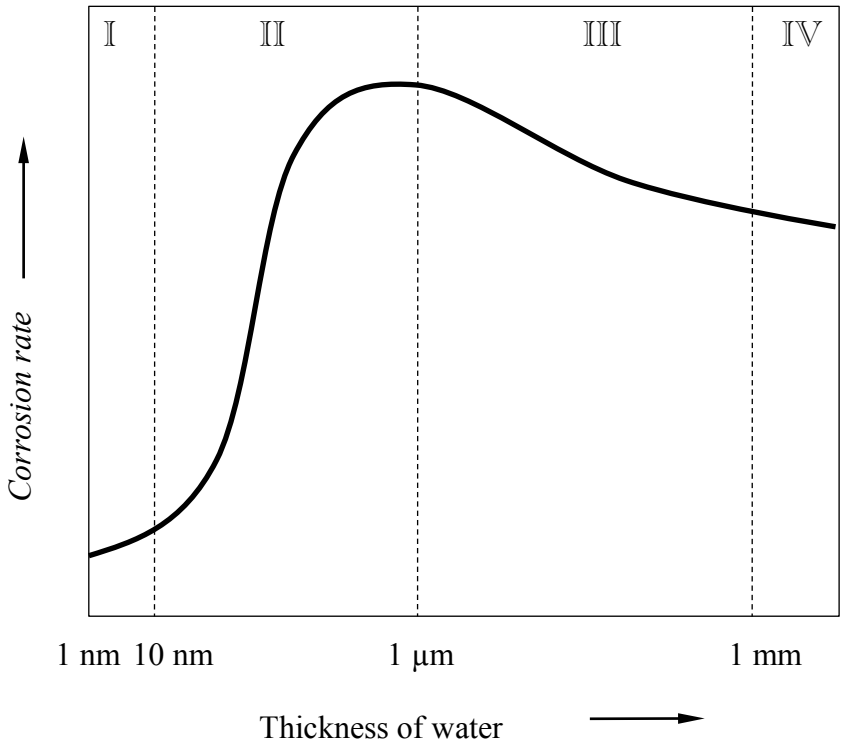


Fig. 1-3-3. Schematic diagram of relationship between corrosion rate and thickness of water layer.

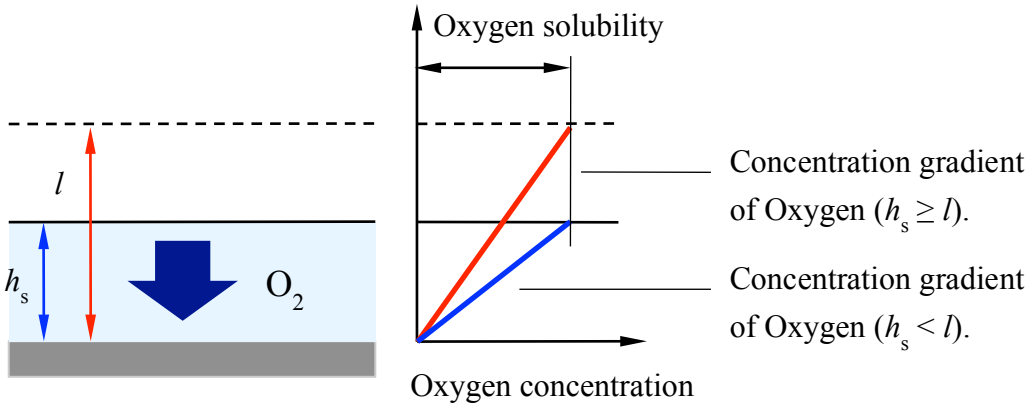


Fig. 1-3-4. Schematic diagram of relationship between water layer thickness and concentration gradient of oxygen.

1.4. Galvanized steel

1.4.1. Corrosion inhibition mechanism

Sacrificial effect

Metal Zn has corrosion protection ability for steel by its less noble redox potential. When substrate steel is exposed to corrosive environment at a cut edge of galvanized steel or scratching, galvanic couple is formed between steel the substrate steel and Zn coating. In this

case, the potential of Zn dissolution is less nobler than that of Fe dissolution. Zn coatings thus preferentially dissolved to protect substrate steel to be cathodic.

Inhibition by corrosion products

Zn corrosion products precipitated on steel substrate also inhibit dissolution of steel. Because zinc is less noble metal, the surface of zinc metal is transformed Zn to zinc oxide (ZnOx). The zinc oxide is insultive material and thus it prevents the surface of steel from the exposed environment, such as aqueous solution and so on[5-10].

1.4.2. Manufacturing method

Hot-dip plating

Hot-dip plating is popular way to manufacture galvanized steel with Zn and its alloy. In this process, the steel is immersed in the molten Zn bath at 460ºC. To manufacturing Al-Zn galvanized steel, the steel is immersed into the molten Al-Zn bath at 570ºC [11-14]. This process causes substrate steel to transform their morphology because of high temperature [15-17]. Furthermore, hot-dip process generate undesirable intermediate Zn-Fe layer between steel substrate and galvanized coating. This intermediate layer lessens adhesion of galvanized coating.

Electrodeposition

Galvanizing Zn coatings also electrodeposited from alkaline and acidic electrolytes. The electrodesposition take advantage of hot-dip coating for the purpose of controlling the morphology, thickness, composition and so on. However, the hydrogen generation reaction simultaneously takes place when metallic zinc is electrodeposited from aqueous solution, e.g. $ZnSO_4$ aqueous solution. This hydrogen evolution causes the defect in the electrodeposits. Thus alternative electrolyte is required to obtain uniform and dense zinc coating layer by electrodeposition. Furthermore, the coating consists of zinc and other less-noble metal, such as aluminum, shows more corrosion resistance because of formation of metal oxide layer [18]. To deposit aluminum containing coatings by electrodeposition, non-aqueous solution must be chosen because of its less-noble deposition potential compared with water decomposition

reaction.

The applicable candidates of alternative electrolytes are molten salt and ionic liquid [19-24]. Especially, ionic liquid bath have advantages compared with aqueous solution for electrodeposition of less-noble metal because of its wide potential window enough to enable electrodeposition of aluminum.

1.5. Aim of this study

In this study, we evaluated corrosion behavior of zinc-galvanized steel by using multi-channel electrode method, which enable to evaluate spatial distribution of anodic and cathodic reaction rate. Then we tried to co-electrodeposit aluminum and zinc form 1-etthil-3-methilimidazolium chloride based ionic liquid bath and heat treatment to control composition and morphology of electrodeposited coatings. Furthermore, we tried to development double-counter electrode method to control the composition of electrodeposited coatings more flexibly than conventional way of electrodeposition.

References

[1] Committee on Cost of Corrosion in Japan, *Zairyo-to-Kankyo*, **50**, 490-512 (2001)

[2] Ministry of the Environment, Government of Japan, Annual Report on the Environment, the Sound Material-Cycle Society and Biodiversity in Japan (2011)

[3] Marcel Paurbaix, Atlas of Electrochemical Equilibria in Aqueous Solutions (1974)

[4] N. D. Tomashov, Atmospheric Corrosion of Metals, Mac millan 367 (1966)

[5] K. Ogle, S. Morel and D. Jacquet, *J. Electrochem. Soc.*, **153**, B1 (2006).

[6] F. Thébault, B. Vuillemin, R. Oltra, C. Allely and K. Ogle, *Electrochim. Acta*, **56**, 8347 (2011).

[7] K. Ogle, V. Baudu, L. Garrigues and X. Philippe, *J. Electrochem. Soc.*, **147**, 3654 (2000).

[8] A.P. Yadav, H. Katayama, K. Noda, H. Masuda, A. Nishikata and T. Tsuru, *Electrochim. Acta*, **52**, 3121 (2007).

[9] J.Izquierdo, L. Nagy, Á. Varga, J.J. Santana, G. Nagy, R.M. Souto, *Electrochim. Acta,* **56**, 8846 (2011).

[10] E. Tada, S. Satoh, H. Kaneko, *Electrochim. Acta,* **49**, 2279 (2004).

[11] T. Prosec, D. Persson, J. Stoulil, D. Thierry, *Corrosion Science* **86** (2014) 231-238.

[12] H.C. Shih, J.W. Hsu, C.N. Sun, S.C. Chung, *Surface Coatings and Technology* **150** (2002) 70-75.

[13] P.R. Seré, M. Zapponi, C.I. Elsner, A.R. Di Sarli, *Corrosion Science* **40** (1998) 1711-1723.

[14] D. Laverde, j.C. Zubillaga, J.G. Sevillano, E. Vilaueva, *Corrosion Science* **37** (1995) 79-87, 89-95.

[15] R. Sagl, A. Jarosik, D. Stifter, G. Angeli, *Corrosion Science* **70** (2013) 268-275.

[16] G.M. Song, T. Vystavel, N. van der Pers, J.Th.M. De Hosson, W.G. Sloof, Acta Mater. **60** (2012) 2973-2981.

[17] S. Prabhudev, S. Swaminathan, M. Rohwerder, *Corrosion Science* **53** (2011) 2413-2418.

[18] C. Leygraf and T. E. Graedel, Atmospheric Corrosion, Electrochemical Society Series, Wiley-Interscience, John Wiley & Sons, Inc., N.Y. (2000).

[19] Q.X. Liu, S. Zein El Abedin, F. Endres, *Surface Coatings and Technology* **201** (2006) 1352-1356.

[20] Y.F. Lin, I.W. Sun, *Electrochimica Acta* **44** (1999) 2771-2777.

[21] J.K. Chang, S.Y. Chen, W.T. Tsai, M.J. Deng, I.W. Sun, Electrochem. Commun. **9** (2007) 1602-1606.

[22] T. jiang, M.J. Chollier Brym, G. Dubé, A. Lasia, G.M. Brisard, *Surface Coatings and Technology* **201** (2006) 1-9.

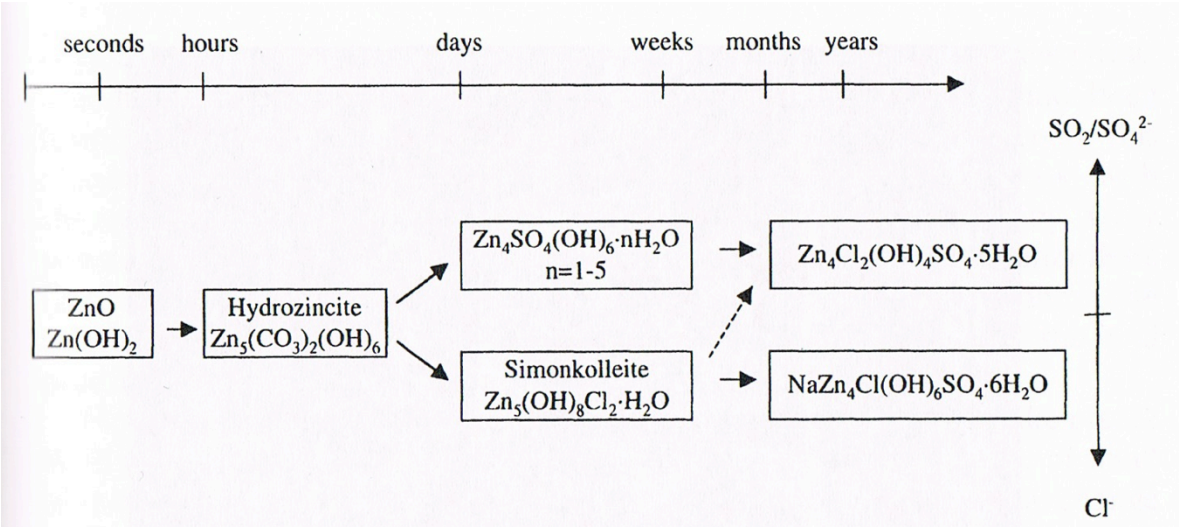
[23] S.I. Hsiu, J.F. Huang, I.W. Sun, C.H. Yuan, J. Shiea, *Electrochimica Acta* **47** (2002) 4367-4372.

[24] S.J. Pan, W.T. Tsai, J.K. Chang, I.W. Sun, *Electrochimica Acta* **55** (2010) 2158-2162.

Chapter 2. Evaluation of localized corrosion on Zn galvanized steel by using multichannel electrode coupling current measurement system

2.1. Introduction

Zn-coated steels have been widely used for various structures and vehicles because of their good anti-corrosion performance. Various kinds of corrosion products are formed on Zn depending on the environment such as zinc oxide, ZnO, zinc hydroxide, $Zn(OH)_2$, basic zinc carbonates such as $ZnCO_3 \cdot Zn(OH)_2$, $2ZnCO_3 \cdot 3Zn(OH)_2$ (hydrozincite, $Zn_5(CO_3)_2(OH)_6$), $ZnCO_3 \cdot 3Zn(OH)_2$, simonkolleite, $Zn_5(OH)_8Cl_2 \cdot H_2O$, and zinc hydrosulfate, $Zn_4SO_4(OH)_6 \cdot nH_2O$ [1]. Even if the Zn coating is accidentally broken by, for example, scratching, the exposed area of substrate steel is cathodically protected by sacrificial anodic dissolution of the Zn coating. It is also expected that the corrosion products of the Zn covering the substrate can suppress the corrosion of substrate steel due to their dense structure, low hydrophilicity and low solubility in water [1-3]. Such a protective function of a Zn corrosion product has, however, not yet been fully clarified.



Reprint from "I. Odnevall, C. Leygraf, *Reaction sequences in atmospheric corrosion of zinc*, W.W. Kirk, H.H. Lawson (Eds.), in *Atmospheric Corrosion*, ASTM STP 1239, American Society for Testing and Materials, Philadelphia (1995)"

Practical corrosion of metals often proceeds in a non-uniform manner due to differences in local conditions such as different oxygen supply and water level, local

deposition of salt, and partial contact with other structures. Visualization of the spatially distributed corrosion progress of metals is thus expected to provide information that will be useful for understanding the corrosion mechanism of Zn coatings. Various *in-situ* imaging techniques have been developed and applied to Zn coatings under the condition of corrosion progress. Ogle *et al.* investigated the relationship between the spatial distribution of ionic current and pH during sacrificial corrosion by using the scanning vibrating electrodes technique (SVET) and pH microelectrodes [2-4]. Yadav *et al.* showed the potential map on Zn-galvanized steel obtained by using a scanning electrochemical microscope [5]. Izquierdo *et al.* revealed the spatial distribution of Zn^{2+} ions by scanning solid contact Zn^{2+} ion-sensing microelectrodes [6]. Tada *et al.* also showed the spatial distribution of Zn^{2+} ions in bulk solution during galvanic corrosion by using a scanning Zn disc electrode [7]. These techniques can visualize the spatial distribution of various parameters such as potential, pH and ionic species on the corroding metal surface immersed in an electrolyte solution or even in atmospheric conditions. However, these techniques, except for SVET, do not enable evaluation or direct visualization of the distribution of anodic current related to the actual corrosion reaction.

In practical corrosion, some of the surface of the metal acts as an anode or cathode depending on its composition or surrounding conditions to form galvanic couples. Coupling current mapping is therefore useful for evaluating the corrosion progress in various practical materials, especially for the case of sacrificial corrosion. Tan *et al.* applied the multiple wire beam electrode (WBE) method to various kinds of wet corrosion to visualize the progress of corrosion [8,9]. Muster *et al*. investigated the effects of size and shape of water droplets on corrosion of Zn [10]. Budiansky *et al.* and Bocher *et al.* applied a multichannel microelectrode analyzer (MMA) to crevice and pitting corrosion of stainless steels [11,12]. Fushimi *et al.* applied the multichannel electrode method to galvanic corrosion on carbon steel welded with type-309 stainless steel [13], and Naganuma *et al.* applied this method to crevice corrosion of steel [14] and to the pitting corrosion of stainless steels used in salt manufacturing plants [15]. In those studies, metal samples were divided into many pieces and reconstructed to reproduce the original shape of the sample, and each piece was used as an individual electrode to measure the coupling current on it to the other electrodes to obtain a coupling current map on

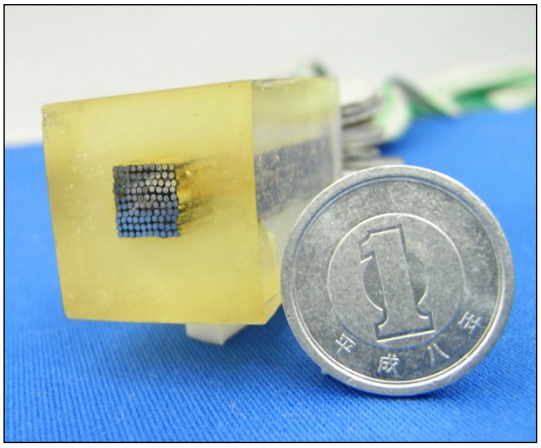
the corroding metals. These coupling current techniques have advantages in simple equipment and applicability to partially immersed system (wet and dry corrosion simulating atmospheric corrosion) and to large corrosion phenomena (relatively low spatial resolution) comparing to, for example, SVET.

In the present study, the coupling current mapping technique was applied to atmospheric corrosion of Fe partly covered with Zn electrodeposits to investigate the anti-corrosion function of the Zn layer in its sacrificial protection of Fe and corrosion inhibition of Fe by the corrosion products of Zn. A specimen of multichannel (100-channel) electrodes composed of a bundle of Fe wires in an arrangement of a 10 x 10 matrix partially electrodeposited with Zn was exposed to a humid atmosphere in a chamber, and the time series of the coupling current map was traced during the progress of corrosion. Raman spectroscopic analysis was also applied to identify the corrosion products formed on individual electrodes.

2.2. Experimental

2.2.1. *Fabrication of 100-channel electrodes array*

The specimen was composed of 100 Fe wires (0.5 mmf, 99.5% in purity, Nilaco Co.) embedded in epoxy resin as shown in **Fig. 2-2-1**. These wires were electropainted individually for electric insulation from each other, bundled in the form of a 10x10 array matrix and fixed in epoxy resin. The specimen was then ground with emery paper (#1000) to expose the cross-section of wires used as an electrode surface. The two-dimensional coordination system to specify the individual electrode is indicated in the figure. The central 4 x 4 electrodes were then electroplated with Zn at –0.1 A cm^{-2} for 300 s in a bath containing 2 mol dm^{-3} $ZnSO_4$ and 0.5 mol cm^{-3} Na_2SO_4 at pH 2. The thickness of the Zn layer was calculated to be *ca*. 28.5 μm from the electrodeposition charge of Q_{dep} = 30 C cm^{-2} with the assumption that the electrodeposition efficiency was 100%.



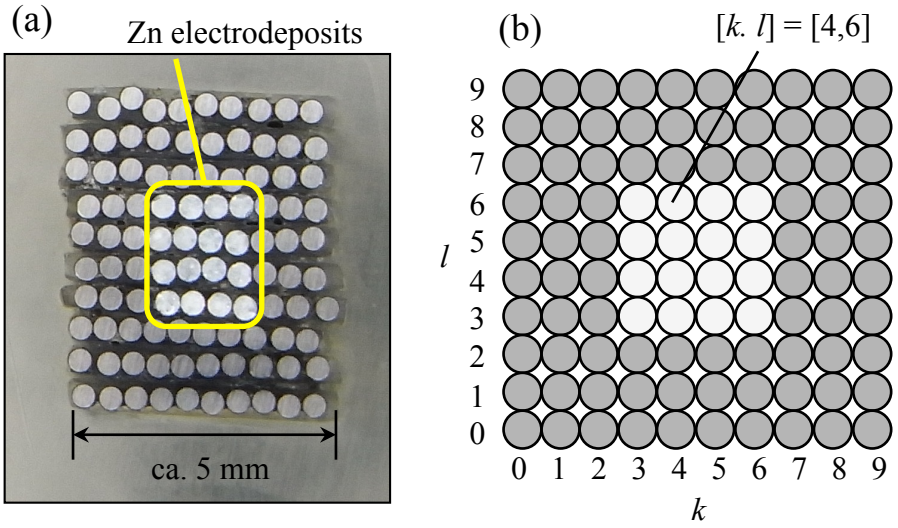


Fig. 2-2-1. (a) Appearance of a specimen composed of a 100-channel electrode array, (b) coordination system of the electrode arrangement.

2.2.2. *Multichannel coupling current measurement system*

The coupling current map was obtained by using a multichannel coupling current measurement system schematically shown in **Fig. 2-2-2**. This system consisted of an array of photo-MOS relays, an operational amplifier (OPA) for current-voltage conversion, a 16 bit analogue-digital converter (ADC) to digitize the coupling current, and a microcontroller (MC) controlling the whole system and communicating with a host personal computer (PC). Each Fe wire electrode was connected to the OPA or common (ground) level of the circuit *via* a low on-resistance photo-MOS relay. In the operation, all electrodes were connected to the common level to enable flow of the coupling current to each other in galvanic corrosion. When the coupling current map was measured, one of the electrodes was chosen and

connected to the OPA *via* a photo-MOS relay to measure the coupling current on it to the other 99 electrodes connected to the common level. The electrode connected to the OPA was scanned sequentially for all electrodes, and the intensity of the coupling current was plotted in an *X*-*Y* plane corresponding to the actual arrangement of the matrix of electrodes.

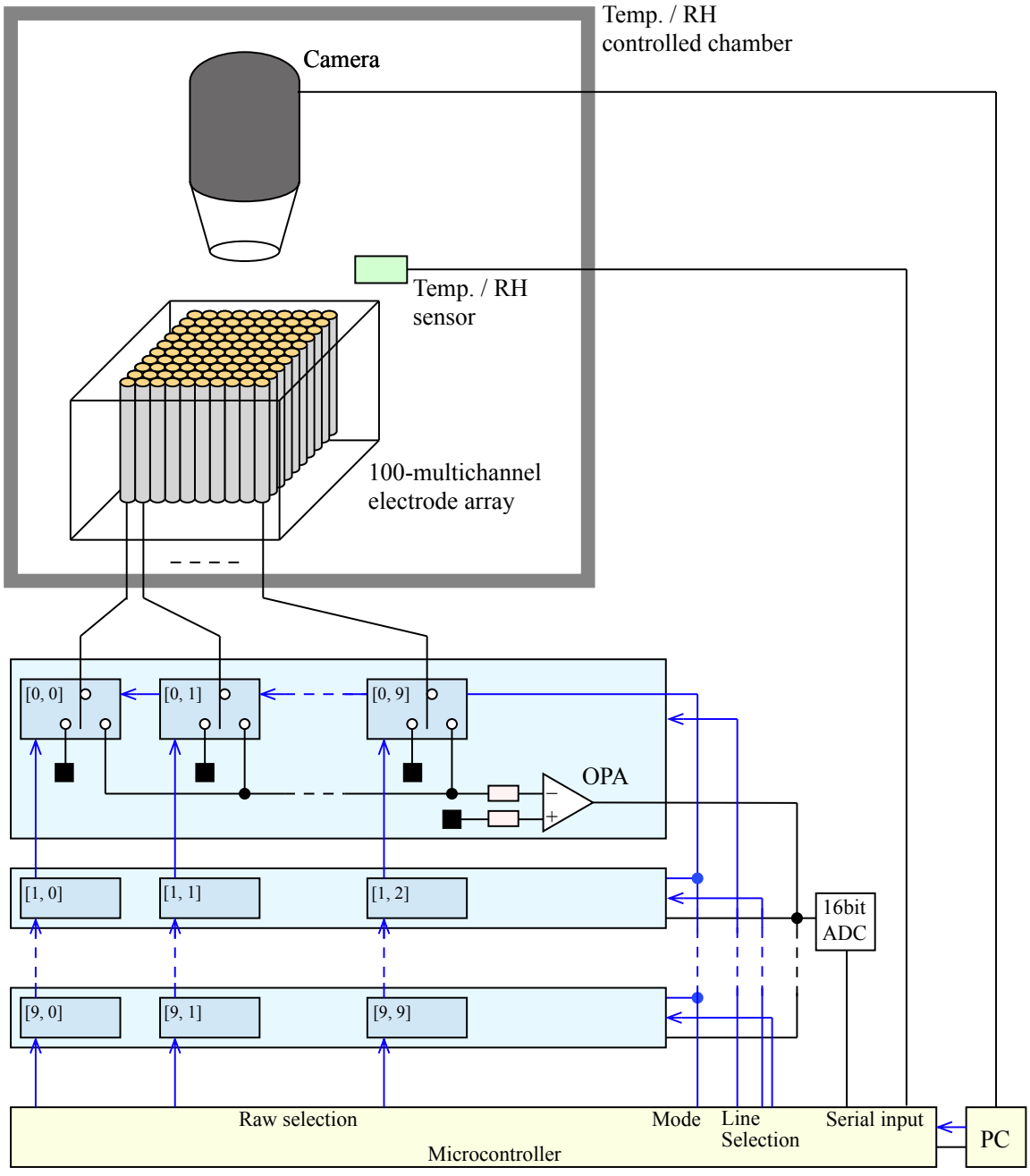


Fig. 2-2-2. Schematic diagram of the 100-channel electrode coupling current measurement system.

2.2.3. *Atmospheric corrosion test*

For the corrosion test simulating atmospheric corrosion, the specimen was put in a temperature and humidity-controlled chamber (Tokyo Rikakikai Co. LTD, ENVIROS KCL-1000) in which the temperature (*T*) and relative humidity (*RH*) were kept at 25ºC and 90%, respectively. To accelerate corrosion, a droplet of 5 mm^3, 3 wt.% NaCl solution was put on the center of the specimen surface. The appearance of the specimen surface was captured sequentially using a digital camera placed in the chamber during the test.

2.2.4. *Calculation of anodic and cathodic coupling current charge*

Although the coupling current is not directly proportional to the actual corrosion rate, they are in a close relationship, especially in a strong galvanic coupling condition as in the case of Zn-coated Fe in the sacrificial corrosion protection condition. The anodic coupling charge calculated from integration of the anodic coupling current is thus expected to correlate with the actual corrosion loss of Zn and Fe. Anodic and cathodic coupling charge densities, Q_a^{cp} and Q_c^{cp}, were calculated for individual electrodes using the following equations (**Fig. 2-3-3**):

$$Q_a^{cp} = \int_{t1}^{t2} i_a^{cp} dt \,, \quad (1)$$

$$Q_c^{cp} = \int_{t1}^{t2} i_c^{cp} dt, \quad (2)$$

where i_a^{cp} and i_c^{cp} are the anodic and cathodic coupling current densities, respectively.

2.5. *Microscopic Raman spectroscopy*

Microscopic Raman spectroscopy was used to determine the composition of corrosion products formed on an individual electrode using a Raman spectrometer (Bunko-Keiki Co., model BRM-300) and a YVO_4 laser (532.0 nm, 100 mW). Raman spectra were averaged for 300 times measurements to reduce noise.

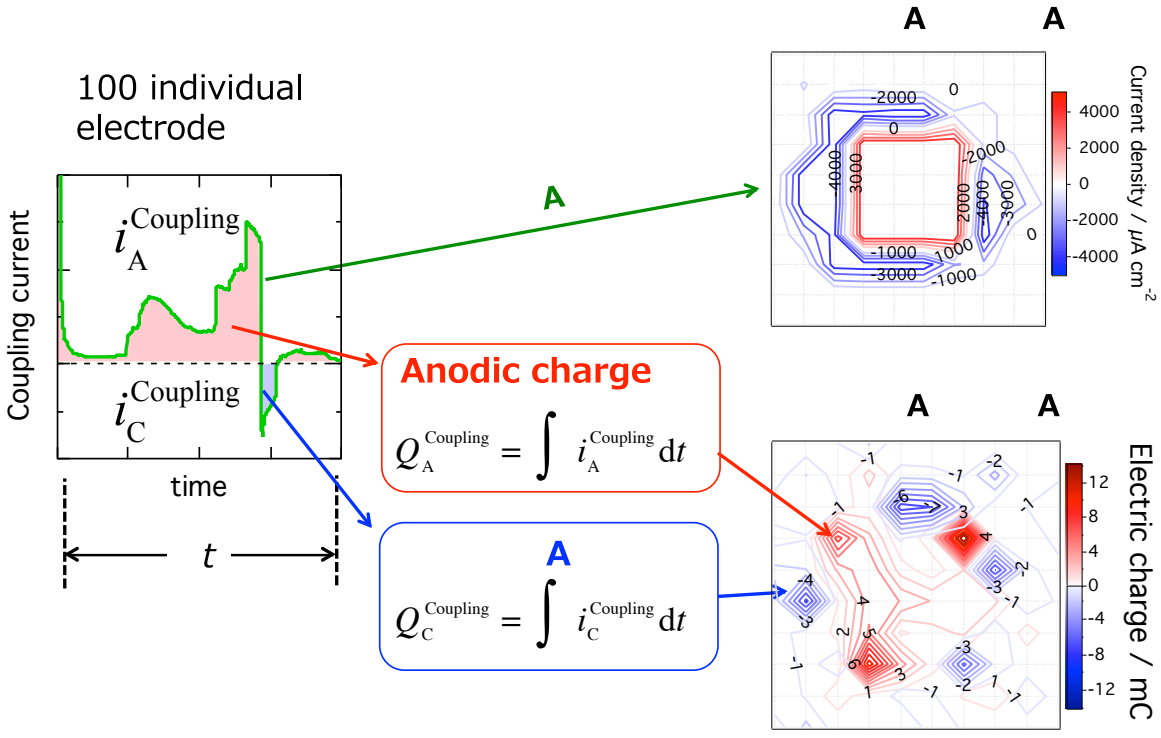


Fig. 2-3-3. Calculation of anodic and cathodic coupling current charge maps.

2.2.3. Results and discussion

2.3.1. *Time series of coupling current map*

An image of the specimen surface composed of 10 x 10 Fe electrodes partially covered with Zn deposits and the corresponding contour map of coupling current i^{cp} measured at the initial stage of the corrosion test are shown in **Fig. 2-3-1-1**. From a comparison of **Fig. 2-3-1-1 (a)** and **(b)**, it was confirmed that the central 4 x 4 Fe electrodes covered with Zn acted as anodes and that the Fe electrodes surrounding the Zn coating acted as cathodes. The shape of the cathodic area in the contour map reflects the border of the NaCl droplet. A large cathodic coupling current was obtained on the bare Fe electrodes in the vicinity of Zn anodes. The intensity of the coupling current was as large as several hundred μA cm^{-2} for each electrode. These results confirm that the 100-channel electrodes system can reveal the area of anodic or cathodic distribution on the corroding metal in a strong coupling condition even in the case of atmospheric corrosion.

Transition of the specimen surface in the progress of sacrificial dissolution of the Zn coating and the corresponding coupling current map are shown in **Fig. 2-3-1-2**. The Zn

coating seems to be preferentially consumed in the vicinity of bare Fe electrodes by sacrificial dissolution. At 5 ks (**Fig. 2-3-1-2 (a) (b)**), a large anodic coupling current was observed, especially at the four corners of the Zn-coated area, due to strong coupling of the Zn-coated electrode with the surrounding bare Fe electrodes. At 108 ks (**Fig. 2-3-1-2 (c) (d)**), the strong anodic area retreated to the center of electrodes, and the four electrodes at the corners of the 4 x 4 central electrodes changed from anodes to cathodes due to complete depletion of the Zn coating. At 154 ks (**Fig. 2-3-1-2 (e) (f)**), only one of the central electrodes showed large i_a^{cp}. At this time, the central area of the sample surface with the size of the initial NaCl solution droplet was covered with a white corrosion product formed by Zn corrosion. Fe rust was observed on the electrodes at the edge of the 10 x 10 electrode matrix after 108 ks because the electrodes were located beyond the sacrificial corrosion protection range by the central Zn coating.

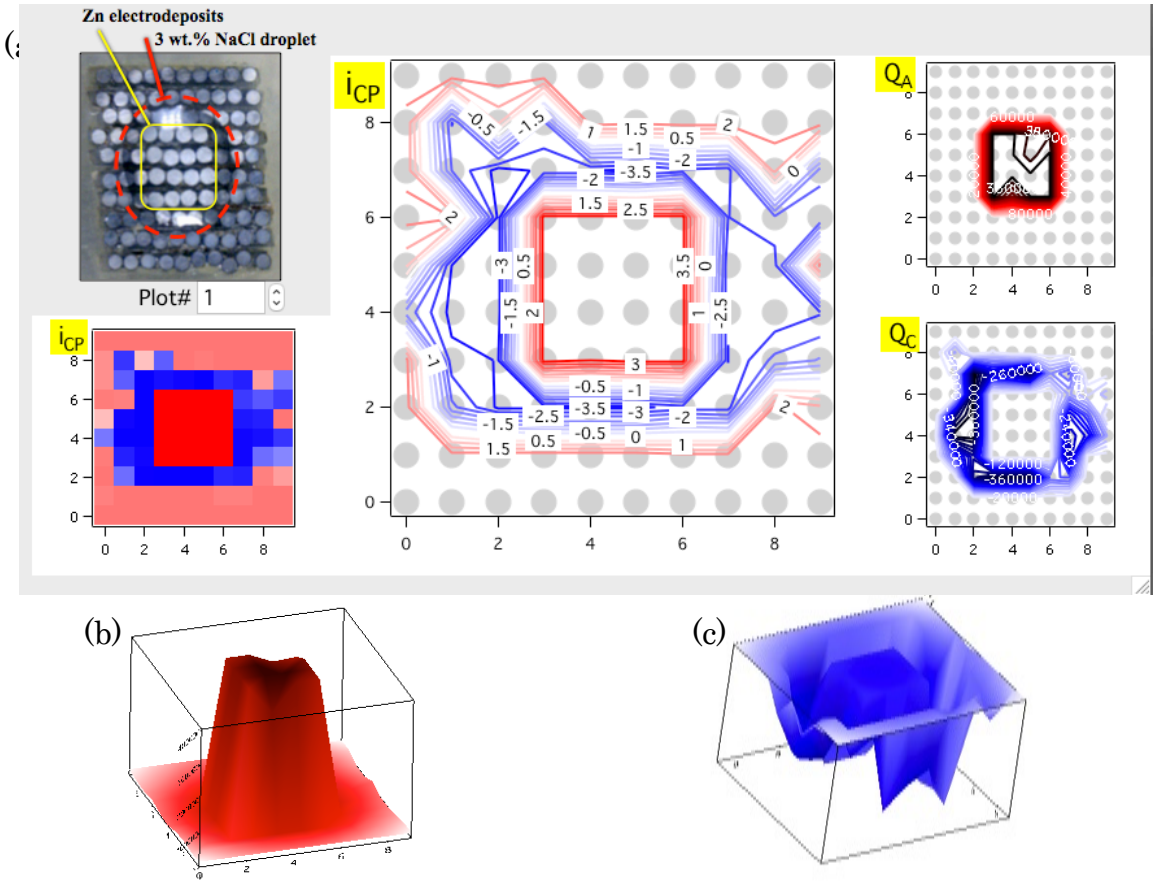


Fig. 2-3-1-1. (a) Example of coupling current map obtained for iron array partially coated with zinc during corrosion test. The images shows surface appearance, image map and contour map of coupling current (i_{CP}) presented with red lines for anodic current and blue lines for cathodic

current, anodic and cathodic electric charge (Q_A, Q_C) maps obtained form integration of anodic and cathodic current, respectively. (b, c) 3D presentation of Q_A, Q_C maps.

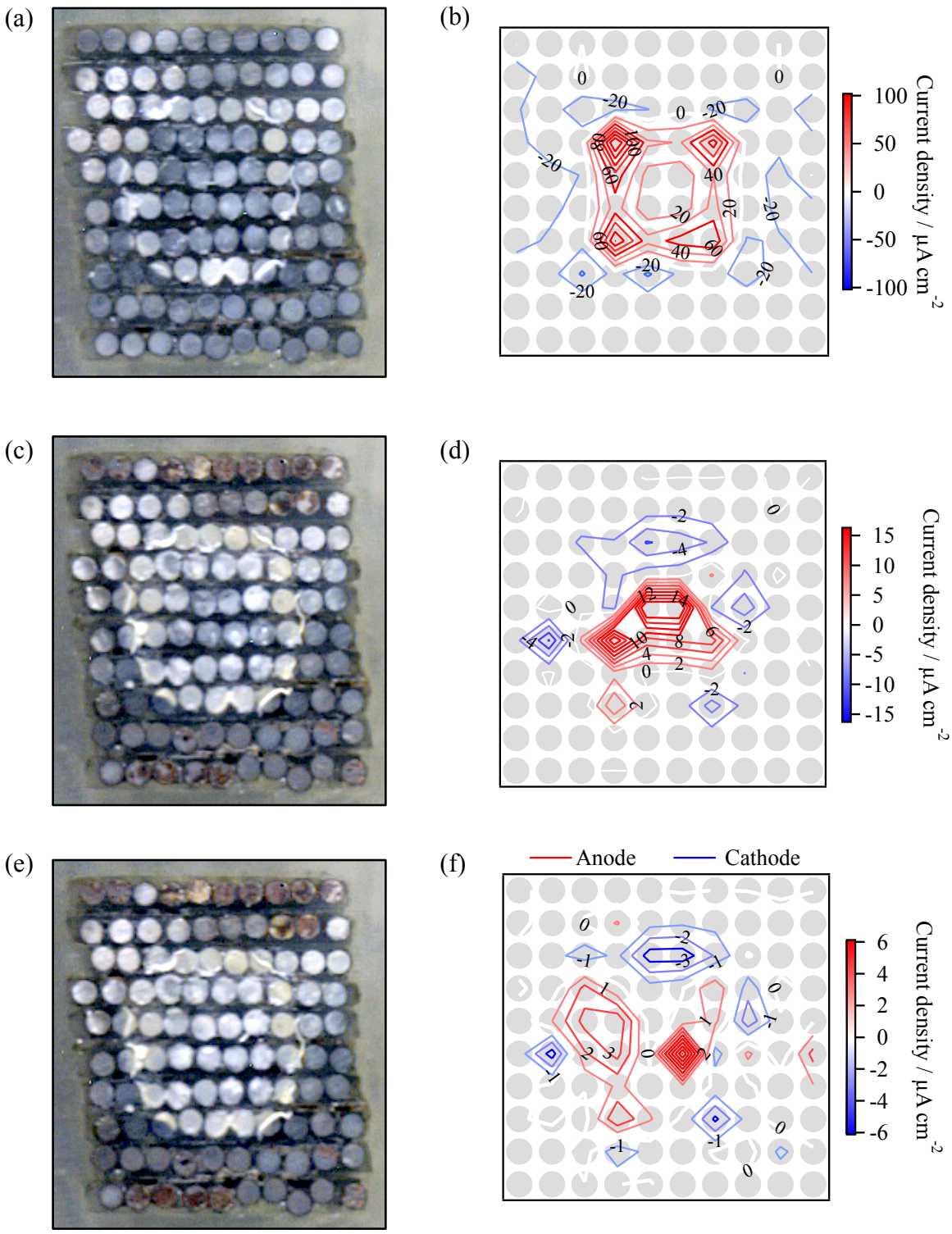


Fig. 2-3-1-2. Appearance of the corroding specimen (*left*) and spatial distribution of coupling current density (*right*) at (a,b) 5 ks, (c,d) 108 ks, and (e,f) 154 ks in the corrosion test.

2.3.2. *Time series transition of coupling current on individual electrodes*

Transitions of the coupling current i^{cp} at four Zn-coated electrodes are shown in **Fig. 2-3-2-1(a)**. Electrode [3, 3] at one of the corners of the Zn-coated area showed initially the largest anodic coupling current i_a^{cp} followed by a drastic decrease of i_a^{cp} at t = 36 ks and then a small cathodic coupling current i_c^{cp} after *ca.* 39 ks. When i_a^{cp} on electrode [3, 3] dropped at t = 36 ks, i_a^{cp} on electrode [3, 4] increased instead. Similar phenomena were observed for the other electrodes at 50 ks and 110 ks. These results indicate that the sacrificial anodic current was shared by these electrodes and that depletion of the Zn coating on some electrodes caused an increase in anodic current on the other anodes. At 143 ks, the Zn coating on these electrodes was depleted. Therefore, the sacrificial corrosion protection stage of Fe due to dissolution of Zn was over at this time.

Time series transition of the anodic coupling charge, Q_a^{cp}, was calculated for the 4 electrodes using Eq.(1) (**Fig. 2-3-2-1(b)**). These four electrodes showed an increase in Q_a^{cp} during sacrificial dissolution, and steady values were reached after depletion of the Zn coating on each electrode. The summation of Q_a^{cp} obtained on the central 4 x 4 electrodes coated with Zn during sacrificial dissolution was calculated to be 37.4 C cm^{-2}, while the electrodeposition charge of Zn was 30 mC cm^{-2}. This indicates the possibility that the anodic coupling current includes not only Zn dissolution but also Fe dissolution (Fe $\rightarrow$ Fe^{2+} + $2e^-$) on Fe electrodes exposed to the environment after depletion of the Zn coating.

Fig. 2-3-2-2 shows another example of the time series transition of two strongly coupled adjacent electrodes, [4, 4] and [5, 4]. Both electrodes acted as anodes until *ca*. 145 ks. Electrode [4, 4] then showed a sudden change from an anode to a cathode due to depletion of the Zn coating, while electrode [5, 4] showed a simultaneous increase in i_a^{cp}, indicating that sacrificial dissolution of the Zn coating on electrode [5,4] increased to compensate for the depletion of neighboring sacrificial electrode [4,4] and also to provide a cathodic current to a new bare Fe electrode at [4,4]. This process accelerated dissolution of the Zn coating and lessened the effective period of galvanic protection on the electrode at [5,4]. At 154 ks, the Zn coating on electrode [5, 4] was depleted and the coupling current on both electrodes decreased gradually to reach a slightly anodic condition.

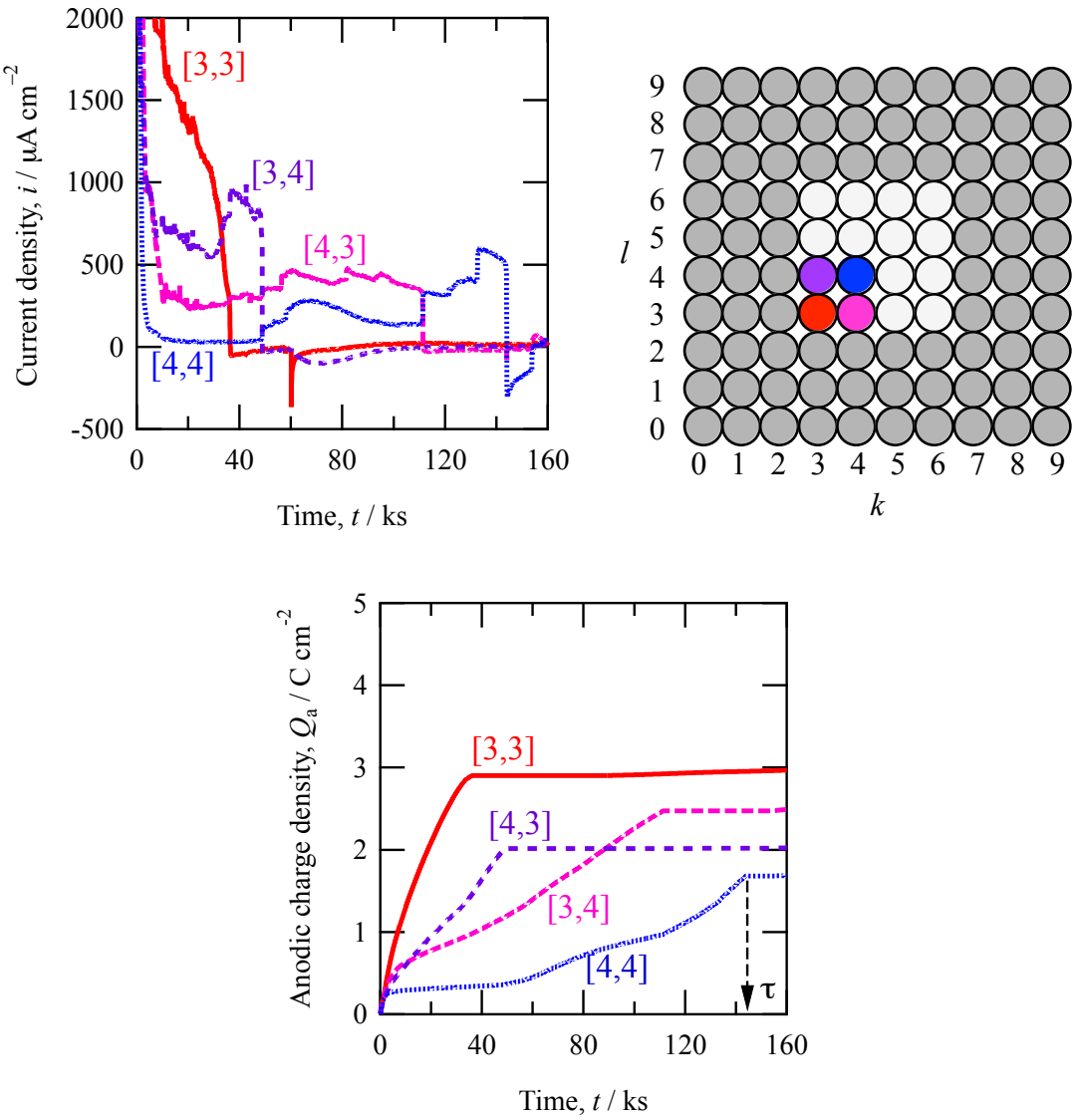


Fig. 2-3-2-1. Time series transition of (a) coupling current density, i^{cp}, and (b) anodic coupling charge, Q_a, on electrodes at [3, 3], [3, 4], [3, 5] and [3, 6].

Table 2-3-2-1. Parameters for obtaining detection ratio of anodic current

Q_t / C cm^{-2}	Q_{dep} / C cm^{-2}	Q_t /Q_{dep}
37.4	30	1.25

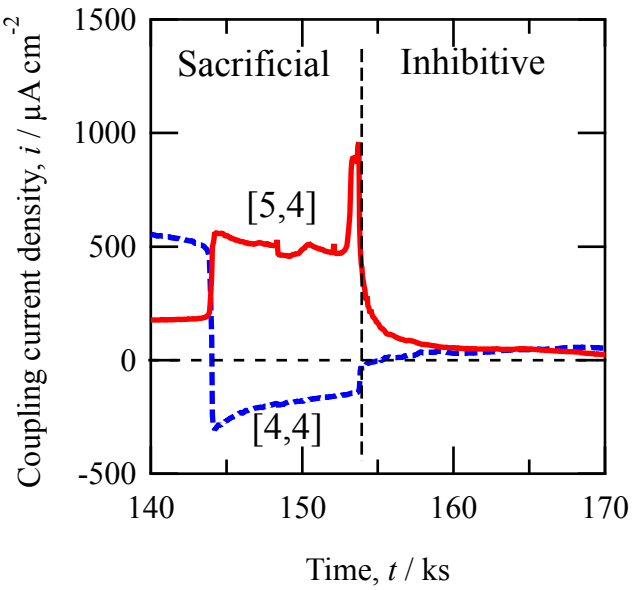


Fig. 2-3-2-2. Coupling current transient of electrodes at [4, 4] and [5, 4].

2.3.3. *Areal categorization of the corroding surface*

After the sacrificial protection stage, corrosion progressed depending on the condition of each Fe electrode surface. The specimen surfaces at a 154 ks and 1000 ks shown in **Fig. 2-3-3-1** (a) and (b), respectively, can be divided into four areas depending on their corrosion states. Area I was initially covered with Zn and began to be covered with Fe rust after the sacrificial dissolution stage. Area III was covered with white Zn corrosion products at the early stage of sacrificial dissolution and was not covered with Fe rust until the end of the corrosion test. The corrosion of Fe in this area therefore appears to be inhibited by Zn corrosion products and/or by local alkalization due to cathodic reaction of oxygen (inhibition stage). Area II was the border between areas I and III. In area II, some electrodes were covered with Fe rust and the others were still covered with white corrosion products. Area IV was the area beyond sacrificial corrosion protection by the Zn coating.

Fig. 2-3-3-1(c) shows a map of the anodic and cathodic coupling charges, Q_a^{cp} and Q_c^{cp}, calculated in the inhibition stage (154 ks – 1000 ks). From a comparison of Fig. 2-3-3-1 with Fig. 2-3-1-2, the corrosion process in the inhibition stage is speculated to be as follows. Area I did not show apparent Q_a^{cp} except for electrode [6,6], although the area was covered with Fe rust. This indicates that the corrosion on these Fe electrodes progressed in the non-coupling condition (micro-cell corrosion on each electrode) after Zn depletion. Area III

tended to show cathodic Q_c^{cp} probably due to the inhibition effects mentioned above. Area II, a border area between areas I and III, showed formation of an anode / cathode pair between the close electrodes. This area seems to be still active for corrosion reaction because the uncovered Fe electrodes with Fe rust or Zn corrosion products could be corroded in the weak coupling condition with the close area.

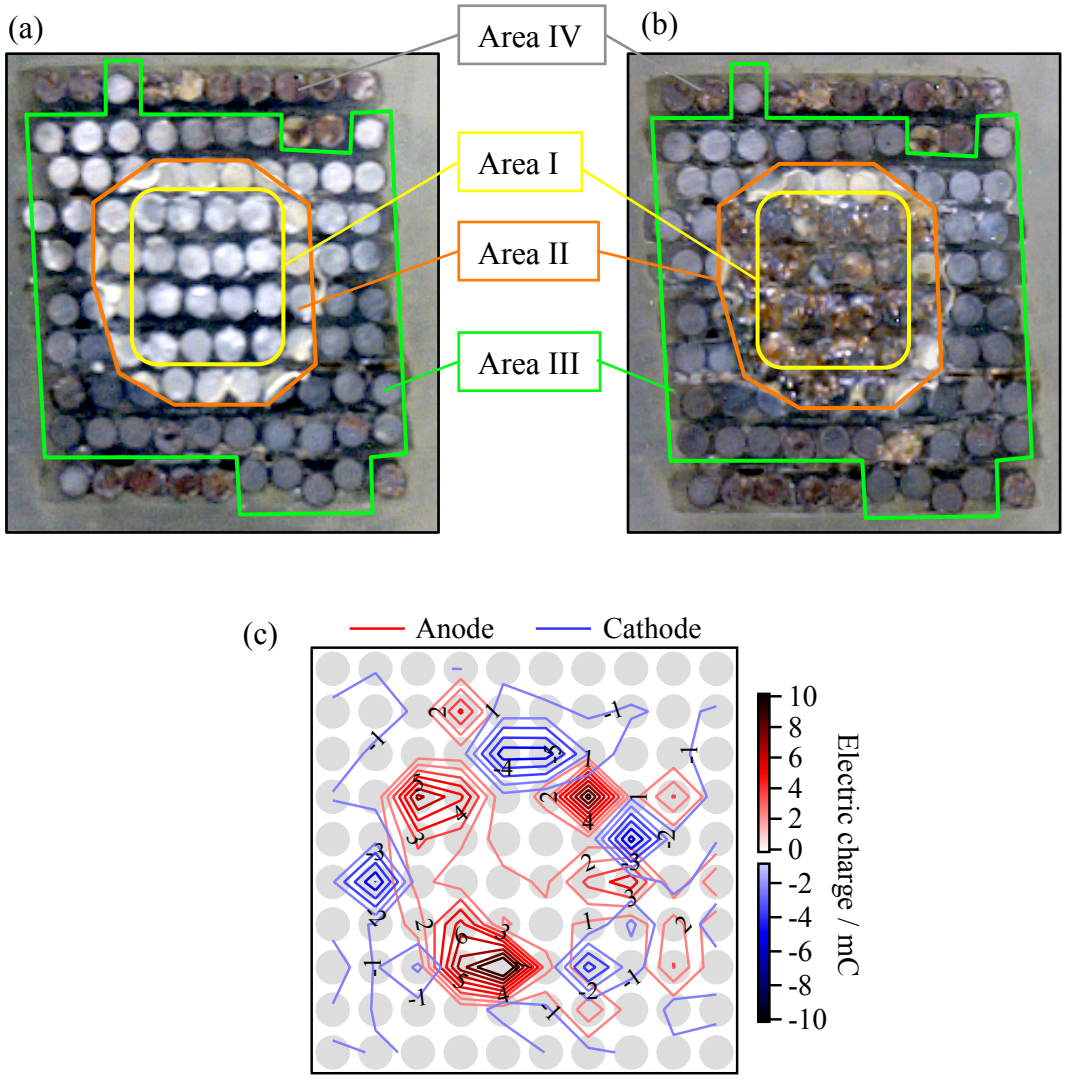


Fig. 2-3-3-1. Photo-images of the corroding specimen at (a) 154 ks and (b) 1000 ks in the corrosion test. (c) A contour map of anodic and cathodic coupling charges, Q_a^{cp} and Q_c^{cp} , of the corroding sample calculated by integration of the anodic and cathodic coupling currents, i_c^{cp} and i_c^{cp}, respectively, in the period between 154 ks and 1000 ks.

To investigate the relationship between the anodic / cathodic contribution and corrosion products of each electrode, microscopic Raman spectroscopy measurement was applied to a selected pair of electrodes at [7,4] and [7,5] as shown in **Fig. 2-3-3-2**. These electrodes belong to area II and were thus not covered previously with a Zn coating. The electrode at [7,4] was covered with Fe rust and the electrode at [7,5] was covered with white Zn corrosion products but not with Fe rust after the corrosion test. The coupling charge on these electrodes in the inhibition stage shown in **Fig. 2-3-3-1(c)** confirmed that electrode [7,4] showed anodic Q_a^{cp} and that electrode [7,5] showed cathodic Q_c^{cp}.

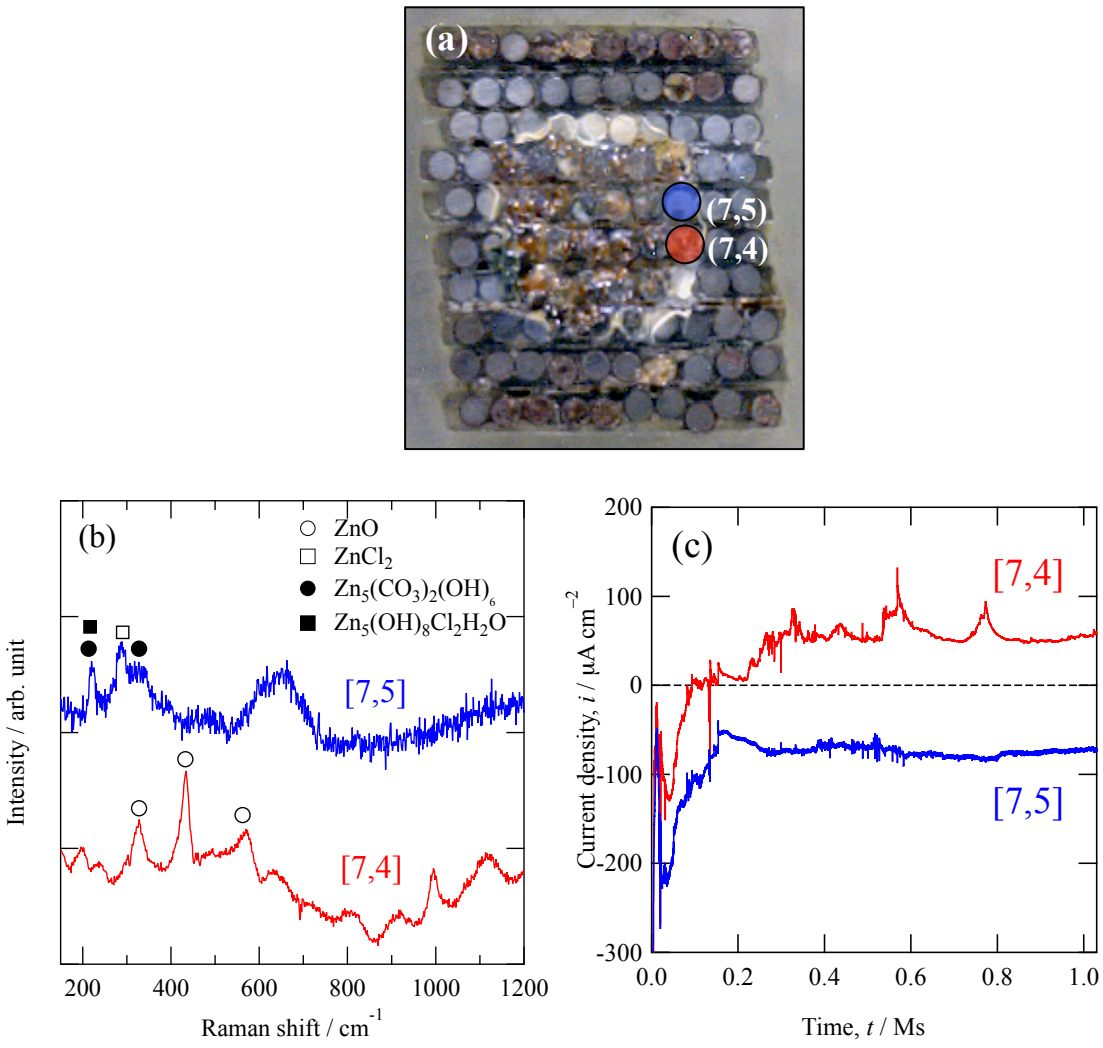


Fig. 2-3-3-2. (a) Surface appearance of the specimen after the corrosion test, (b) Raman spectra and (c) time series transition of the coupling current at electrodes [7, 4] and [7, 5].

Raman spectra of electrode [7,5] showed peaks of hydrozincite ($Zn_5(CO_3)_2(OH)_6$, 225 cm^{-1}), simonkolleite ($4Zn(OH)_2 \cdot ZnCl_2 \cdot H_2O$, 210 cm^{-1}) and zinc chloride (aq. $ZnCl_2$, 290 cm^{-1}) [16,17,18]. This electrode always acted as a cathode, and local pH on this electrode remained alkaline due to continuous oxygen reduction reaction and less amount of water [3,7]. On the other hand, Raman spectra of electrode [7,4] showed peaks mainly assigned to zincite (ZnO, 320, 436 and 550 cm^{-1}) [17]. The electrode [7,4] acted initially as a cathode in the sacrificial stage and then changed to an anode in the inhibition stage. Because both of these electrodes belonged to area II and were located closely, the great difference in their corrosion status at the final stage of the corrosion test may have been caused by the small difference in their initial conditions. For example, accumulation of corrosion products from the dissolving Zn layer on electrode [7,5] was greater than that on electrode [7,4], as can be seen in **Fig. 2-3-1-2(e)**, and this caused a small difference in their roles as slightly anodic for electrode [7,4] and slightly cathodic for electrode [7,5], as can be seen in **Fig. 2-3-1-2(f)**. Once their roles were established, the Fe dissolution caused acidification on the anode by hydration reaction of dissolving Fe ions, which made the precipitation of Zn corrosion products difficult, while progress of alkalization by the oxygen reduction reaction on the cathode promoted corrosion inhibition of Fe and precipitation of Zn corrosion products. Since carbon dioxide gas can be efficiently absorbed in an alkaline solution, formation of hydrozincite might be promoted on the cathode electrodes [1].

2.3.4. *Corrosion process on Zn-coated Fe*

From the results described above, the probable corrosion process at the border between the Zn-coated Fe and the bare Fe is shown in **Fig. 2-3-4-1**. At the initial stage of the corrosion process, the bare Fe surface becomes a cathode and is protected by the sacrificial anodic dissolution of the Zn-coating in a strong coupling condition (**Fig. 2-3-4-1(a)**). The dissolution rate of the Zn-coating surface close to the bare Fe is high because of the short ionic pathway enabling a strong coupling condition. Dissolution of the Zn surface may cause slight acidification of the local solution which enables Zn ions to be dissolved [5,7]. On the bare Fe cathode, oxygen reduction reaction causes alkalization of the local solution and thus promotes the precipitation of Zn ions diffused from the Zn anode to form a white Zn

hydroxide [3,7,19]. As a result, the bare Fe surface close to the Zn anode is covered with $Zn(OH)_2$ and/or zincite layers (Fig. 2-3-4-1(b)). Carbon dioxide can be efficiently absorbed in the alkaline solution on the Fe cathode to form hydrozincite, which is proposed to act as a protective layer against the corrosion reaction due to its lower solubility than that of zincite (**Fig. 2-3-4-1(c)**) [1,20]. **Fig. 2-3-1-2(e)-(f)** shows that the area covered with a protective Zn corrosion product (area III) expanded to a relatively large area around the Zn-coated area (area I) and the amount of $Zn(OH)_2$ (and/or zincite) precipitation was large in area II, where dissolving Zn^{2+} ions from area I and alkaline solution from area III encountered [3,5]. A thick $Zn(OH)_2$ layer covering area II might not be efficiently converted to hydrozincite because of its large thickness and less alkalinity of the local solution [21].

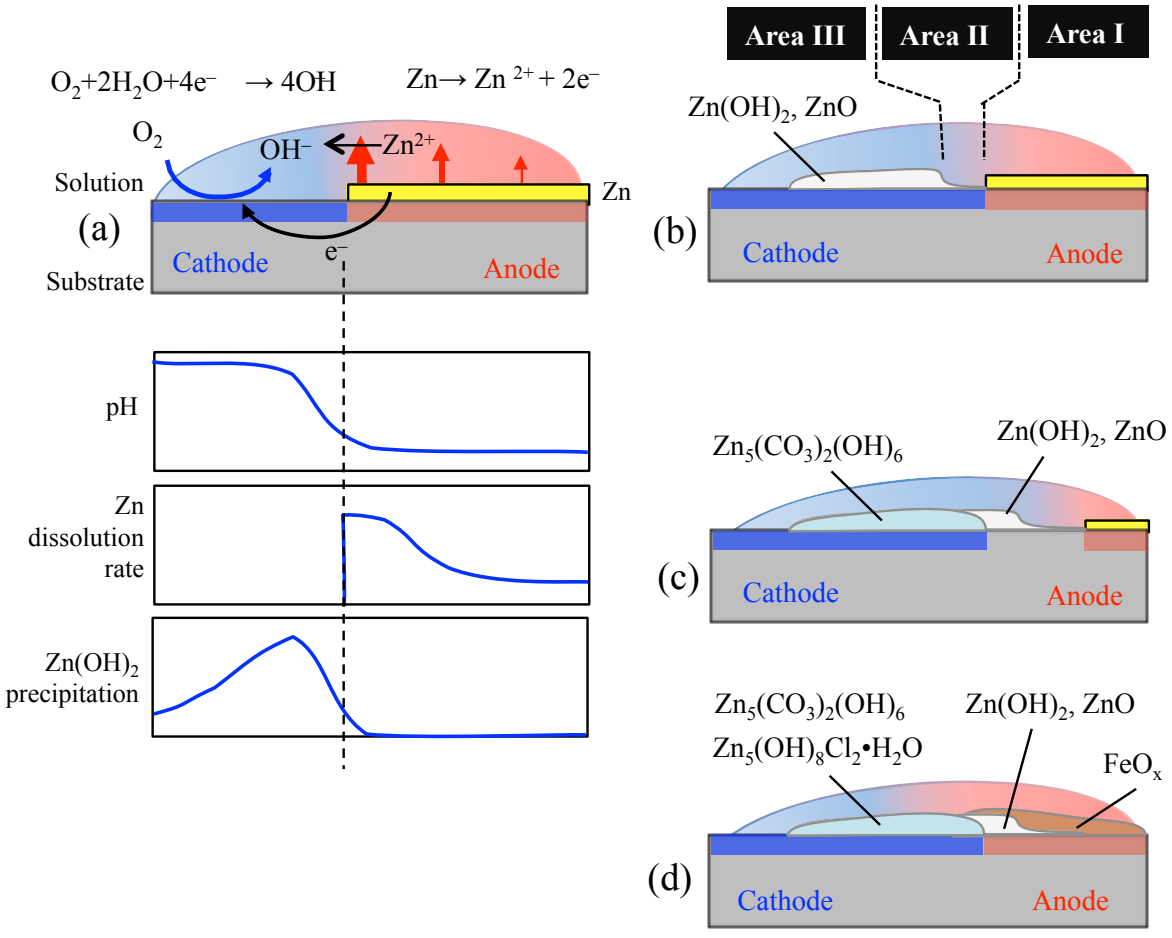


Fig. 2-3-4-1. Schematic diagram of corrosion proceeding on the partially Zn-coated surface; *Left*: initiating sacrificial effect, *Right*: proceeding corrosion and inhibitory effect on corrosion.

When the Zn coating is completely dissolved from area I, *i.e.*, the end of the sacrificial stage, the newly bare Fe surface on area I begins to be easily corroded (**Fig. 2-3-4-1(d)**). The Fe surface covered with a hydrozincite layer acts as a cathode for oxygen reduction reaction coupled with the anodic corrosion reaction of Fe, indicating that the hydrozincite layer might be sufficiently thin to allow electron transfer to the oxygen reduction reaction or that the cathode area is efficiently large to accept cathodic reduction at a low current density. Simonkolleite and zinc chloride are also formed in this area due to presence of Cl^- ions at considerable concentration [1,23], as confirmed in Raman spectra shown in **Fig. 2-3-3-2(b)**. Area II cannot be effectively protected by the $Zn(OH)_2$ (and/or zincite) layer and thus partly accepts the progress of corrosion depending on the condition of the Zn corrosion products covering the surface.

The model proposed above is confirmed by the further analysis of coupling current distribution in the regions 1-4 as shown in **Fig. 2-3-4-2**. In **region 1** where the surface was covered with Zn shows large anodic current due to sacrificial dissolution of Zn until 159 ks (sacrificial period). After 159 ks (after sacrificial period), the anodic coupling current is still dominant because the iron surface was not covered with Zn corrosion film resulting continuous corrosion. Cathodic current contribution is negligible because the anodic reactions on the other regions were already suppressed by Zn corrosion film or iron rust. **Region 3** shows the strongest cathodic protection by the sacrificial Zn dissolution in the sacrificial period and continuous cathodic protection by the anodic reaction in Region 1. **Region 2** shows the intermediate property between the Regions 1 and 3. **Region 4** shows relatively smaller coupling current because the area was far from strong coupling regions 1-3. As a results these regions show different corrosion progress as described in **Fig. 2-3-4-3** in which anodic and cathodic electric charges, Q_A and Q_C, obtained for region 1-4 are plotted. Strong coupling area composed of Regions 1-3 shows distribution of corroding and non-corroding areas around partial Zn coatings. These consideration also proposed that the Zn coated area may be faced to severe corrosion after disappearance of coating more than the other area.

The results describe above confirm that the trace of the coupling current map of the corroding sample in the atmospheric corrosion using 100-channel coupling current

monitoring system can provide useful information to evaluate the corrosion progress and to investigate the corrosion mechanism in the *in-situ* condition.

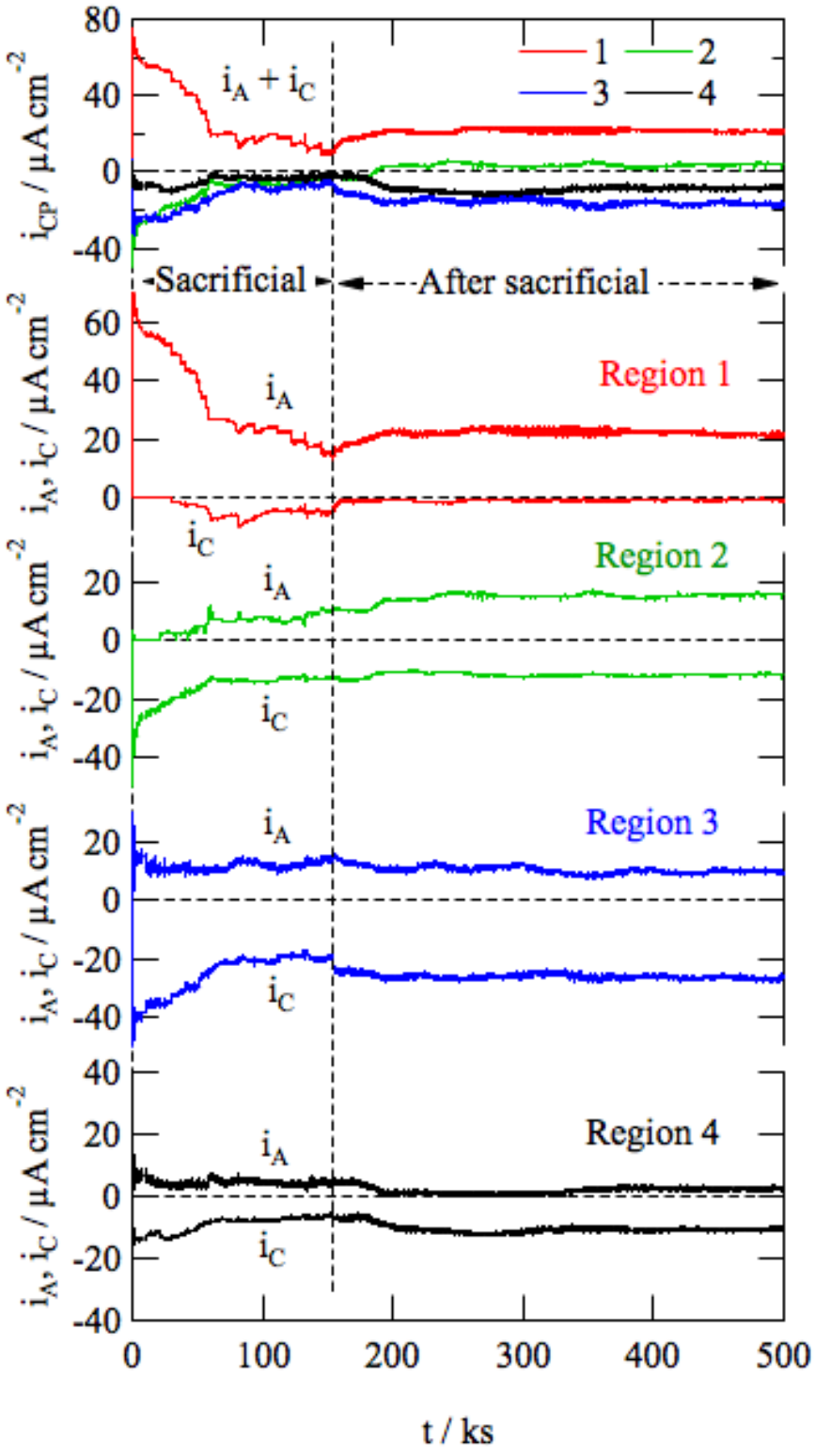


Fig. 2-3-4-2. Time-transition of coupling current ($i_{CP} = i_A + i_B$), anodic and cathodic coupling current (i_A, i_B) obtained for regions 1-4.

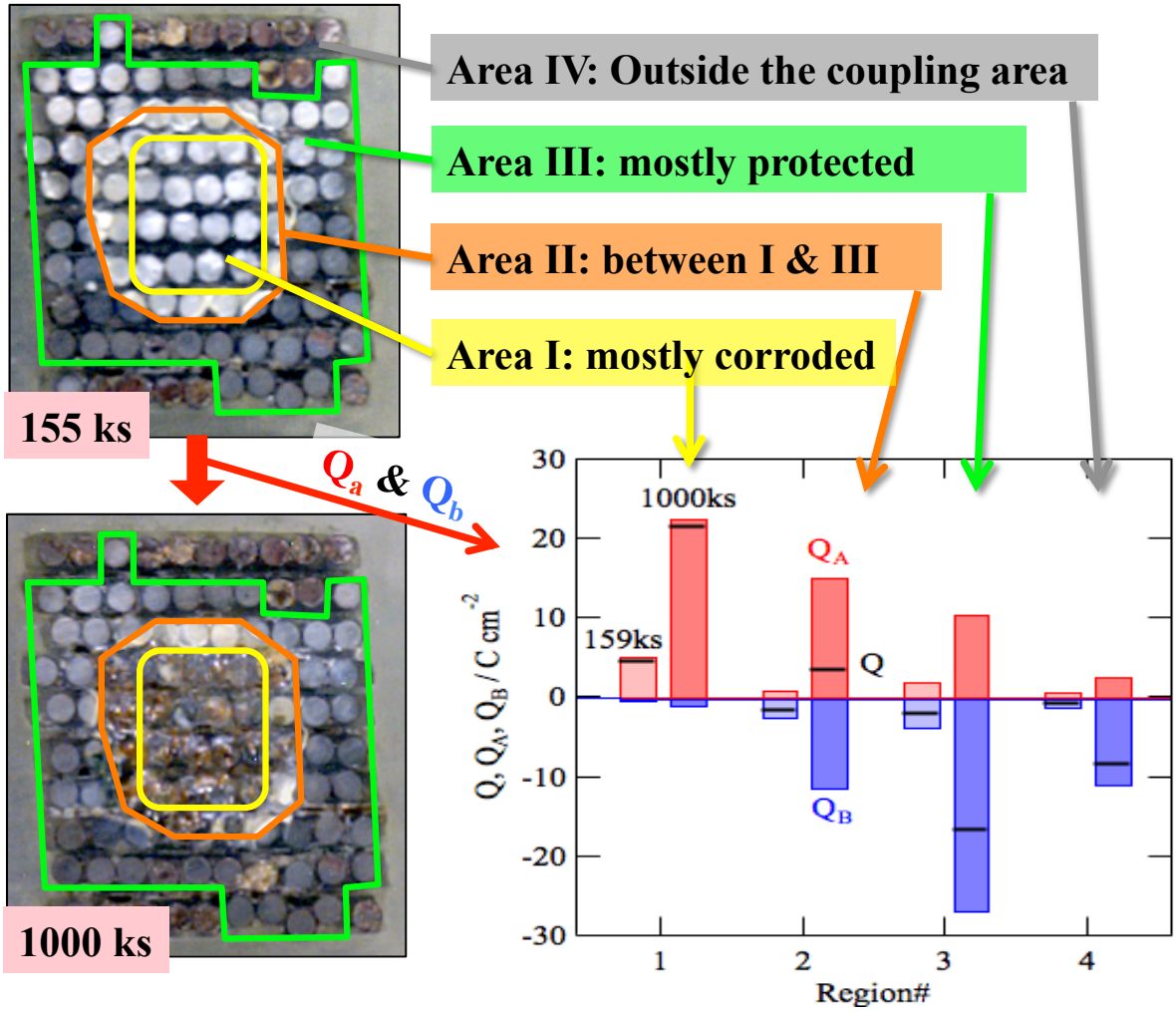


Fig. 2-3-4-3. Total charge (Q, Q_A, Q_B) of obtained for region 1-4 at the test period of 159 ks (sacrificial period) and 1000 ks (after sacrificial period). Q_A and Q_B are anodic and cathodic charge calculated from i_A and i_C, $Q = Q_A + Q_B$

2.4. Conclusion

In this work, corrosion behavior of an Fe specimen partially covered with a Zn coating was investigated by using a 100-channel electrodes coupling current measurement system, and a coupling current map on the specimen was traced during a corrosion test simulating atmospheric corrosion. The time series of the coupling current map clearly revealed transition of the corrosion protection mechanism of Fe from sacrificial protection by

the anodic dissolution of Zn to inhibition by covering with the Zn corrosion product. During the sacrificial protection period, Zn ions extend to the area around the Zn-coating and form a hydrozincite layer with absorbed CO_2 in the local solution alkalized by the cathodic oxygen reduction reaction. After depletion of the Zn coating, corrosion of Fe could be inhibited by the hydrozincite and simonkolleite layer covering the Fe surface but not by the zincite layer, as confirmed by the relationship between the coupling current and Raman spectra on individual electrodes.

References

[1] C. Leygraf and T. E. Graedel, Atmospheric Corrosion, Electrochemical Society Series, Wiley-Interscience, John Wiley & Sons, Inc., N.Y. (2000).

[2] K. Ogle, S. Morel and D. Jacquet, *J. Electrochem. Soc.*, **153**, B1 (2006).

[3] F. Thébault, B. Vuillemin, R. Oltra, C. Allely and K. Ogle, *Electrochim. Acta*, **56**, 8347 (2011).

[4] K. Ogle, V. Baudu, L. Garrigues and X. Philippe, *J. Electrochem. Soc.*, **147**, 3654 (2000).

[5] A.P. Yadav, H. Katayama, K. Noda, H. Masuda, A. Nishikata and T. Tsuru, *Electrochim. Acta*, **52**, 3121 (2007).

[6] J.Izquierdo, L. Nagy, Á. Varga, J.J. Santana, G. Nagy, R.M. Souto, *Electrochim. Acta,* **56**, 8846 (2011).

[7] E. Tada, S. Satoh, H. Kaneko, *Electrochim. Acta,* **49**, 2279 (2004).

[8] Y.-J. Tan, *Corros. Sci.*, **41**, 229 (1999).

[9] Y. Tan, N.N. Aung, T. Liu, *Corros. Sci*., **63**, 379 (2012).

[10] T.H. Muster, A. Bradbury, A. Trinchi, I.S. Cole, T. Markley, D. Lau, S. Dligatch, A. Bendavid, P. Martin, *Electrochim. Acta,* **56**, 1866 (2011).

[11] N. D. Budiansky, J. L. Hudson, and J. R. Scully, *J. Electrochem. Soc.*, **151**, B233 (2004).

[12] F. Bocher, F. P.-Moreno, N. D. Budiansky, and J. R. Scully. *Electrochemical and Solid-State Letters*, **10**, C16 (2007).

[13] K. Fushimi, A. Naganuma, K. Azumi and Y. Kawahara, *Corros. Sci.*, **50**, 903 (2008).

[14] A. Naganuma, K. Azumi, *Corros. Sci.,* **52**, 1179 (2010).

[15] A. Naganuma, K. Azumi, *Corros. Sci.,* **53**, 1165 (2011).

[16] M. Bouchard and D.C. Smith, *Spectrochim. Acta A*, **59**, 2247 (2003).

[17] M.C. Bernard, A. Hugot-Le Goff, D. Massinon and N. Phillips, *Corros. Sci.*, **35**, 1339 (1993).

[18] M. Ueda, M. Matsuda, and T. Ohtsuka, *Proc. Electrochemical Soc*. PV, **14**, 166 (2004).

[19] F. Thébault, B. Vuillemin, R. Oltra, K. Ogle, C. Allely, *Electrochim. Acta,* **53**, 5226 (2007).

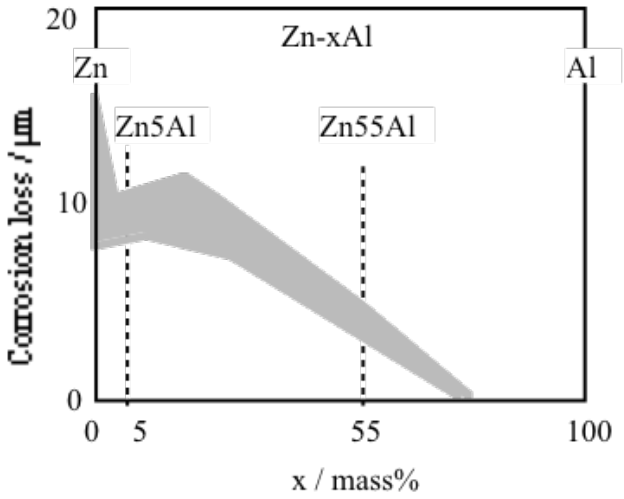
[20] J.M. Zachara, J.A. Kittrick, L.S. Dake and J.B. Harsh, *Geochim. Cosmochim. Acta*, **53**, 9 (1989).

[21] J.D. Yoo, K. Ogle, P. Volovitch, *Corros. Sci.,* **81**, 11 (2014).

Chapter 3. Co-electrodeposition of Al-Zn coatings from an $AlCl_3$–$ZnCl_2$–EMIC bath

3.1. Introduction

In chapter 1 the corrosion behavior of Zn coated steel was investigated using the 100 channel multi-electrodes system to visualize the corrosion progress and corrosion-protection function of Zn in the atmospheric corrosion. In the practical structural materials, however, Zn-based alloy coatings has been used. Among various alloy coatings, Zn-Al coatings have been provided excellent anticorrosion performance in practical use [1-4].

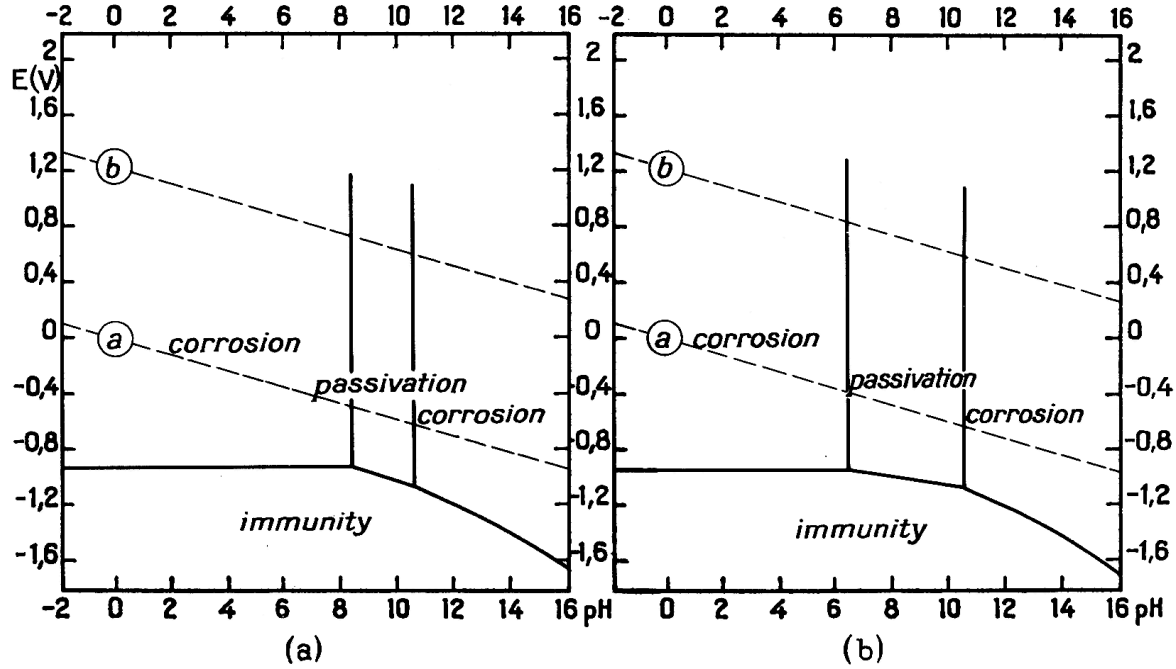


Corrosion loss of Zn-Al alloy coatings, J.B.Horton, Corrosion Control by Coatings, Science Press, Princeton (1979); D.J.Blickwede, 鉄と鋼, 66[7] (1980) 821-834

A hot-dip galvanization method has been used to form the Al-Zn alloy galvanized coatings on steels in which steel substrate is dipped in a molten Al-Zn bath at a temperature around 450 °C. In this process, however, intermetallic compounds are formed at the interface between the coating and the substrate and also oxides may be formed on the substrate steel due to the high temperature operation and lessens sometimes the adhesion of coatings [5-7]. In compensation for the simple and fast dipping process, hot-dip method has a difficulty in precise control of the thickness and uniformity of coatings. These parameters can contribute to improvement of the performance of the coatings and reduction of use of Zn resources. Alternatives of the Al-Zn coating methods have therefore been investigated such as electrodeposition methods that can be operated at a lower temperature. In this

electrochemical process, steel substrate is immersed in plating bath of aqueous, non-aqueous or molten salts and cathodically polarized to enable electrodeposition of metal coating from the bath containing metal ions. In case of alloy coating, electrodeposition is conducted in the bath containing different kinds of metal ions and the composition of the coatings can be controlled by changing the bath composition and electrodeposition condition such as static polarization potential and pulse timing in the pulse polarization method. Not only the coating composition but also macro- and micro-structure of the alloy or co-deposit coatings are also affected by the electrodeposition parameters such as polarization current density that directly connected to the deposition rate. For example, large current density of electrodeposition enable the rapid nucleation of deposits with a high density on the substrate at the initial stage of electrodeposition and may contribute to the uniform deposition of coating. On the other hand, rapid growth of nuclei may also result in a less dense deposit composed of dendritic crystal with considerable voids or defects. In case of limited bath volume relative to the substrate area in the electrodeposition process, compositional change of coatings in the depth direction caused by change in bath composition during the plating process may also be considered.

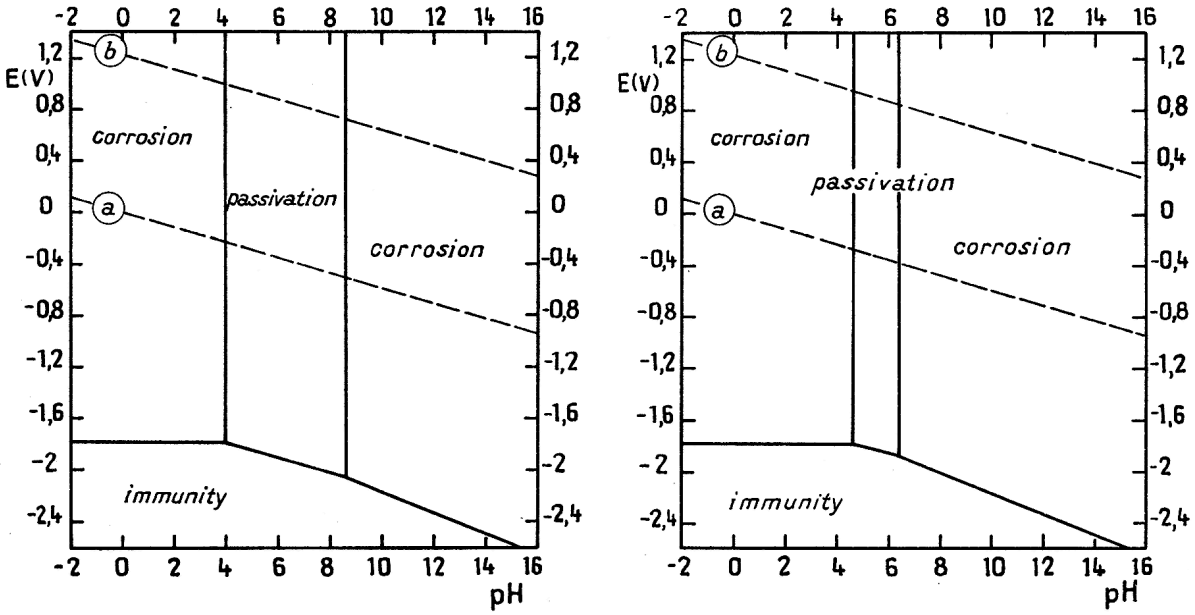
In the Paouraix diagrams of Zn and Al shown below, the redox potential of Al (Al^0 / Al^{3+}) and Zn (Zn^0 / Zn^{2+}), *i.e.*, the border line between immunity/passivation and corrosion, is less-noble than the hydrogen evolution (water decomposition) potential (line (a)). This indicates the water decomposition proceeds if the electrode potential is lowered to the electrodeposition potentials. Fortunately, in case of Zn, large overpotential for hydrogen evolution reaction as 0.7V enables electrodeposition of Zn even in aqueous solution. However it is not the case of Al. For electrodeposition of Al or Al-Zn alloy, therefore, non-aqueous bath should be used. Generally molten salt bathes at high (inorganic salt) or room (ionic liquid) temperature bathes has been therefore used.



(*a*) Deduced from Fig. 1, for solutions free from CO_2.

(*b*) For solutions containing CO_2 (1 g-mol/l).

Pourbaix diagram of zinc in aqueous solution with or without CO_2. The broken lines (a) and (b) represent oxygen evolution reaction and hydrogen evolution reaction, respectively, in a aqueous solution. Reprint from "M. Pourbaix, *Atlas of Electrochemical Equilibria in. Aqueous Solutions*, NACE, Houston, TX. (1974)."

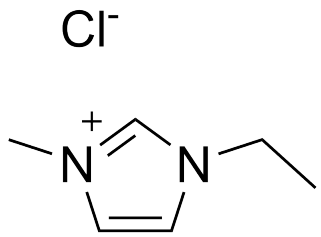


(*a*) Passivation by a film of hydrargillite $Al_2O_3.3H_2O$.

(*b*) Passivation by a film of böhmite $Al_2O_3.H_2O$.

Example of a Pourbaix diagram of aluminum in aqueous solution covered with hydrargillte and bohmite.

An ionic liquid bath such as a mixture of 1-ethyl-3-methylimidazolium chloride (EMIC) and metal chloride salts has been used to investigate Al electrodeposition [8-13]. Generally ionic the liquid bath has many advantages against to the water-based bath such as wide potential window enabling electrodeposition of less-noble metals, high electric and ionic conductivity because the whole bath is composed with ionic species, high solubility of metal ions due to formation of metal-ion complex at very high concentration, superior stability at high temperature widening the suitable condition for electrodeposition even at temperature higher than 100 °C.



1-ethyl-3-methylimidazolium chloride (EMIC)

In an acidic EMIC-$AlCl_3$ ionic liquid bath, it has been suggested that the dominant complex ions of $Al_2Cl_7^-$ can be electrochemically reduced to form Al deposits as presented in the next reaction [11];

$$4Al_2Cl_7^- + 3e^- \rightarrow 7AlCl_4^- + Al.$$

For the electrodeposition of Zn in the acidic EMIC-$ZnCl_2$ bath, it has been proposed that Zn can be electrodeposited from a $ZnCl_3^-$, $Zn_2Cl_5^-$ or $Zn_3Cl_7^-$ complex depending on the bath acidity [12]. In a neutral bath, however, predominant $ZnCl_4^{2-}$ ions are less reactive to the electrodeposition reaction [12].

In this chapter, the results of co-electrodeposition of Al-Zn from an EMIC base ionic liquid bath containing Al and Zn complexes are presented. The potentiostatic polarization was conducted to investigate the effect of deposition potential on surface morphology and composition of coatings. Furthermore, effect of heat treatment on the micro-structure of the coatings was also examined in which the transformation of the Al-Zn codeposits to alloy structure was intended.

3.2. Experimental

3.2.1. Preparation and characterization of an $AlCl_3$–$ZnCl_2$–EMIC ionic liquid bath

An ionic liquid (IL) bath composed of $AlCl_3$: $ZnCl_2$: EMIC = 1.8 : 0.01 : 1 in molar ratio was prepared as following in a glove box filled with dried N_2 gas. Anhydrous $AlCl_3$ powder (Junsei Chemical Co., 98% in purity) was added slowly to EMIC (Merck Co.) of 20 cm^3 in volume to reach a molar ratio of $AlCl_3$: EMIC = 1.8 : 1. An Al wire (Nilaco Co., 99.999% in purity) was then immersed in the bath at 80 ºC for 2 days to remove residual water. After this pretreatment, $ZnCl_2$ (Junsei Chemical Co., 98.0% in purity) was added to reach a molar ratio of $ZnCl_2$: EMIC = 0.01 : 1. This solution was then stirred at 80 ºC for 1 h to dissolve $ZnCl_2$ entirely. Finally a transparent solution with slightly brown color was obtained suitable for electrodeposition experiments.

3.2.2. Electrochemical experiments

For electrochemical experiments, a conventional three electrodes system composed of a working electrode (WE) of Pt plate (5x5 mm, Nilaco Co., 99.8% in purity) or Cu plate (Nilaco Co., 99.96% in purity), a counter electrode (CE) of Pt or a Zn (Nilaco Co., 99.99% in purity) plate, and a quasi-reference electrode (RE) of Al wire (Nilaco Co., 99.999% in purity) was used. The Al-RE was put in a glass tube filled with $AlCl_3$–EMIC ($AlCl_3$:EMIC = 1.8 : 1) and the tip of the glass tube was sealed with a porous ceramics. Cyclic voltammogram of Pt-WE in a plating bath was measured in a potential range from 2.0 V to –0.5 V (vs. Al-RE) with a scan rate of 30, 50, 100, 150, and 200 mV s^{-1}. Potentiostatic polarization was conducted for co-electrodeposition of Al-Zn on a Cu-WE plate using Zn-CE. Prior to polarization, a Cu-WE plate was ground with diamond abrasive of 1 μm in average particle size. A Cu-WE was then potentiostatically polarized in a potential range within a range of –0.2 and –0.7 V (vs. Al-RE). An electric charge of cathodic polarization was fixed to be 15 C cm^{-2} using a computer controlled potentiostat (Ivium technologies Co., Iviumstat). After electrodeposition, the Cu-WE was rinsed with ethanol and acetone and then dried in an air stream. A coulombic efficiency (η), of electrodeposition was calculated from the following equation;

$$\eta = \frac{F}{q}\sum\frac{n_i \Delta w_i}{M_i},$$

where n_i is a number of electrons for electrodeposition reaction of each element i (Al or Zn), Dw_i is the weight gain of element i due to electrodeposition, M_i is atomic weight, q is the cathodic polarization charge (15 C cm^{-2}), and F is the Faraday constant.

3.2.3. Heat treatment

The samples with Al-Zn co-electrodeposited were put in a glass tube with N_2 gas flow to be subjected to the heat treatment using a electric furnace. Temperature was elevated from room temperature to 350 ºC with a rate of 10 ºC min^{-1}, kept for 10 min or 1 h at 350 ºC, and then cooled naturally to room temperature.

3.2.4. Characterization of coatings

The surface morphology and the elemental composition of coatings were investigated by using SEM and EDX (JEOL Ltd., model JSM-6500F). Microstructure of the coatings was analyzed using XRD analyzer (Rigaku Co., RINT-2000 X-ray diffractometer using Cu Ka radiation under a q-2q mode).

3.3. Results and discussion

3.3.1. Analysis of ionic liquid

Typical cyclic voltammogram of Pt-WE immersed in $AlCl_3$-$ZnCl_2$-EMIC bath is shown in **Fig. 3-3-1-1**. Two peaks can be observed respectively in both potential scan in a anodic and cathodic directions, indicating that two redox reactions of Al and Zn occurred. In a potential scan in a cathodic direction, cathodic reaction occurred at 0.3 V and –0.2 V. Considering the redox potential of metals, it is suggested that the cathodic peak at 0.3 V corresponds to reduction of Zn complex ions and that at –0.2 V

Fig. 3-3-1-2 shows dependence of cathodic current peak of Zn reduction at 0.3 V on square root of scan rate. The linear relationship in the plot indicates that the electrodeposition of Zn was diffusion control.

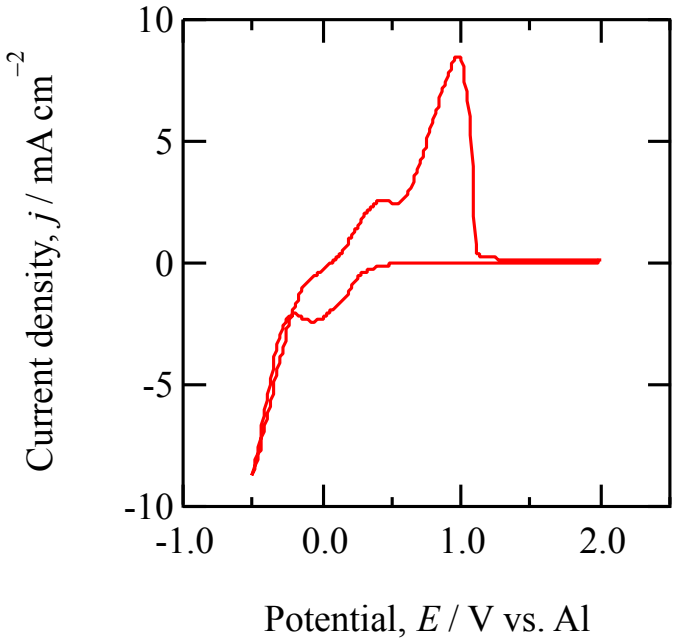


Fig. 3-3-1-1. Cyclic voltammogram of Pt-WE in an ionic liquid bath of $AlCl_3$–$ZnCl_2$–EMIC (1.8 : 0.01 : 1 in molar ratio) with scan rate of 100 mV s^{-1}.

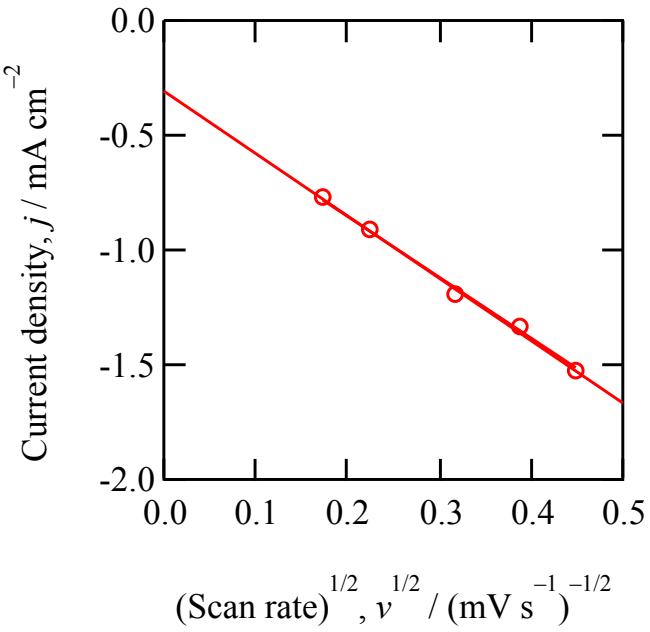


Fig. 3-3-1-2. Relationship between the cathodic current peak and the square root of scan rate measured for Pt-WE.

3.3.2. Co-electrodeposition of Al and Zn by potentiostatic polarization

Property of electrodeposition

Surface appearance of the specimen at various deposition potential is shown in **Fig.**

3-3-2-1. The coatings were uniform at every deposition potential. The color of coatings change to be whitish as the deposition potential becomes less noble.

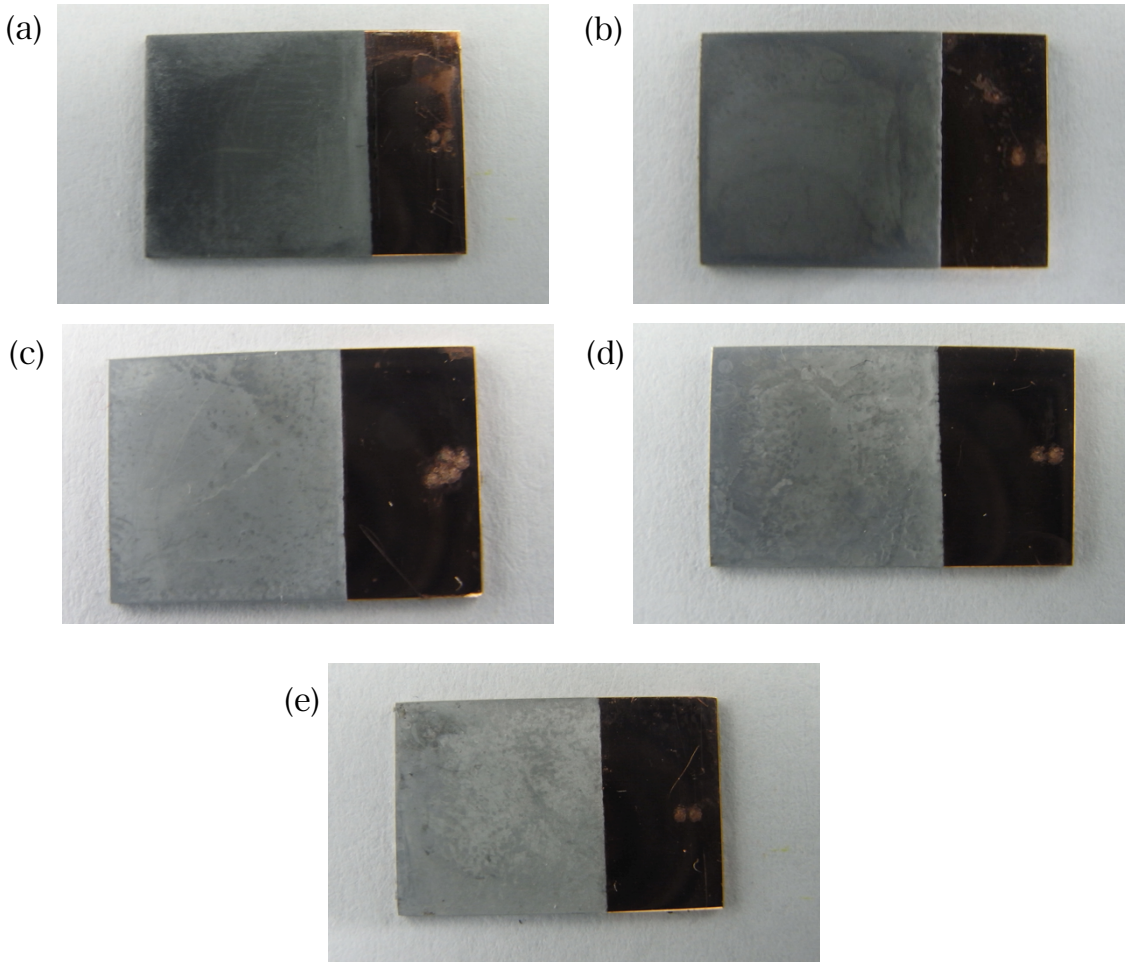


Fig. 3-3-2-1. Surface appearance of the Cu-WE after potentiostatic polarization at (a) –0.1, (b) –0.2, (c) –0.3, (d) –0.4, and (e) –0.5 V vs. Al-RE.

The current density during electrodeposition correlates with deposition potential. Time transients of current density during electrodeposition at each deposition potential are shown in **Fig. 3-3-2-2**. Cathodic current density increased as the deposition potential is less noble, indicating more Al was contained in the coatings because of the limitation of Zn reduction reaction caused by diffusion limitation. In electrodeposition at –0.1 and –0.2 V, current density slightly increased as the proceeding of electrodeposition, indicating that the roughness of surface increased because of preferential nuclei growth. Hence current density increased as the surface area increased.

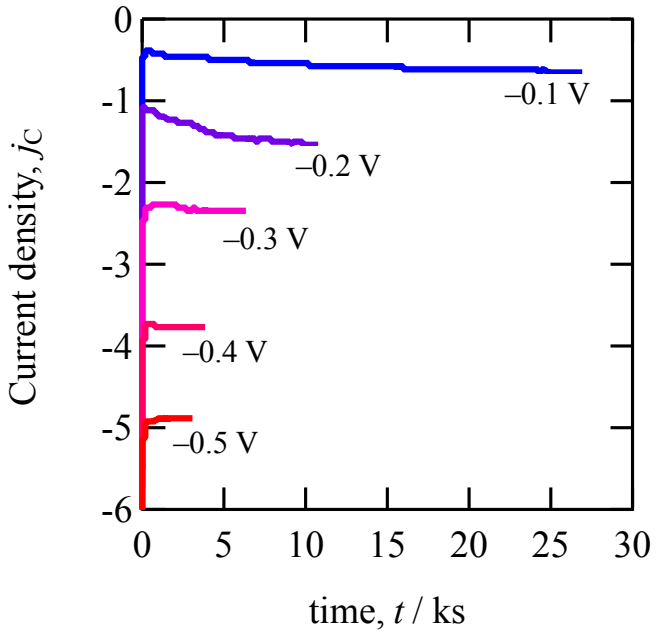


Fig. 3-3-2-2. Transition of polarization current (j_C) of Cu-WE during potentiostatic polarization in $AlCl_3$–$ZnCl_2$–EMIC bath.

The composition of Zn in the coatings gradually decreased as the deposition potential become less noble. The dependence of Zn composition on deposition potential is shown in **Fig. 3-3-2-3**. As shown in **Fig. 3-3-1-1**, less noble deposition potential leads large amount of Al deposition because of limitation of Zn deposition rate.

The electrodeposition from the IL bath leads high charge efficiency (η). **Fig. 3-3-2-4** shows the charge efficiency at each deposition potential. As shown in **Fig. 3-3-2-4**, η is higher than 0.8 at every deposition potential, indicating that the side reaction such as decomposition of water residuals and/or oxygen reduction derived from atmosphere in the grove box.

Microstructure of coatings

The surface structure of Zn coatings depended on the deposition potential. **Fig. 3-3-2-5** shows the surface morphology of the coatings obtained by electrodeposition at each deposition potential. In **Figs. 3-3-2-5 (a)** and **(b)**, the shape of particles is similar the hexagonal crystal, derived from *hcp* crystal structure of Zn. The smallest particle was obtained in the electrodeposition at –0.3 V. In electrodeposition at less nobler potential than –

0.3 V, relatively larger sizes of particles were obtained. The shape of particle obtained at less noble than –0.3 V was derived from the crystal structure of Al. These results indicate that both Zn and Al deposits hinder nuclei growth each other.

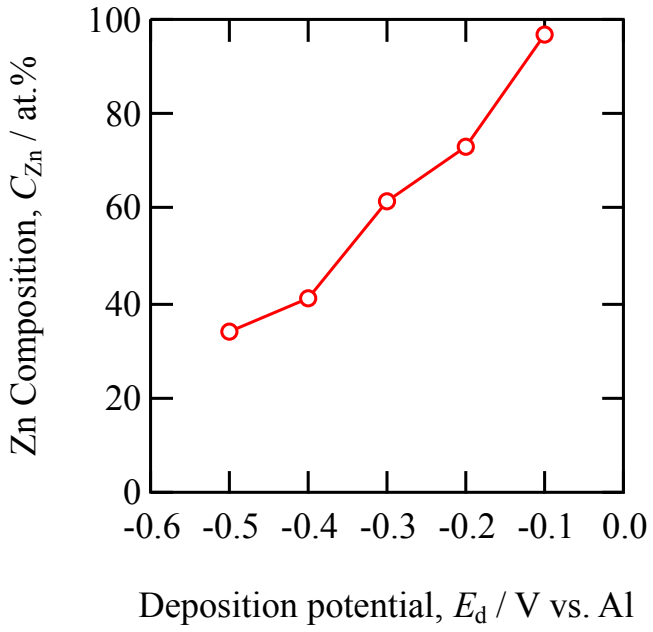


Fig. 3-3-2-3. Relationship between the Zn composition of the coatings and deposition potential.

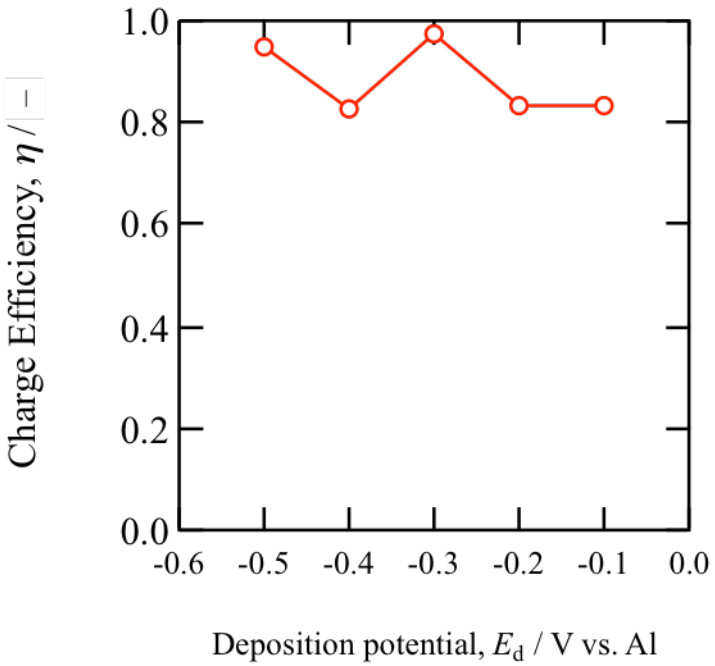


Fig. 3-3-2-4. Coulombic efficiency of Al-Zn co-electrodeposition as a function of potentiostatic polarization potential.

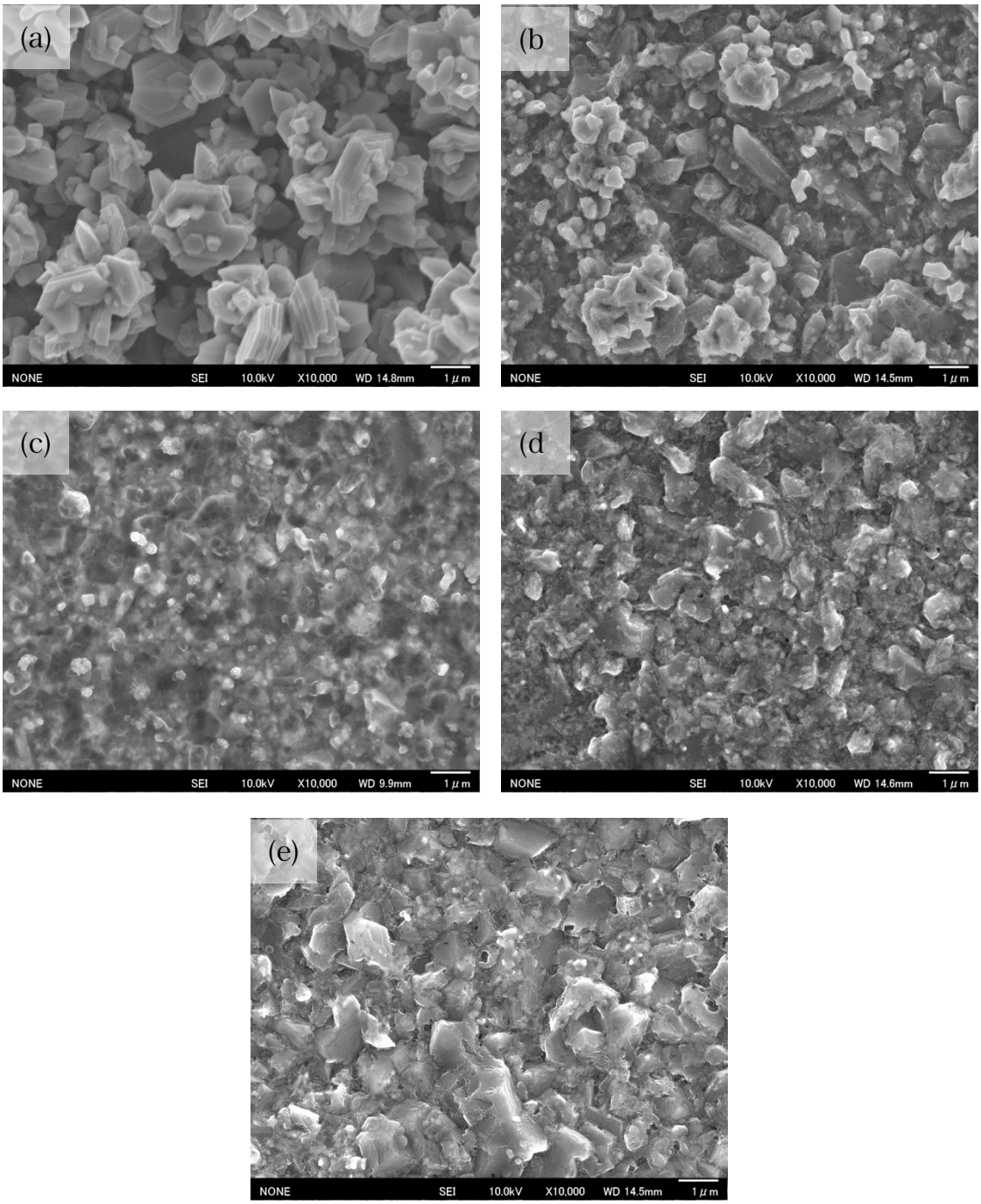


Fig. 3-3-2-5. Surface SEM images of Al-Zn co-electrodeposits obtained with potentiostatic polarization at (a) –0.1, (b) –0.2, (c) –0.3, (d) –0.4, and (e) –0.5 V vs. Al-RE.

Fig. 3-3-2-6 shows X-ray diffraction pattern of specimen. Peaks of metallic Al and Zn exist at all electrodeposits in addition to peaks originating from Cu substrate. Compared with **Fig. 3-3-2-3**, intensity of both Al and Zn peaks has relationship with the composition of coatings. On the other hand, the peaks originating from Al-Zn alloy did not exist at all pattern,

indicating that most of Al and Zn individually deposited as metallic Zn and Al.

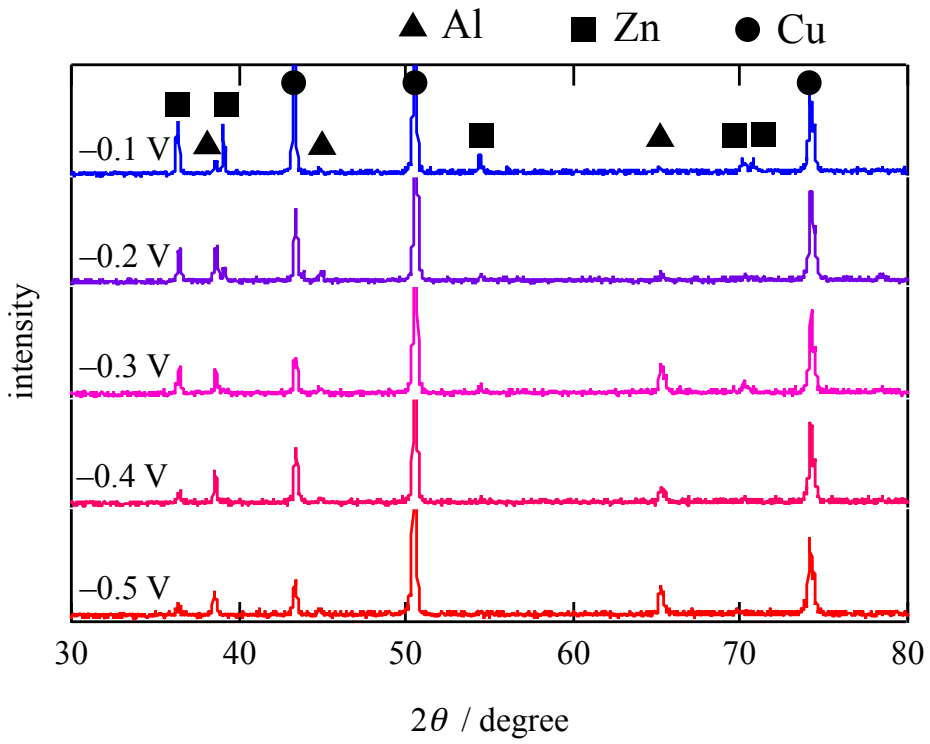


Fig. 3-3-2-6. XRD pattern measured for Al-Zn co-electrodeposits obtained with potentiostatic polarization at –0.1, –0.2, –0.3, –0.4, and –0.5 V vs. Al-RE.

3.3.3. Effect of heat treatment

The surface morphology was changed by heat treatment in moderate temperature compared with hot-dip treatment. The surface morphology after 1 h heat treatment is shown in **Fig. 3-3-3-1**. From the comparison of **Fig. 3-3-2-5**, the morphology changed in every coating, implying that heat treatment can affect the structure of coatings.

To investigate the changes of structure by heat treatment, X-ray diffraction pattern was obtained. **Fig. 3-3-3-2** shows the XRD pattern of coatings after 10 min. and 1 h of heat treatment. Compared with **Fig. 3-3-3-3**, the peaks originated from metallic Al and Zn was disappeared, and a few peaks generated. The peaks on diffraction angle around 44º and 75º derived from the structure changes of substrate Cu. On the other hand, the peak exists at 2q = 44.38º appeared at less noble deposition potential than –0.2 V. Additionally, the intensity of this peak increased with longer heat treatment. Furthermore, the highest intensity was obtained from the deposits at –0.2 V, and gradually decreased as less noble deposition

potential. These results indicate that this peak originate from $Al_{0.403}Zn_{0.597}$ alloy and thus heat treatment leads alloying of Al and Zn even lower temperature than appearing liquid phase of both Al and Zn.

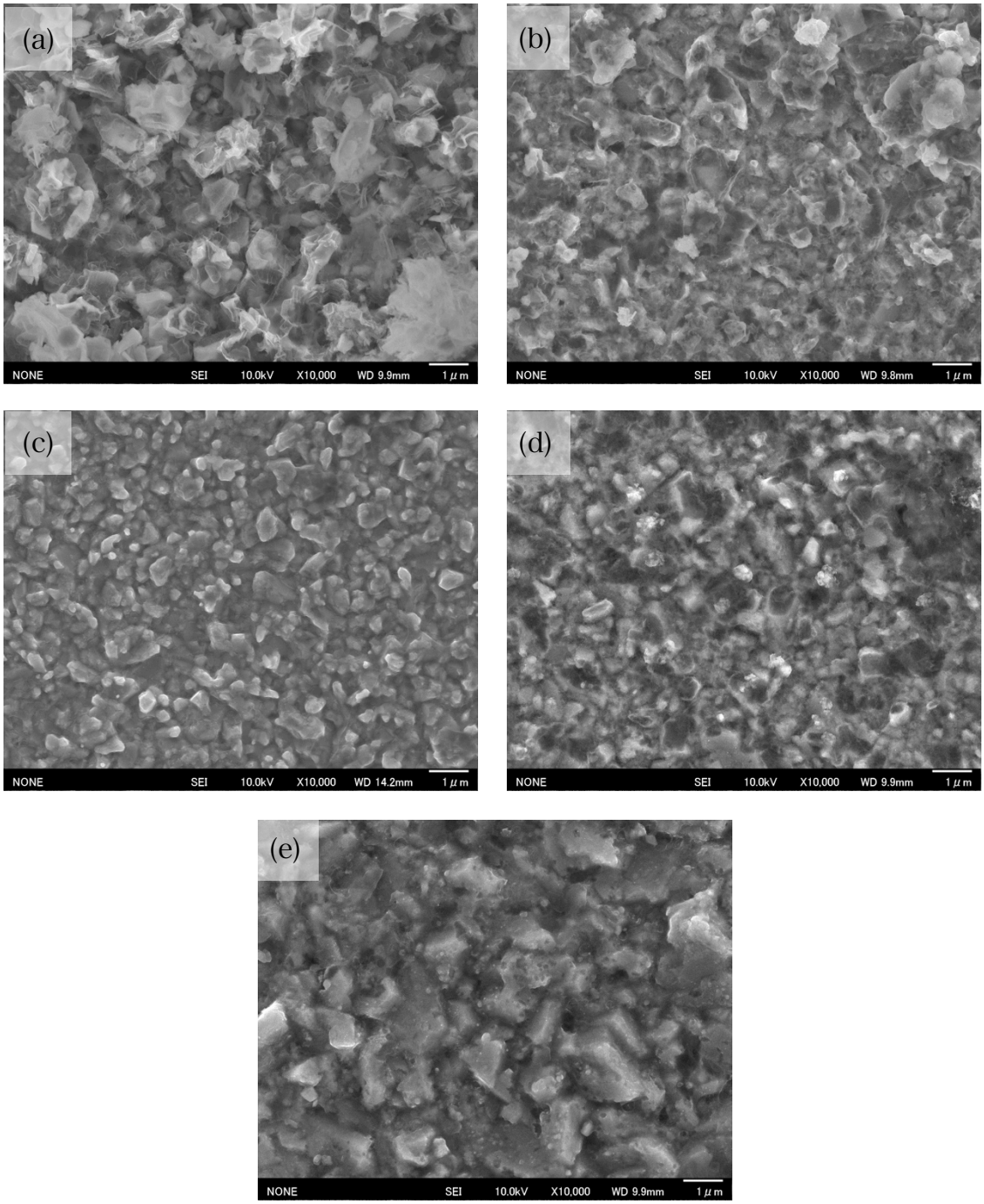


Fig. 3-3-3-1. Surface SEM images of Al-Zn co-electrodeposits obtained with potentiostatic polarization at (a) –0.1, (b) –0.2, (c) –0.3, (d) –0.4, and (e) –0.5 V vs. Al-RE after heat treatment at 350ºC for 1 h in N_2 gas.

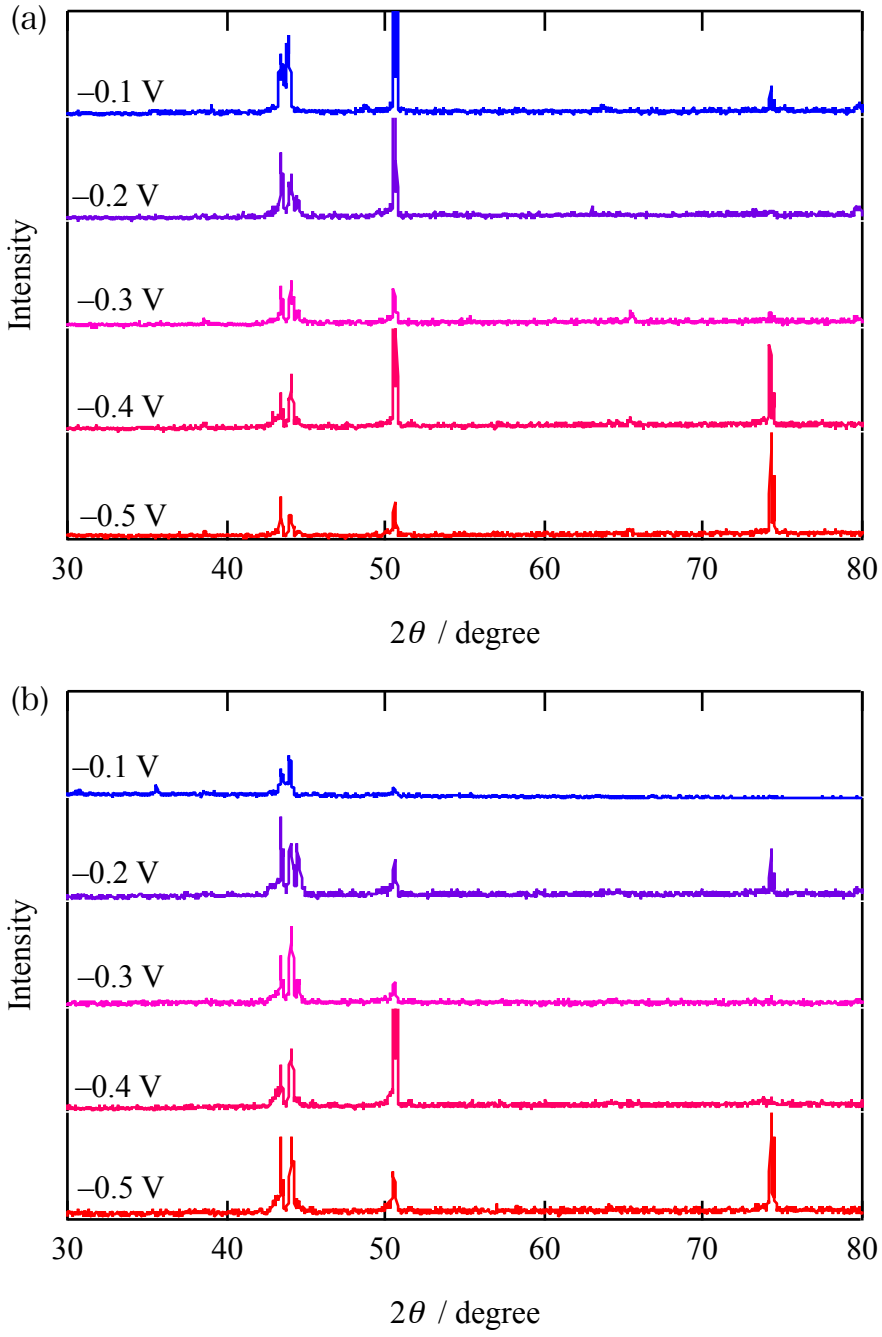


Fig. 3-3-3-2. XRD pattern measured for Al-Zn co-electrodeposits obtained with potentiostatic polarization at –0.1, –0.2, –0.3, –0.4, and –0.5 V vs. Al-RE after heat treatment for (a) 10 min. and (b) 1 h in N_2 gas.

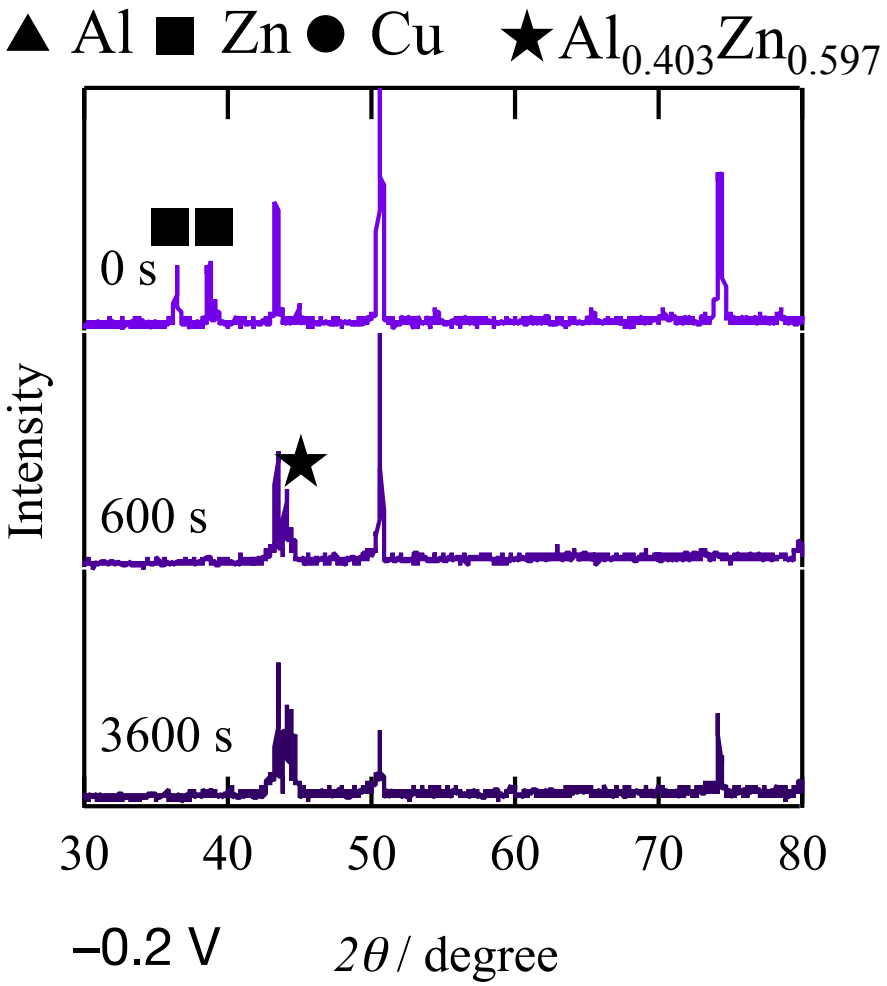


Fig. 3-3-3-3. Transition of XRD pattern of Al-Zn co-electrodeposits obtained with potentiostatic polarization at –0.2 V vs. Al-RE with heat treatment time in N_2 gas.

3.4. Conclusions

In this experiment, both Al and Zn were electrodeposited from an $AlCl_3$-$ZnCl_2$-EMIC bath. The composition of coatings depended on the electrodeposition potential. The composition ratio of Zn increased with applied noble electrodeposition potential. The electrodeposits consisted of simple substance of Al and Zn. However, the heat treatment at the temperature lower than hot-dip process can change the structure of coatings and $Al_{0.403}Z_{0.597}$ was obtained.

Reference

[1] T. Prosec, D. Persson, J. Stoulil, D. Thierry, *Corros. Sci*. **86** (2014) 231.

[2] H.C. Shih, J.W. Hsu, C.N. Sun, S.C. Chung, *Surf. Coat. Technol*. **150** (2002) 70.

[3] P.R. Seré, M. Zapponi, C.I. Elsner, A.R. Di Sarli, *Corros. Sci*. **40** (1998) 1711.

[4] D. Laverde, j.C. Zubillaga, J.G. Sevillano, E. Vilaueva, *Corros. Sci*. **37** (1995) 79.

[5] R. Sagl, A. Jarosik, D. Stifter, G. Angeli, *Corros. Sci*. **70** (2013) 268.

[6] G.M. Song, T. Vystavel, N. van der Pers, J.Th.M. De Hosson, W.G. Sloof, *Acta Meter*. **60** (2012) 2973.

[7] S. Prabhudev, S. Swaminathan, M. Rohwerder, *Corros. Sci*. **53** (2011) 2413.

[8] Q.X. Liu, S. Zein El Abedin, F. Endres, *Surf. Coat. Technol*. **201** (2006) 1352.

[9] Y.F. Lin, I.W. Sun, *Electrochim. Acta* **44** (1999) 2771.

[10] J.K. Chang, S.Y. Chen, W.T. Tsai, M.J. Deng, I.W. Sun, *Electrochem. Commun*. **9** (2007) 1602.

[11] T. jiang, M.J. Chollier Brym, G. Dubé, A. Lasia, G.M. Brisard, *Surf. Coat. Technol*. **201** (2006) 1.

[12] S.I. Hsiu, J.F. Huang, I.W. Sun, C.H. Yuan, J. Shiea, *Electrochim. Acta* **47** (2002) 4367.

Chapter 4. Al-Zn co-electrodeposition by a double counter electrode electro-deposition system from an $AlCl_3$-1-ethyl-3-methylimidazolium chloride ionic liquid bath

4.1. Introduction

Zinc alloy coatings have been widely used for corrosion protection of steels. Among various alloy coatings, Zn-Al coatings provide excellent anticorrosion performance, as mentioned in Chapter 3 [1-4]. A hot-dip process has been used to form the Al-Zn alloy galvanized coatings on steels. However, this process forms intermetallic compounds and the oxides on the substrate steel due to high temperature operation and sometimes lessens the adhesion of coatings [5-7]. Precise control of the thickness and uniformity of coatings to improve the performance and to reduce the use of Zn resources is another issue of the hot-dip process. Alternative methods for Al-Zn coating at a low temperature such as electrodeposition methods have therefore been investigated. Not only the composition but also the macro- and micro-structures of the alloy or co-deposit coatings can be modified depending on the intended use by changing the electrodeposition potential or current density (deposition rate), bath composition and rate of the supply of ions from the electrodeposition bath. For example, large current density may enable rapid nucleation of deposits with a high density on the substrate at the initial stage of electrodeposition. However, rapid growth of nuclei may also result in a less dense deposit composed of dendritic crystal and voids or defects. Compositional change of coatings in the depth direction caused by change in bath composition during the plating process may also be considered.

For electrodeposition of Zn-Al alloy coatings, a non-aqueous bath must be used because the deposition potential of Al is very less noble than the hydrogen evolution potential due to water decomposition. An ionic liquid bath such as a mixture of 1-ethyl-3-methylimidazolium chloride (EMIC) and metal chloride salts has been used for investigation of Al electrodeposition [8-13]. In an acidic EMIC-$AlCl_3$ ionic liquid bath at high concentration of Al^{3+} ions, it has been suggested that the dominant complex ions of $Al_2Cl_7^-$ are electrochemically reduced to form Al deposits as [11]

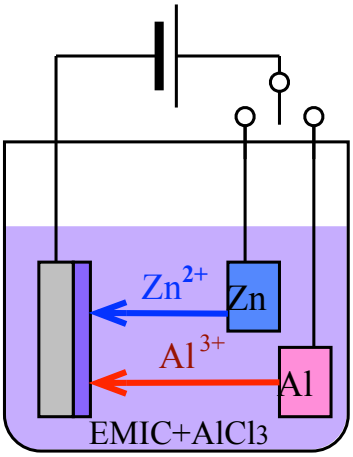
$$4Al_2Cl_7^- + 3e^- \rightarrow 7AlCl_4^- + Al.$$

If the molar ratio of $AlCl_3$ to EMIC is low as less than 1, however, only $AlCl_4^-$ presents and

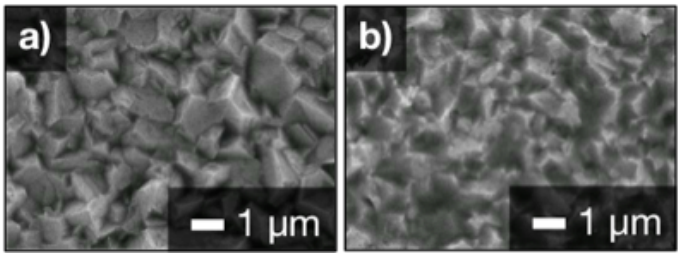
electrodeposition of Al hardly occurs. In the case of Zn electrodeposition in the acidic EMIC-$ZnCl_2$ bath, it has been proposed that Zn is electrodeposited from a $ZnCl_3^-$, $Zn_2Cl_5^-$ or $Zn_3Cl_7^-$ complex depending on the bath acidity [12]. In a neutral bath, however, predominant $ZnCl_4^{2-}$ ion is less reactive to the electrodeposition reaction [12].

Co-electrodeposition of Al-Zn from an EMIC-based ionic liquid bath was also examined. Composition and structure of co-electrodeposits of Al-Zn from an EMIC-$AlCl_3$-$ZnCl_2$ bath were reported to depend on the deposition potential [13]. Generally, the composition of co-electrodeposits is limited in a range constrained by the electrochemical properties of different metals such as different electrodeposition potentials, deposition ratio and concentration of ions in the plating bath. To control coating composition more arbitrary, a more flexible technique is desired.

In this work, therefore, a double counter electrodes electrodeposition system (DCES) was first developed. In this system, two counter electrodes of different metals are used as a source of ion supply to the bath, and the rate of ion supply is controlled by switching the active counter electrodes for anodic dissolution during the electrodeposition. The switching of counter electrodes alters the bath composition and thus influences the composition of deposits. As discussed in Chapter 3, addition of Zn ions to EMIC-$AlCl_3$ bath enables Zn-Al electrodeposition and its composition can be controlled by the deposition potential because Zn deposits preferentially electrodeposited than Al due to its relatively noble redox potential. From this result a prototype DCES was designed to use EMIC-$AlCl_3$ bath and Zn C.E. as a Zn ion supplier to control Zn content by the dissolution of Zn C.E. In the pilot experiments of DCES, electrodeposits of Al containing small amount of Zn were also obtained. The content of Zn in the deposits, however, quite small because the volume of the bath was considerably large comparing with dissolving Zn-C.E., i.e., plating bath acts as a large buffer for Al ions.



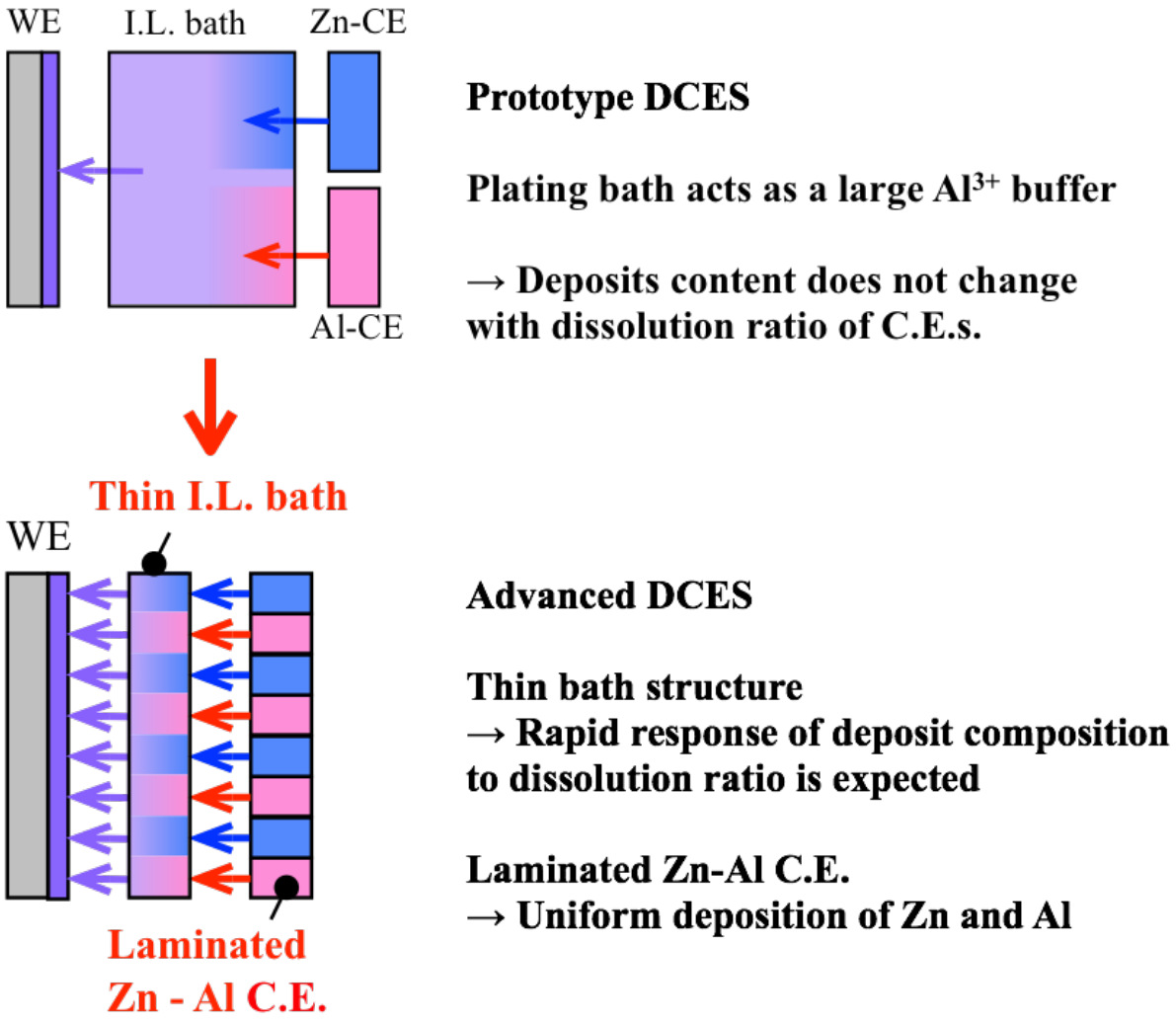
$Q_{Zn} : Q_{Al}$	5 : 1	1 : 5
X_{Zn} / at %	1	2



Left : Concept of a double counter electrodes electrodeposition system (DCES) developed in this work. *Right* : Typical results of electrodeposits and their composition.

In the work of this chapter, therefore, advanced DCES was designed in which (a) a thin ionic liquid bath structure and (b) laminated Al and Zn counter electrodes are used. A thin bath structure enables rapid change in ionic bath composition by changing the dissolution ratio of Al and Zn C.E.s and thus considerable modulation of deposit composition is expected. An integrated counter electrode composed of laminated Zn and Al sheets enables uniform dissolution of Al and Zn ions from the C.E. surface and thus uniform electrodeposition of Al and Zn on a W.E.

In this chapter, DCES was developed and applied to electrodeposition Al-Zn on Cu plate. To evaluate this new electrodeposition technique, relationships between the composition of the coatings deposited using the DCES and deposition conditions such as current density, electric charges of the two different counter electrodes, and distance between the working electrode and the counter electrodes were investigated.



Design of an advanced DCES using a thin electrolyte bath and laminated multi-counter electrodes.

4.2. Experimental

An ionic liquid (IL) bath was prepared by using the following procedure. Anhydrous $AlCl_3$ powder (Junsei Chemical Co., 98% in purity) was added slowly to 1-ethyl-3-methylimidazolium chloride (EMIC, Merck Co.) IL to reach a molar ratio of $AlCl_3$:EMIC = 2:1. Then an Al wire (Nilaco Co., 99.999% in purity) was immersed in the bath at 80ºC for 2 days to remove residual impurities such as water [14]. After this pretreatment, a transparent solution with slightly yellow color to be used for electrodeposition was obtained.

The DCES is schematically shown in **Fig. 4-2-1**. The electrochemical cell was composed of metal plates and silicone rubber sheets tightened with screws. The working

electrode (WE) was a Cu plate (Nilaco Co., 99.5% in purity, 0.5 mm in thickness). The surface of the WE was covered with nitoflon®(Nitto Denko Co.) tape except for the electrode area of 1 cm^2. Prior to electrodeposition, the Cu-WE surface was polished with diamond abrasive of 1 μm in average particle size. An integrated counter electrode (CE) was constructed from many Zn and Al sheets (1.5 x 1.0 x 0.2 mm) (**Fig. 1 (b,c)**). The two faces of each sheet were electropainted for electric insulation to each other, piled alternatively, and embedded in epoxy resin. The top Al sheets was used as a reference electrode (RE) to be accommodated in a narrow cell. All of the Al sheets except for the RE and all of the Zn sheets were connected to Cu rods via a through-hole to establish electric connection to be used as Al-RE, Al-CE and Zn-CE. Then the surfaces of CEs were ground with #800 emery paper to expose the Al-CE and Zn-CE surfaces alternatively arranged in the comb-formed electrodes. After incorporating the CEs into the electrochemical cell, the cell was filled with $AlCl_3$-EMIC ionic liquid. The volume of the IL bath was limited to a small volume of *ca*. 0.18, 0.26 or 0.9 cm^3 to obtain reasonable time-responses of concentration changes of ions supplied from the CEs. The distance between the WE and the CE was d_{WC} = 1, 2 or 5 mm.

An integrated electrochemical system (Ivium technologies Co., model Iviumstat) and two additional photo-MOS relays driven by external digital ports of Iviumstat for switching two CEs were used in the DCES. Electrodeposition was conducted using a pulse method as shown in Fig. 1(d). The pulse method has been sometimes used to improve the flatness of the electrodeposit by mitigating the depletion of ion supply in the electrodeposition period. The WE was periodically subjected to galvanostatic cathodic polarization with a timing of t_{ON} = 1 s and t_{OFF} = 1 s, and Al-CE and Zn-CE were periodically switched alternately with a pulse number of N_{Al} and N_{Zn}. The ratio of the electric charge on Zn-CE, q_{Zn}, against the total polarization charge, q, was obtained from the pulse number ratio as

$$r_{Zn} = q_{Zn} / q = N_{Zn} / (N_{Zn}+N_{Al}). \quad (1)$$

The value of r_{Zn} was chosen to be 0.2 (N_{Al} : N_{Zn} = 2 : 8), 0.5 (5 : 5) or 0.8 (8 : 2). The pulse current density was j_C = –2, –5 or –10 mA cm^{-2}, and the electrodeposition charge was fixed to be q = 15 C cm^{-2}. After electrodeposition, the Cu-WE was rinsed with ethanol and acetone and then dried in an air stream. The whole system was operated by a batch sequence built

with the programmable function of bundle software (Iviumsoft).

The surface and cross-sectional morphology and the elemental composition of deposits were investigated by using SEM and EDX (JEOL Ltd. model JSM-6500F). The composition obtained by EDX analysis was averaged at multiple points of the surface and cross section. The coulometric efficiency η of the electrodeposition was calculated from the following equation:

$$\eta = \frac{F}{q}\sum\frac{n_i \Delta w_i}{M_i}, \qquad (2)$$

where n_i is the number of electrons for electrodeposition reaction of each element i (Al or Zn), Dw_i is the weight gain of element i due to electrodeposition, M_i is atomic weight, and F is the Faraday constant.

The coulometric efficiency of Zn electrodeposition, η_{Zn}, which is defined by the rate of electrodeposited Zn at WE to dissolved Zn at Zn-CE, was also calculated from the following equation;

$$\eta_{Zn} = \frac{F}{q_{Zn}}\frac{n_{Zn}\Delta w_{Zn}}{M_{Zn}}$$

where n_{Zn} is the number of electrons used for electrodeposition of Zn, Dw_{Zn} is the weight gain due to electrodeposition of Zn, M_{Zn} is atomic weight of Zn.

The concentration of Zn (II) suppose to be existed as the complexes in the bath after electordeposition, $C_{Zn,sol}$ was calculated by the charge efficiency, h_{Zn}, by following equation;

$$C_{Zn,sol} = (1-\eta_{Zn})\frac{q_{Zn}}{FV_{sol}}$$

where V_{sol} is the volume of electrolyte solution during electrodeposition.

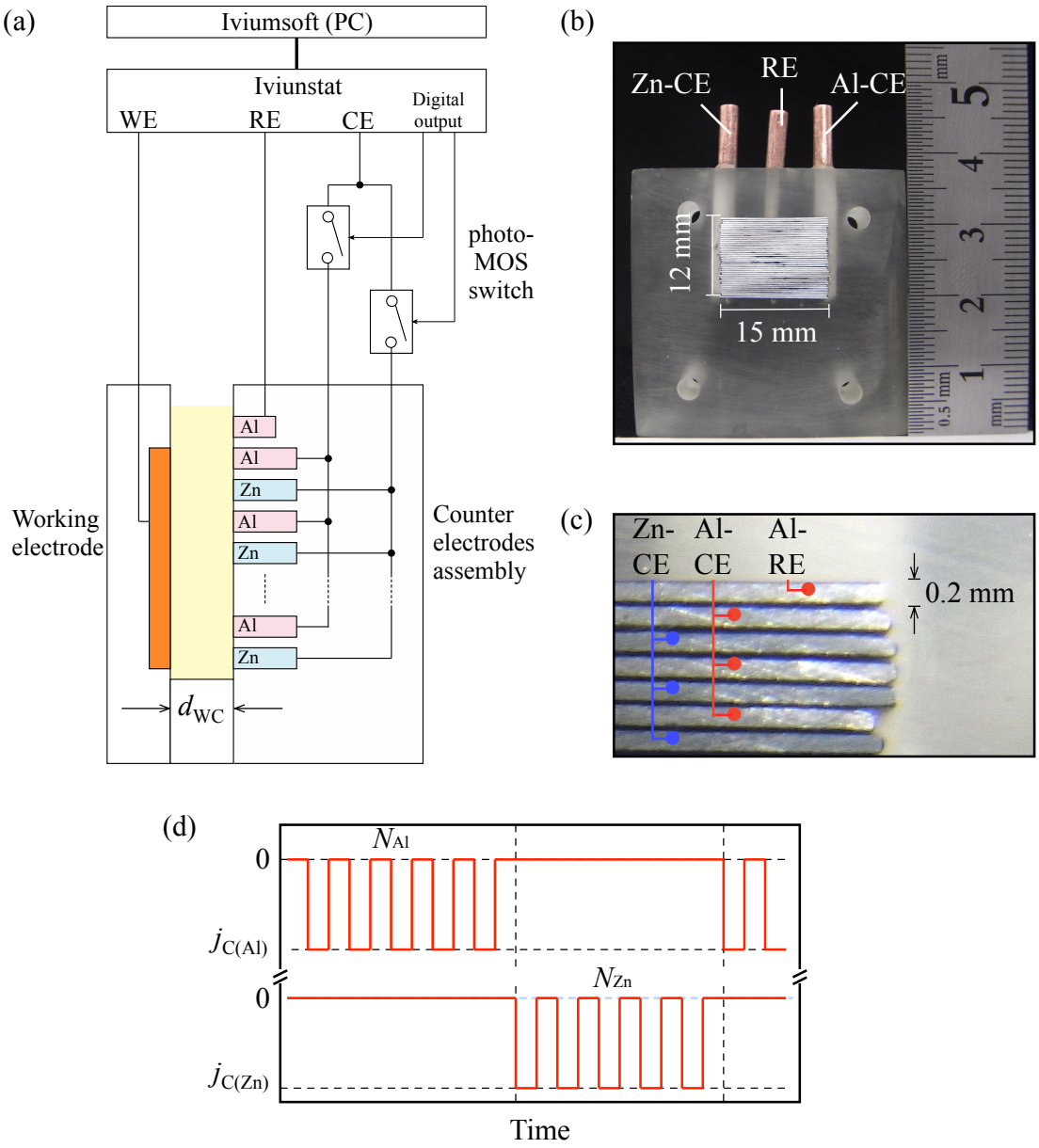


Fig. 4-2-1. (a) Schematic diagram of the double counter electrode electrodeposition system, (b) photograph of the counter electrode assembly, (c) magnified image of the counter electrode surface framed by the dotted square in Fig. 1(b), (d) timing scheme of galvanostatic pulse. $j_{C(Al)}$ and $j_{C(Zn)}$ are current densities on Al and Zn counter electrodes, respectively.

4.3. Results

4.3.1. Potential transient

Transitions of electrode potential Φ during the pulse electrodeposition at different j_C and d_{WC} are shown in **Fig. 4-3-1-1**. Most of the Φ-t curves show a rectangle shape corresponding to the rectangular current pulse. The value of Φ was less noble when Zn-CE or

Al-CE was activated. The value of Φ for Zn-CE was droped with increase of j_C as Φ = *ca.* –0.5 V at j_C = –2 mA cm^{-2} and Φ = –1.7 V at j_C = –10 mA cm^{-2} as shown in Fig. 2(a). The Φ also depended on d_{WC} as seen in Fig. 2(b). The relationship between Φ and d_{WC} was not monotonous, and the lowest Φ = *ca.* –1.4 V was observed for Zn-CE and Al-CE at d_{WC} = 2 mm. Non-rectangular behavior of the Φ-*t* curve was observed for Al-CE at j_C = –10 mA cm^{-2} and d_{WC} = 2 mm and at j_C = –5 mA cm^{-2} and d_{WC} = 1 mm. These transitions of the Φ-*t* curve seem to reflect the change in the composition and transport mechanism of ions in the bath, as discussed later.

Fig. 4-3-1-2 shows the long-term transition of electrode potential Φ during the electrodeposition at j_C = –10 mA cm^{-2} and d_{WC} = 1 mm. In the figure Φ is plotted separately for the dissolution periods of Al-CE and Zn-CE, respectively. The Φ during Al-CE dissolution was in a range of –1.0 and –1.7 V until 1.7 ks and shifted rapidly in a less-noble direction to reach around –3 V after 2000 s. The Φ in the Zn-CE dissolution period showed a similar tendency. The Φ in the Al-CE dissolution period was in the range of –0.7 V and –1.1 V, *ca*. 0.5 V nobler than that for Zn-CE dissolution period. The Φ was then reached *ca*. –3 V after 2000 s as that for Zn-CE dissolution period. As seen in time expansion of Φ plots in **Fig. 4-3-1-2 (b, c)**, Zn-CE dissolution period showed potential transition for every current pulse while Al-CE dissolution period showed only a single transition reflecting probably the difference of dissolution process of Zn CE and Al-CE, as discussed later.

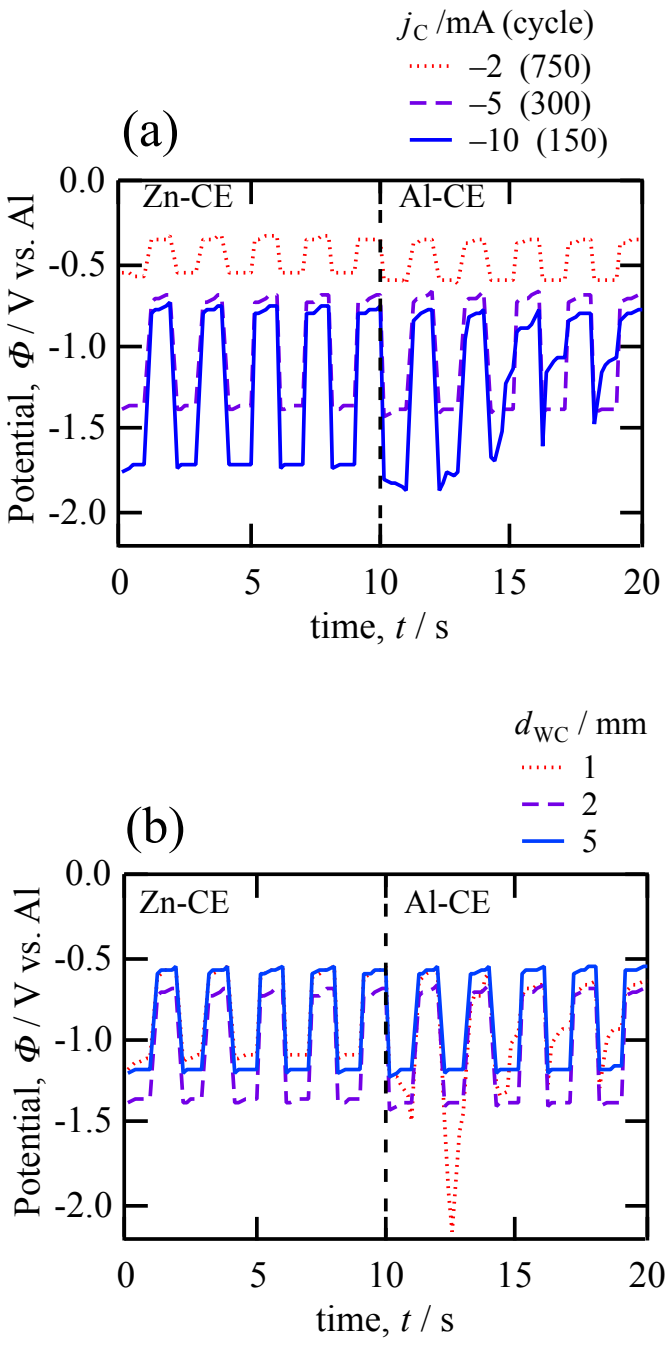


Fig. 4-3-1-1. Transition of the polarization potential Φ during the pulse electrodeposition as a function of (a) different current density j_C at distance between the working electrode and counter electrodes d_{WC} = 2 mm, (b) different d_{WC} at j_C = –5 mA cm^{-2} and 300 cycle.

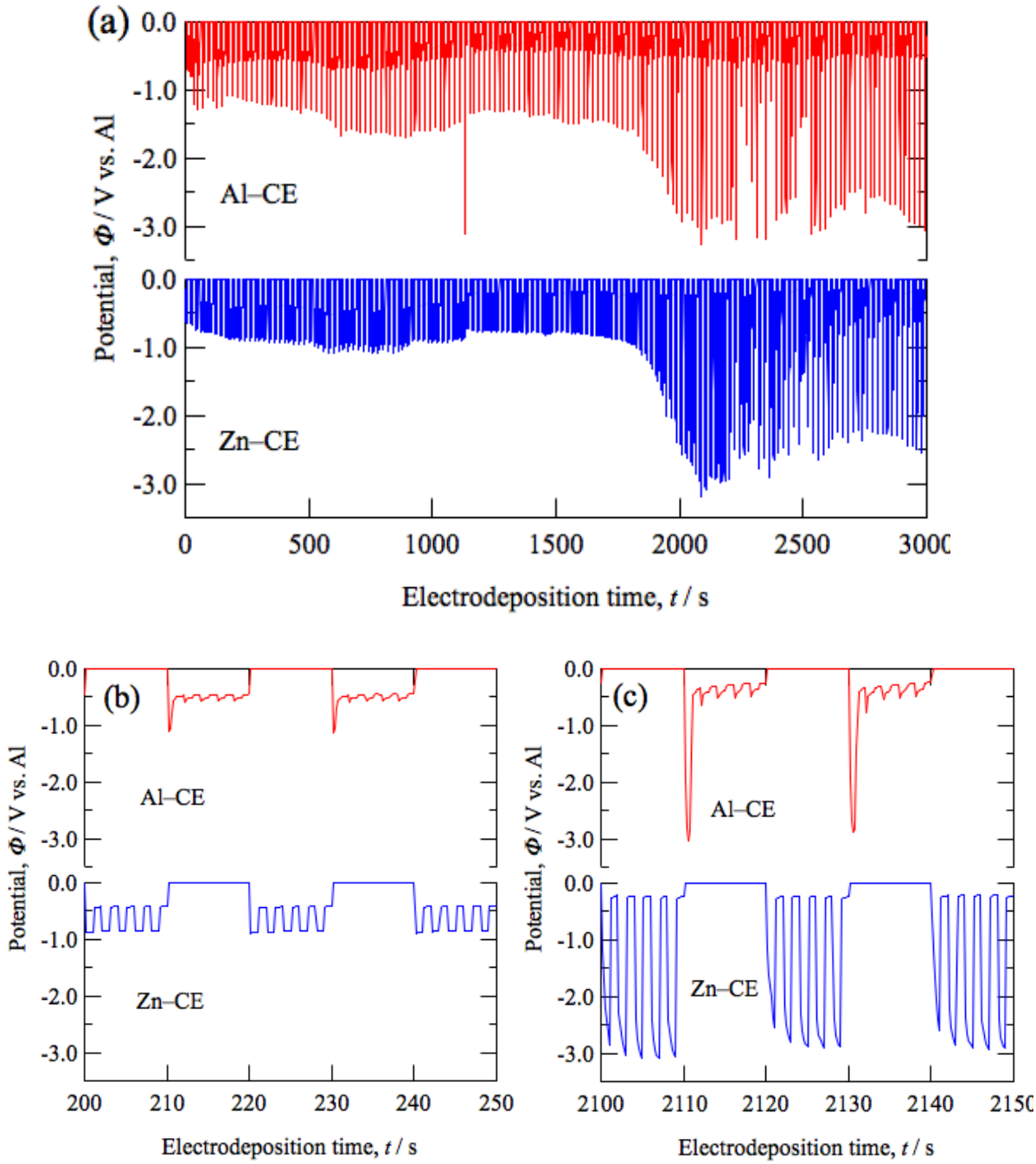


Fig. 4-3-1-2. (a) Transition of the polarization potential F during the pulse electrodeposition at j_C = –10 mA cm^{-2} and d_{WC} = 1 mm. The F is plotted separately for Al-CE dissolution period and Zn-CE dissolution period, respectively. (b,c) Time expansion of upper plot.

4.3.2. Surface morphology of electrodeposits

The morphology of electrodeposits depended on the location of the sample. **Fig. 4-3-2-1** and **Fig. 4-3-2-2** show the SEM images of the top and bottom side of the coatings electrodeposited on Cu sample at different j_C and d_{WC}. The surface tends to show rough

morphologies at low j_C and low d_{WC} and becomes fine with increasing j_C and d_{WC} at the both top and bottom sides. From the comparison of top side (Fig. 4-3-2-1) and bottom side (Fig. 4-3-2-2) morphologies, the surface at the bottom side is rougher than that at the top side, specially at low j_C and d_{WC}.

The composition of the coatings is also affected by d_{WC} and the location of deposits. The Zn content at the top ($X_{Zn,T}$), center ($X_{Zn,C}$) and bottom ($X_{Zn,B}$) of the coatings as a function of d_{WC} obtained by EDX spectra is summarized in **Table 4-3-2-1**. High Zn content was obtained in the order of d_{WC} = 2, 5, 1 mm. Higher Zn content was also obtained at the bottom of the coatings at d_{WC} = 2 and 5 mm. This tendency will be discussed later in term of ion transportation mechanism in the thin ionic liquid bath.

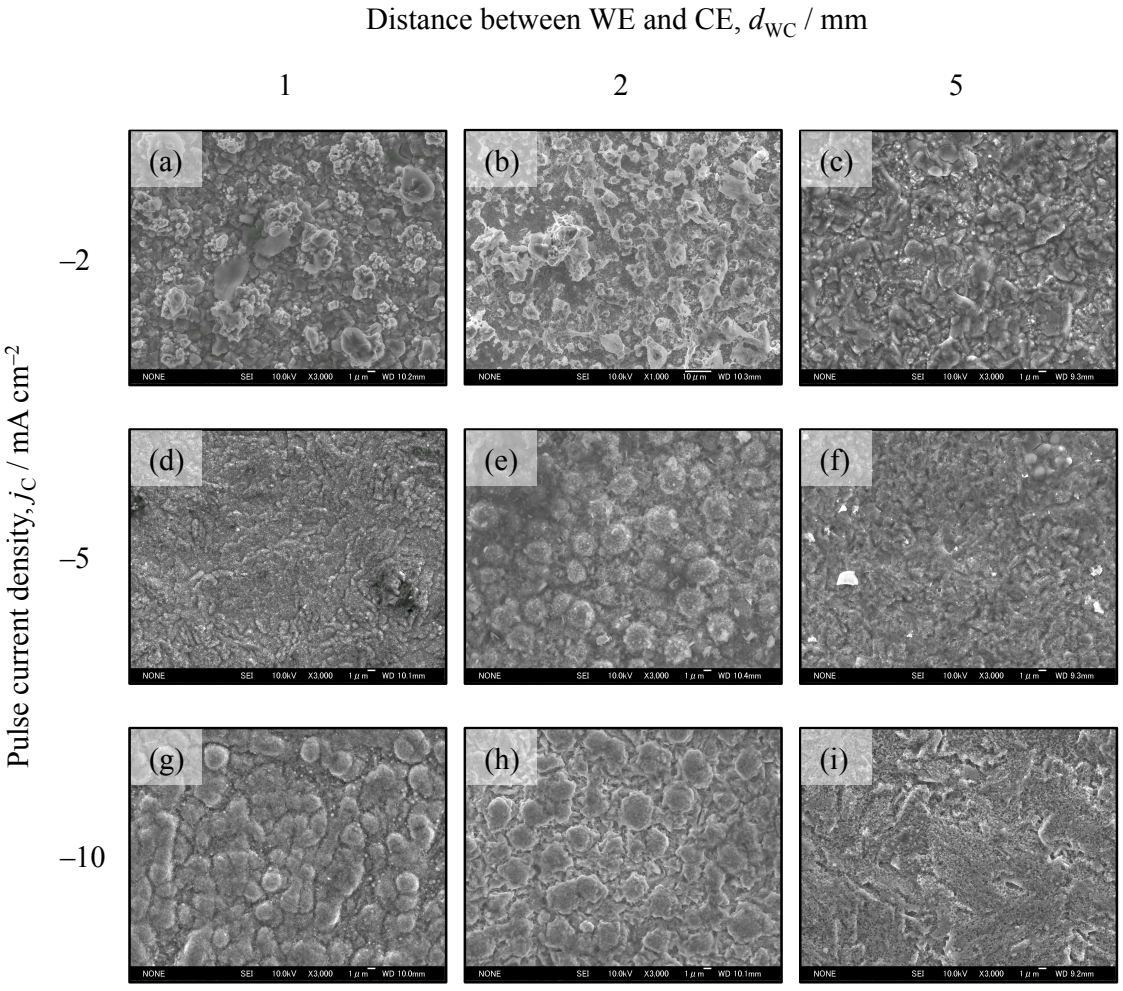
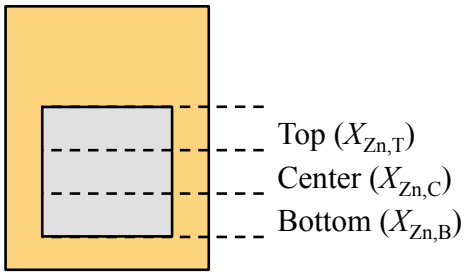


Fig. 4-3-2-1. SEM images at the top side of Al-Zn coatings electrodeposited on Cu as a function of pulse current density (j_C = –2, –5, and –10 mA cm^{-2}) at r_{Zn} = 0.5 in vertical column and distance between W.E. and C.E. (d_{WC} = 1, 2 and 5mm) in the lateral column, respectively.

Table 4-3-2-1. Composition of Zn at top, center and bottom surface of the coatings electrodeposited at j_C = –5 mA cm^{-2}, r_{Zn} = 0.5, and d_{WC} = 1, 2 and 5 mm.

$d$wc / mm	1	2	5
$X_{Zn,T}$ / %	43.7	63.1	43.7
$X_{Zn,C}$ / %	47.6	64.3	53.7
$X_{Zn,B}$ / %	37.7	76.4	66.4



4.3.3. Compositional depth profile in the deposits

Fig. 4-3-3-1 shows cross-sectional SEM images and elemental profile measured by EDX line scan for coatings deposited using the conditions of r_{Zn} = 0.5, j_C = –5 mA cm^{-2} and d_{WC} = 1, 2, 5 mm. The EDX profiles for all d_{WC} reveals that the signal of Zn, I_{Zn}, in the coating near the substrate was relatively low, corresponding to the absence of Zn ions in the bath at the initial stage of the electrodeposition. The value of I_{Zn} then increased gradually with thickening of the coating due to increasing concentration of Zn ions in the bath. Although the profile of signal I_{Zn} is not clear because of its weak intensity compared to that of Al, it can be estimated from the complemental relationship of I_{Zn} to the I_{Al} profile in the binary system. The I_{Al} profile at d_{WC} = 1 mm shows a plateau while those at d_{WC} = 2 and 5 mm show a monotonous decrease toward the surface of the coating. This indicates that the concentration of Zn ions in the bath might reach a steady states at d_{WC} = 1 mm more rapidly than that at d_{WC} = 2 and 5 mm because of the small volume of the former.

The value of I_{Zn} at d_{WC} = 2 mm was considerably larger than those of the other two samples and increased continuously in the coating toward the surface as shown in Fig. 4 (c). This means that the Zn deposition proceeded more efficiently compared to Al deposition at d_{WC} = 2 mm than at other values of d_{WC}.

For further investigation, EDS point analysis was conducted at a few points of the cross sections of coatings. **Fig. 4-3-3-2** shows the depth profiles of atomic ccomposition of Zn in the deposits, X_{Zn}, electrodeposited at different d_{WC}. The horizontal scale is a normalized distance x from the substrate (x = 0) to the coating surface (x = 1). In all deposits, X_{Zn}

increased with x and thus X_{Zn} was highest at the surface of the coatings. The value of X_{Zn} was 30-35 at.% at x = 1 and d_{WC} = 1 or 5 mm, and the averaged value of X_{Zn} over the coatings was *ca*. 25 at.%. On the other hand, the value of X_{Zn} was almost 60 at.% at x = 1 and d_{WC} = 2 mm, and the averaged value of X_{Zn} was *ca*. 40 at.%. The value of X_{Zn} increased monotonically with x at d_{WC} = 2 mm, while the X_{Zn} profile showed a plateau at d_{WC} = 1 and 5 mm.

The X_{Zn} profile is plotted as a function of j_C at d_{WC} = 2 mm in **Fig. 4-3-3-3**. The value of X_{Zn} increased almost monotonically with x and with decrease in j_C. The value of X_{Zn} at x = 1 was *ca*. 45 at.% at j_C = –10 mA cm^{-2} and was almost 80 at.% at j_C = –2 mA cm^{-2}.

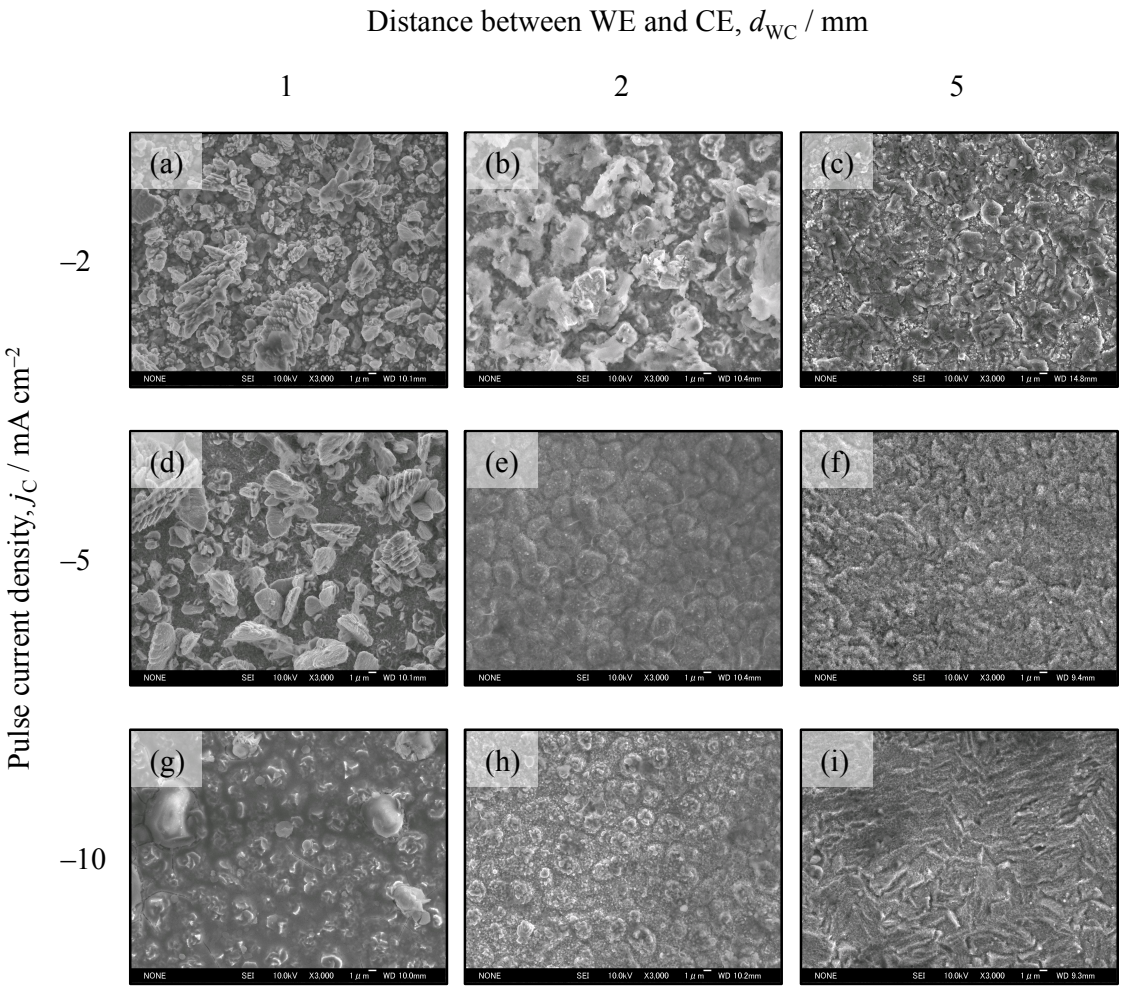


Fig. 4-3-2-2. SEM images at the bottom side of Al-Zn coatings electrodeposited on Cu as a function of pulse current density (j_C = –2, –5, and –10 mA cm^{-2}) at r_{Zn} = 0.5 in vertical column and distance between W.E. and C.E. (d_{WC} = 1, 2 and 5mm) in the lateral column, respectively.

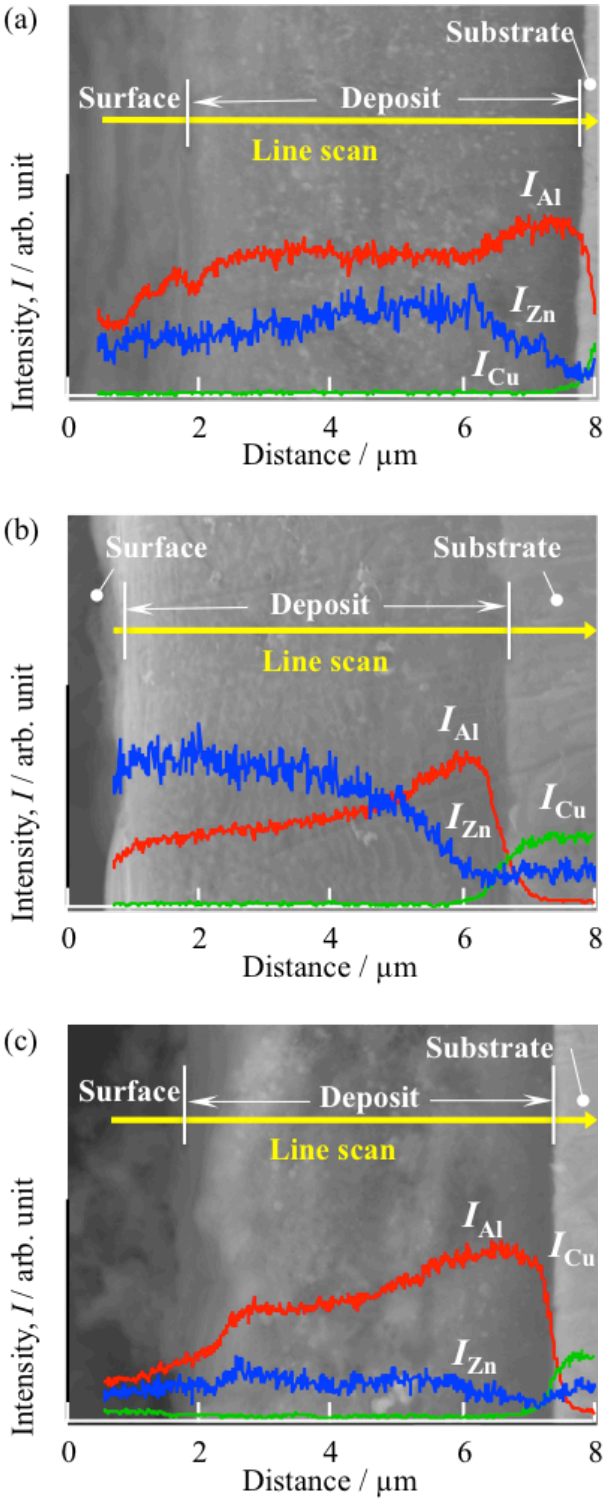


Fig. 4-3-3-1. Cross-sectional SEM images and elemental depth profile obtained by EDX in the Al-Zn coating electrodeposited at j_C = –5 mA cm^{-2}, r_{Zn} = 0.5, and d_{WC} = (a) 1 mm, (b) 2 mm, and (c) 5 mm.

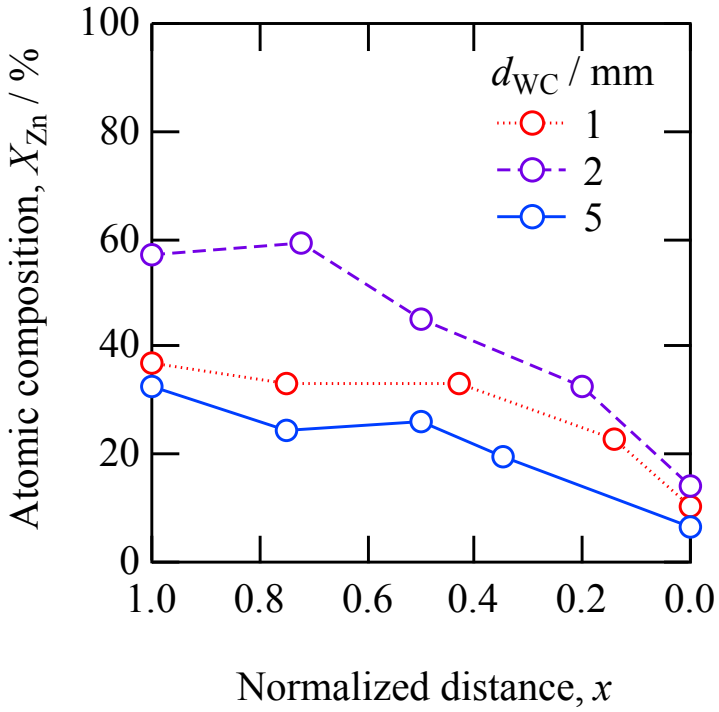


Fig. 4-3-3-2. Depth profile of Zn atomic composition X_{Zn} in the Al-Zn coating deposited at j_C = –5 mA cm^{-2}, r_{Zn} = 0.5, and d_{WC} = 1, 2 and 5 mm.

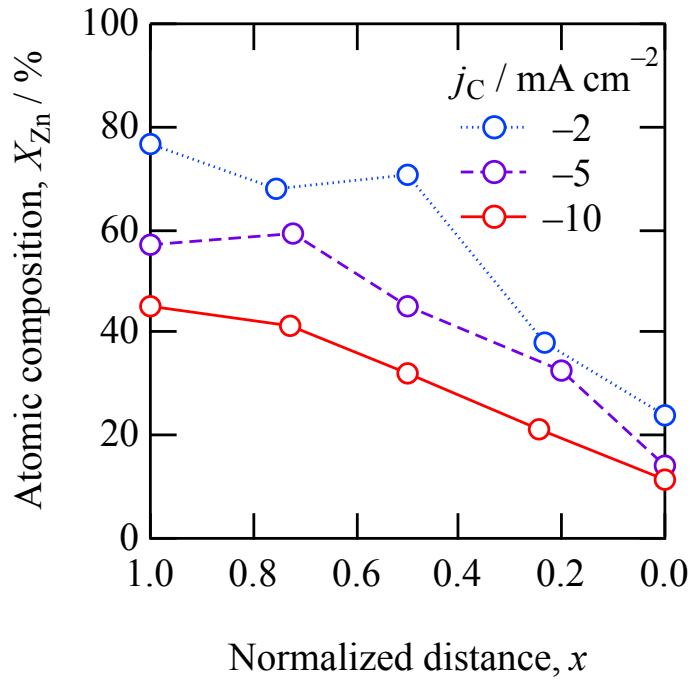


Fig. 4-3-3-3. Depth profile of Zn atomic composition X_{Zn} in the Al-Zn coating electrodeposited at j_C = –2 , –5, and –10 mA cm^{-2}, r_{Zn} = 0.5, and d_{WC} = 2 mm.

4.3.4. Effect of charge ratio on atomic composition of deposits

The X_{Zn} behavior was also investigated as a function of r_{Zn} at different d_{WC} as shown in **Fig. 4-3-4-1**. It is reasonable that X_{Zn} increased with increase in r_{Zn}. The broken line in the plot is the value of X_{Zn} calculated from the dissolution ratio r_{Zn}, *i.e.*, expected composition of deposits at a steady state. It is obvious that the experimental value of X_{Zn} is fairly close to the predicted value. The value of X_{Zn} also depended on d_{WC} and was largest at d_{WC} = 2 mm as already shown in Fig. 4-3-3-2.

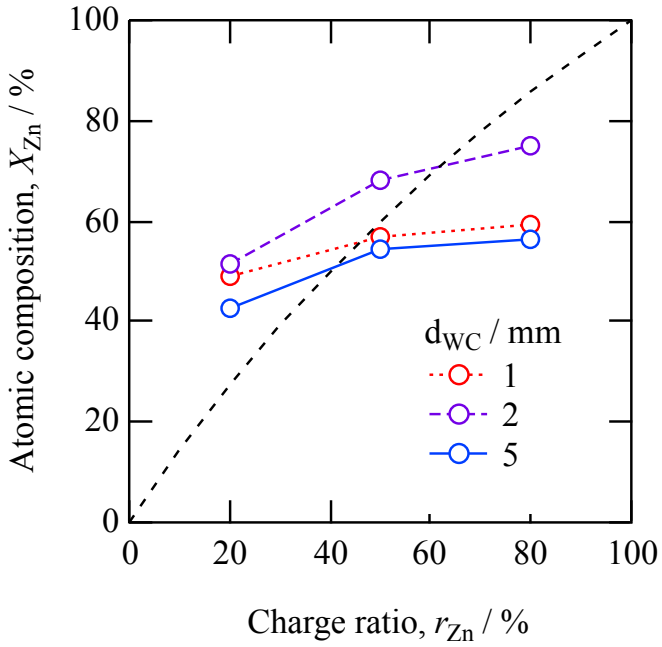


Fig. 4-3-4-1. Dependence of averaged Zn atomic composition X_{Zn} in the Al-Zn coating on the charge ratio of Zn-CE; $r_{Zn} = q_{Zn} / q$. Broken line was calculated assuming the steady state of anodic dissolution on CEs and electrodeposition on WE.

4.3.5. Coulometric efficiency of electrodeposition

The coulometric efficiency η of the electrodeposition at different j_C and d_{WC} calculated from Eq. 2 is plotted in **Fig. 4-3-5-1**. The value of η was almost constant against j_C but depended on d_{WC}, being *ca.* 60% at d_{WC} = 5 mm and being 70-80% at other values of d_{WC}. The coulometric loss in electrodeposition may be due to side reactions such as decomposition of residual water contained in the bath since gas evolution was observed in the cell during the electrodeposition.

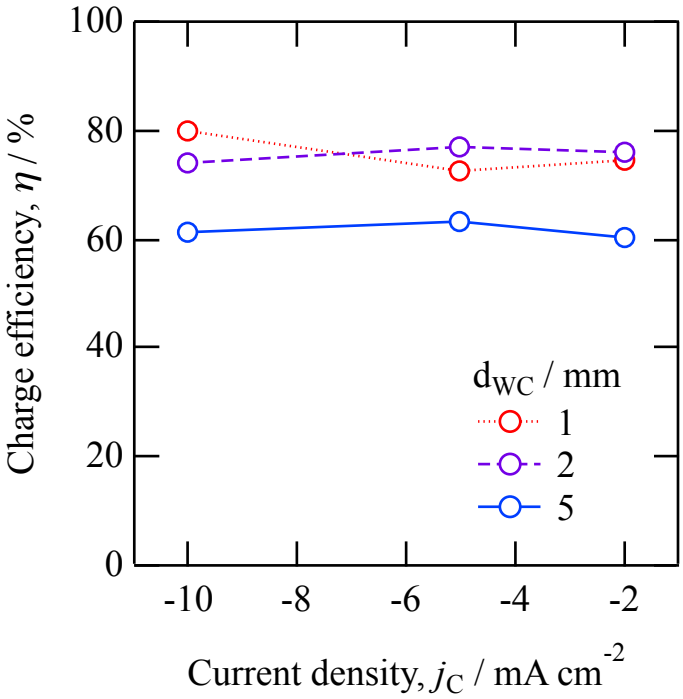


Fig. 4-3-5-1. Coulometric efficiency η of electrodeposition calculated from Eq. 1 in the text as a function of current density j_C at d_{WC} = 1, 2 and 5 mm.

4.3.6. Efficiency of Zn electrodeposition

In the DCES, electrodeposition efficiency of each dissolving element can be estimated from the composition profile of electrodeposit and dissolution charge of CE of each element. **Fig. 4-3-6-1** shows the dependence of η_{Zn} on d_{WC} calculated from the composition of Zn in the electrodeposits shown as Fig. 4-3-3-2 and Fig. 4-3-3-3 and dissolution charge of Zn-CE. The η_{Zn} increased with increasing r_{Zn}, *i.e.* increasing with dissolution charge of Zn-CE, as h_{Zn} = 0.47 at r_{Zn} = 50% and h_{Zn} = 0.67 at r_{Zn} = 80%. On the other hand, the highest h_{Zn} = 0.90 was obtained at d_{WC} = 1 mm and the lowest h_{Zn} was obtained at d_{WC} = 5 mm for each r_{Zn}. The concentration of residual Zn (II) in the bath, $C_{Zn,sol}$ at d_{WC} = 1, 2 and 5 mm calculated from h_{Zn} is shown in **Fig. 4-3-6-2**. For all d_{WC}, C_{Zn} increased linearly with increase of r_{Zn} as C_{Zn} = 6.0 μmol cm^{-3} at r_{Zn} = 20% to C_{Zn} = 1.5x10^2 μmol cm^{-3} at r_{Zn} = 80% at d_{WC} = 1 mm. On the other hand, C_{Zn} increased non-linearly at d_{WC} = 2 and 5 mm.

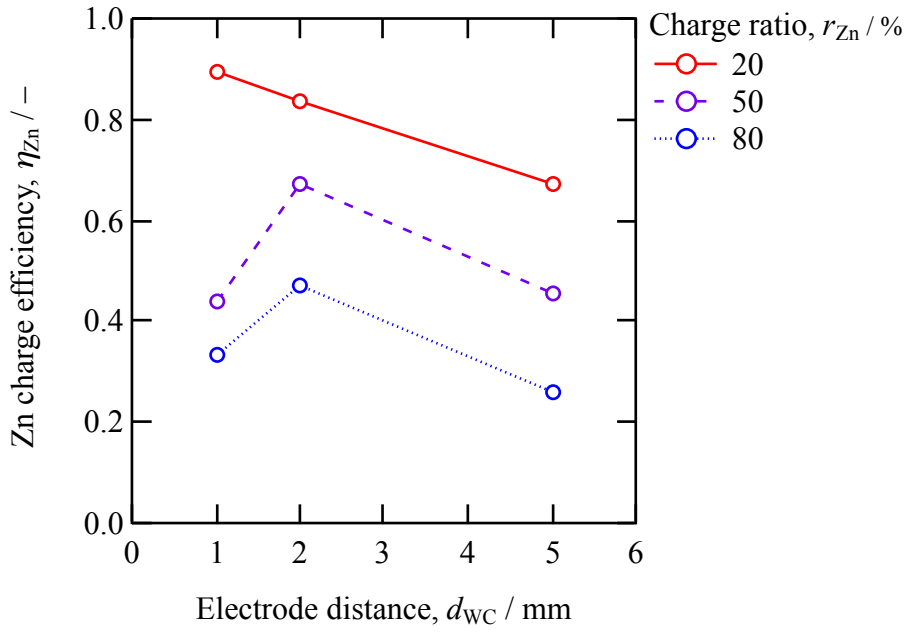


Fig. 4-3-6-1. Dependence of Zn electrodeposition efficiency, h_{Zn}, on d_{WC} at different r_{Zn}.

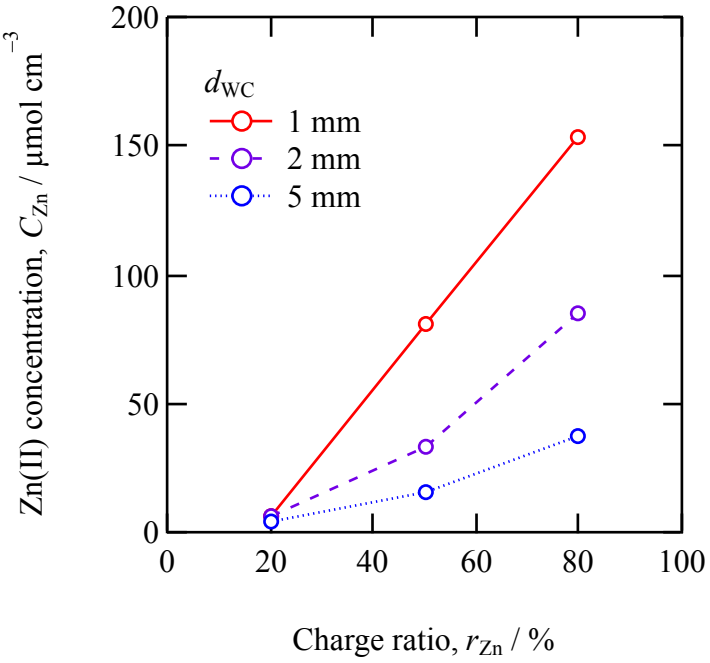


Fig. 4-3-6-2. Concentration of Zn(II) ions in the bath as a function of r_{Zn} and d_{WC} after electrodeposition at j_C = 5 mA cm^{-2} calculated from the Zn content in the deposit, weight gain deposits and dissolution charge of Zn-CE.

4.4. Discussions

In this study, the three factors of pulse current density (j_C), charge ratio on Zn-CE

(r_{Zn}) and distance between the WE and CEs (d_{WC}) affecting the coating composition were investigated.

4.4.1. Effects of j_C and r_{Zn} on X_{Zn}

For example, averaged X_{Zn} decreased with increase in j_C (Fig. 4-3-3-3). From the viewpoint of redox potential, less noble potential Φ at high j_C promotes the electrodeposition of Al from major complex ions of $Al_2Cl_7^-$ in the bath [13]. On the other hand, the supply of Zn complex ions is limited due to the insufficient transportation rate from the Zn-CE to WE via the IL bath at high j_C. Therefore, the decrease in X_{Zn} with increase in j_C shown in Fig. 4-3-3-3 seems to be reasonable. The effect of r_{Zn} on X_{Zn} shown in Fig. 4-3-4-1 also looks straightforward, *i.e.*, X_{Zn} increases with increase in r_{Zn} due to an increase in the concentration of Zn complex ions in the bath dissolved from Zn-CE.

4.4.2. Effect of d_{WC} on X_{Zn}

Compared with the effects of j_C and r_{Zn}, the effect of d_{WC} on X_{Zn} shown in **Fig. 4-3-3-2** is rather complex. X_{Zn} increases with increase in d_{WC} at $d_{WC} < 2$ mm and decreases with increase in d_{WC} at $d_{WC} > 2$ mm. To interpret these phenomena, transport mechanism of Zn and Al ions in the bath from Zn-CE or Al-CE to WE is considered as schematically shown in **Fig. 4-4-2-1**. In the figure, dissolution of metal on a Al-CE or Zn-CE and electrodeposition of metal on a WE are separately described for Al and Zn system. In both cases, metal complex ions are decomposed to form metal deposits on the WE by cathodic reduction and leave free Cl^- ions in the IL bath. Free Cl^- ions seem to be immediately consumed by $Al_2Cl_7^-$ to form an $AlCl_4^-$ complex. Actually, the Cl^- ions exist as a ligand to the metal complex, and the Cl^- ion concentration affects the averaged coordination number of Cl^- ions to the metal that is actually the polymerization number of complexes. On a CE, dissolved metal ions consume Cl^- ions to form complex supplied from the other complexes. Since formation and consumption of Cl^- ions occur on WE and CE, respectively, a concentration gradient of Cl^- ions evolves from WE to CE surfaces in the bath depending on the current density. This means that the concentration of metal complexes changes from the major species of $Al_2Cl_7^-$ and $Zn_3Cl_7^-$ to others such as $AlCl_4^-$, $Zn_2Cl_5^-$ or $ZnCl_3^-$ depending on the distance from the

electrode suface. Depletion of Cl^- ions on the CE may also cause an increase in the overpotential for metal dissolution on the CE to promote side reactions and thus to reduce the coulometric efficiency η at high r_C as seen in Fig. 4-3-5-1. Contrary, excess amount of Cl^- ion may cause transformation of $Al_2Cl_7^-$ to $AlCl_4^-$ on the WE. It decreases the amount of Al deposition and leads increase in overpotential for Al deposition on WE. Both two factors that affecting the overpotential may provide non-rectangular potential response especially at the narrow d_{WC} = 1mm shown in Fig. 4-3-1-1.

At the initial stage of electrodeposition, $Al_3Cl_{10}^-$ is formed on both Al-CE and Zn-CE due to concentration of Al^{3+} and Cl^- in the bath and increase of cations at the surface of CE. On the WE, Al electrodeposits because Zn ions are not supplied. Then when Zn is

Since $Al_2Cl_7^-$ is one of the major species of the IL bath, it is sufficiently supplied to the WE surface for electrodeposition. Therefore, one of the main factors determining the composition of deposits is the rate of supply of Zn ions to the WE surface. When Zn ions reach the WE surface, they are predominantly electrodeposited due to their nobler redox potential than that of Al. **Fig. 4-4-2-2** shows a scheme of the transportation of Zn ions from the Zn-CE to WE *via* the IL bath.

In the cell with a large distance between a CE and a WE as d_{WC} = 5 mm used in the present study, transportation of Zn ions occurs *via* a cascade process of diffusion on the CE surface / convection (flowing state) in the bulk of the bath / diffusion on the WE surface. For example, metal dissolution may change the local density of liquid in the vicinity of the CE surface to cause a downstream flow of heavy liquid. This phenomenon is observed for a dissolving electrode immersed in an aqueous electrolyte solution. Gas bubbling due to the decomposition of water can be another origin of liquid stirring. The convection also thins the diffusion layer on the electrodes and mitigates the diffusion limitation of ion transportation.

When d_{WC} was reduced to 2 mm, transportation rate increased with decrease in the distance between two electrodes. This enabled rapid arrival of Zn ions to the WE surface to contribute to the increase of X_{Zn} in the deposits, as shown in Fig. 4-3-3-2. Lower X_{Zn} at d_{WC} = 5 mm than that at d_{WC} = 2 mm was also caused by the larger volume of the IL bath for the former resulting in dilution of Zn complex ions.

	Al	Zn
CE	Anodic dissolution: $Al + 4Cl^-$ $\rightarrow AlCl_4^- + 3e^-$	Anodic dissolution: $Zn + 3Cl^-$ $\rightarrow ZnCl_3^- + 2e^-$
Bath	Equilibrium $2AlCl_4^- \rightleftarrows Al_2Cl_7^- + Cl^-$ $2ZnCl_3^- \rightleftarrows Zn_2Cl_5^- + Cl^-$ $ZnCl_3^- + Zn_2Cl_5^- \rightleftarrows Zn_3Cl_7^- + Cl^-$:	
WE	Electrodeposition: （多量体が電析可） $Al_2Cl_7 + 3e^-$ $\rightarrow Al + AlCl_4^- + 3Cl^-$	Electrodeposition: $Zn_3Cl_7^- + 2e^-$ $\rightarrow Zn + Zn_2Cl_5^- + 2Cl^-$ $Zn_2Cl_5^- + 2e^-$ $\rightarrow Zn + ZnCl_3^- + 2Cl^-$

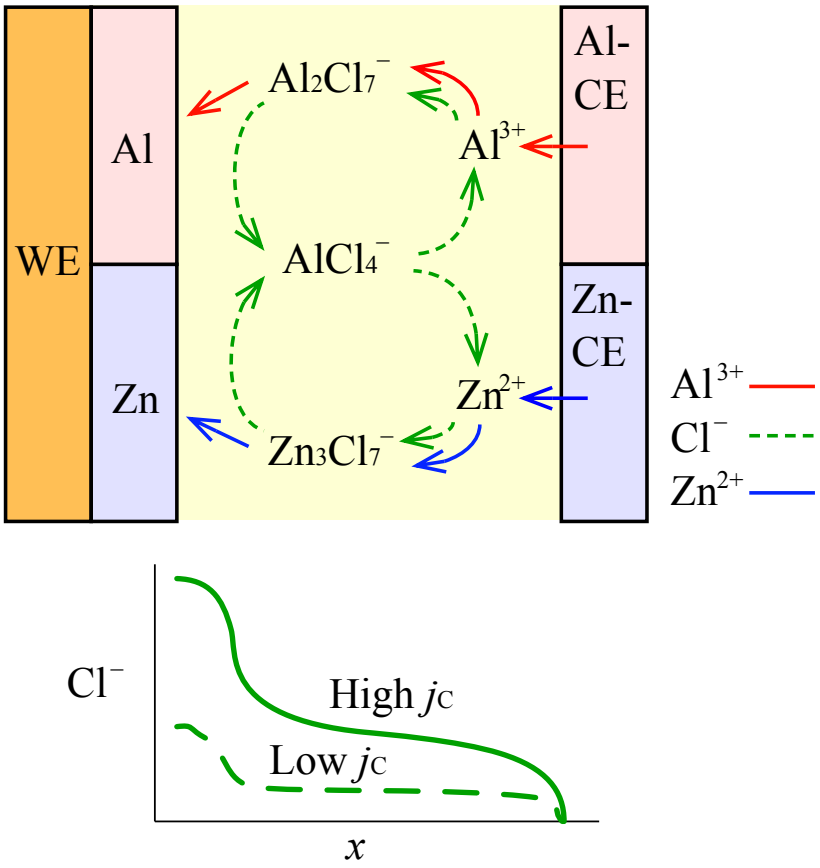


Fig. 4-4-2-1. Schematic illustration of ionic transportation and Cl^- ions profile in the bath.

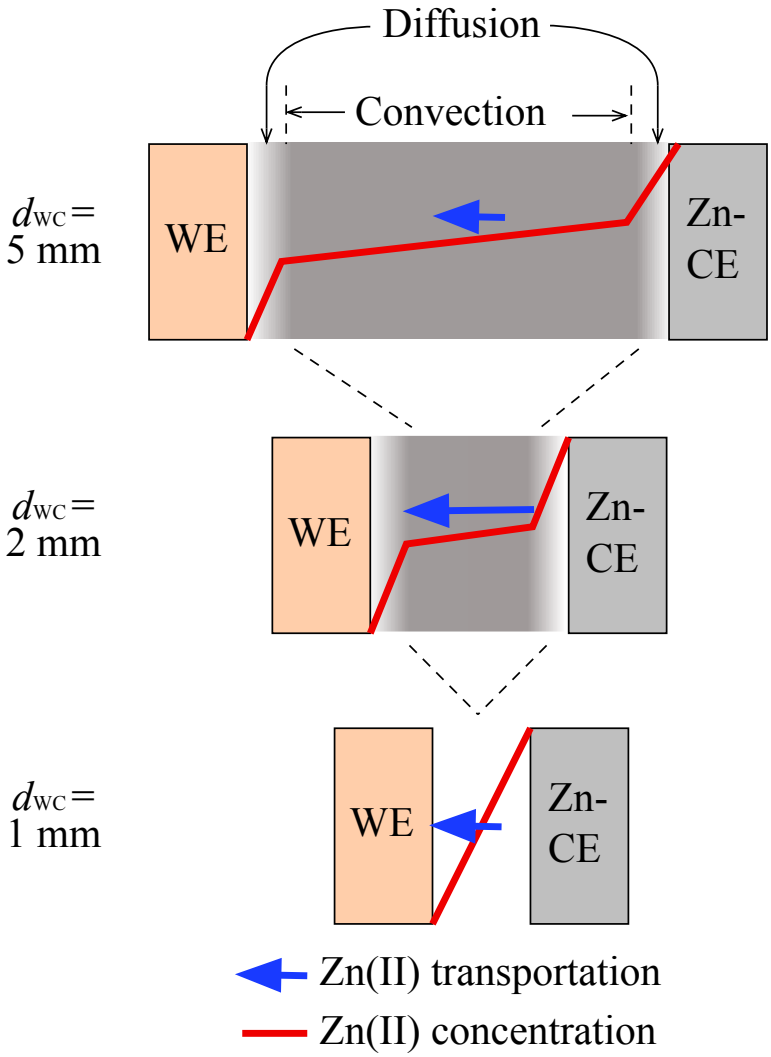


Fig. 4-4-2-2. Transportation mechanism of Zn complex ions functioned on the d_{WC} through the bath affecting the X_{Zn} in the electrodeposits.

When d_{WC} was further reduced to d_{WC} = 1 mm, amount of dissolved Zn^{2+} may affect directly to the composition of deposits because of small volume of electrolyte bath. However, the convection layer could no longer be maintained in a very thin IL bath. Higher viscosity of the IL bath than the aqueous solution bath also contributes to annihilation of the convection layer. In this condition, transportation of Zn complex ions is mainly by diffusion *via* the whole path from the CE to WE and allows spatial re-distribution of ionic species in the bath. This reduces the rate of supply of Zn complex ions to the WE surface, resulting in smaller X_{Zn} than that at d_{WC} = 2 mm until the system reaches a steady state.

The above discussion is applicable for the steady state of dissolution on a CE and

deposition on a WE, while the results presented in this paper are for the transition from an initial state to a steady state. Although not all results can be explained by the model proposed here, it was confirmed that the DCES can provide flexibility and wide composition controllability for alloy coatings.

4.4.3 Transport mechanism of metal ions in a stagnant thin electrolyte IL bath

In this work, a thin electrolyte cell shown in **Fig. 4-4-3-1** was used in which a Al-RE was located close to the CEs. In this arrangement, the potential measured by the Al-RE is close to the potential of CEs rather than WE. This situation resembles to the two electrode system composed of working electrode and counter electrode except for that the measured potential by Al-RE differs from that of CE.

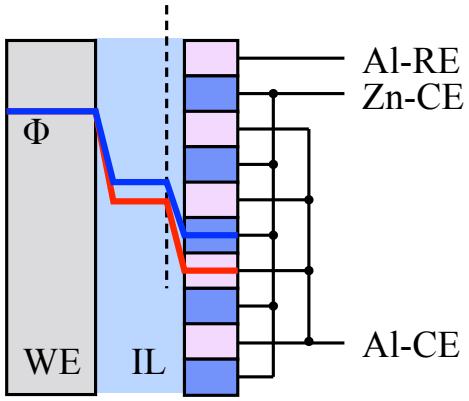


Fig. 4-4-3-1. Arrangement of electrodes in a thin electrolyte cell used in this study.

As discussed above the mass transportation mechanism depends on the thickness of a thin electrolyte phase and rapid transfer rate was obtained at d_{CW} = 2 mm from the contribution both of convection and diffusion processes. At d_{CW} = 1 mm, it was suggested that only diffusion process contributes to the mass transportation. In the following discussion, the mass-transport mechanism will be examined from the transitional potential response. **Fig. 4-4-3-2** shows again the transition of polarization potential under galvanostatic pulse electrodeposition with the pulse number. Electrodeposition pulse was applied as a repetition of [5 pulse for Zn-CE, 5 pulse for Al-CE] (d_{WC} = 1 mm, j_C = –10 mA cm^{-2}, t_{on} =1 s, t_{off} = 1 s). The shape of potential transition changes with progress of electrodeposition. The potential changes in a long span, *i.e.*, increases in the lowest potential around 1800 - 2000 s seems to be induced by the change in bath composition from initial EMIC(1/3 in molar

ratio)-$AlCl_3$(2/3) to EMIC-$AlCl_3$-$ZnCl_2$.

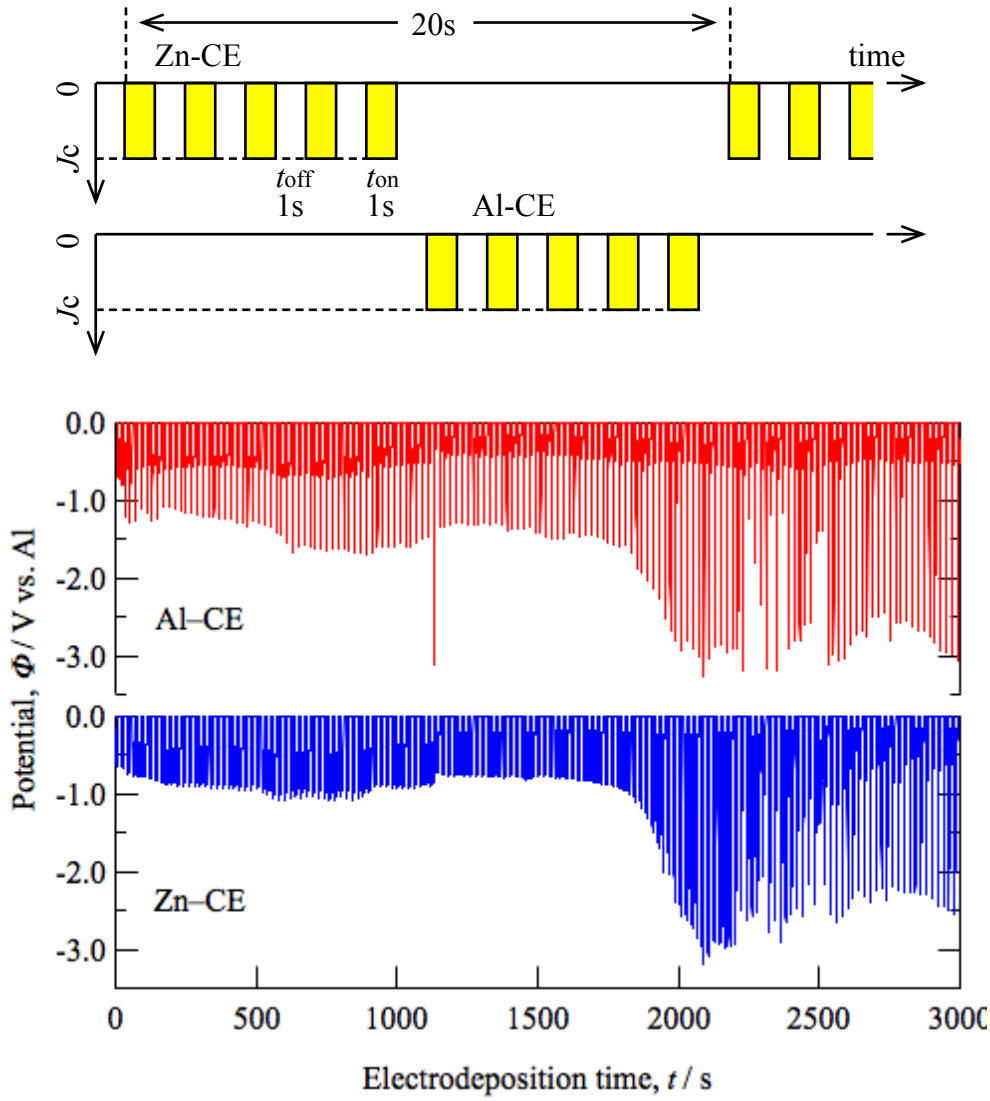


Fig. 4-4-3-2. Transition of the polarization potential F during the pulse electrodeposition in the condition of J_C = –10 mA cm^{-2}, t_{on} = 1 s, t_{off} = 1 s, d_{WC} = 1 mm) plotted separately for Al-CE and Zn-CE, respectively (Duplicate of Fig.4-3-1-2).

Typical potential transitions to a galvanostatic pulse were manipulated as shown in **Fig. 4-4-3-3**(a) for Al-CE and **Fig. 4-4-3-3**(b) for Zn-CE, respectively. In Fig. 4-4-3-3(a) for Al-CE, followings are observed; (1) potential Φ shifts in a cathodic direction during galvanostatic polarization, (2) potential-time response to the current pulse changes from rectangle to spike or falciform with cycling time, (3) large potential shift was found at the initial pulse for 200, 1000 and 1250 cycle, (4) the rest potential at t_{off} depends on the time, indicating that the composition of the bath on the Al-RE differs from that on Al-CE. Similar

analysis was done on the results for Zn-CE shown in Fig. 4-4-3-3(b) and considerable difference was confirmed comparing with the result of Al-CE shown in Fig. 4-4-3-3(a). To clarify the difference of potential response of Al-CE and Zn-CE, four responses were chosen and plotted separately in **Fig. 4-4-3-4**. These for potential response may be categorized into three types (A, B, C) as shown in **Fig. 4-4-3-5** and each type is assigned to the selected results of potential response shown in Fig. D in the right side of the plots, although some of the other response are mixture of these types.

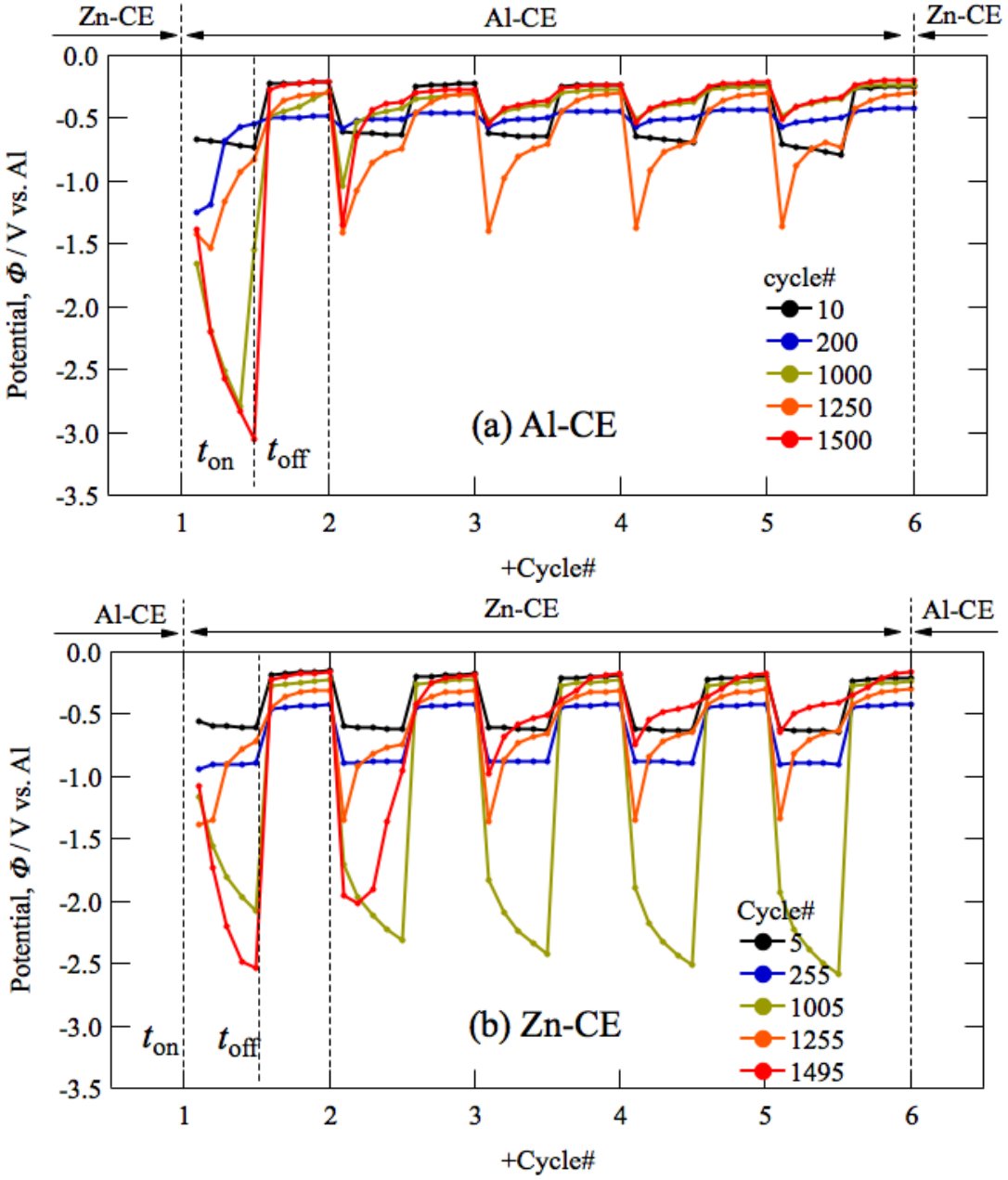


Fig. 4-4-3-3. Selected potential response to five galvanostatic polarization pulse (J_C = –10 mA cm^{-2}, t_{on} = 1 s, t_{off} = 1 s, d_{WC} = 1 mm) for Al-CE (a) and Zn-CE (b), respectively. Sampling rate was 10 s^{-1}.

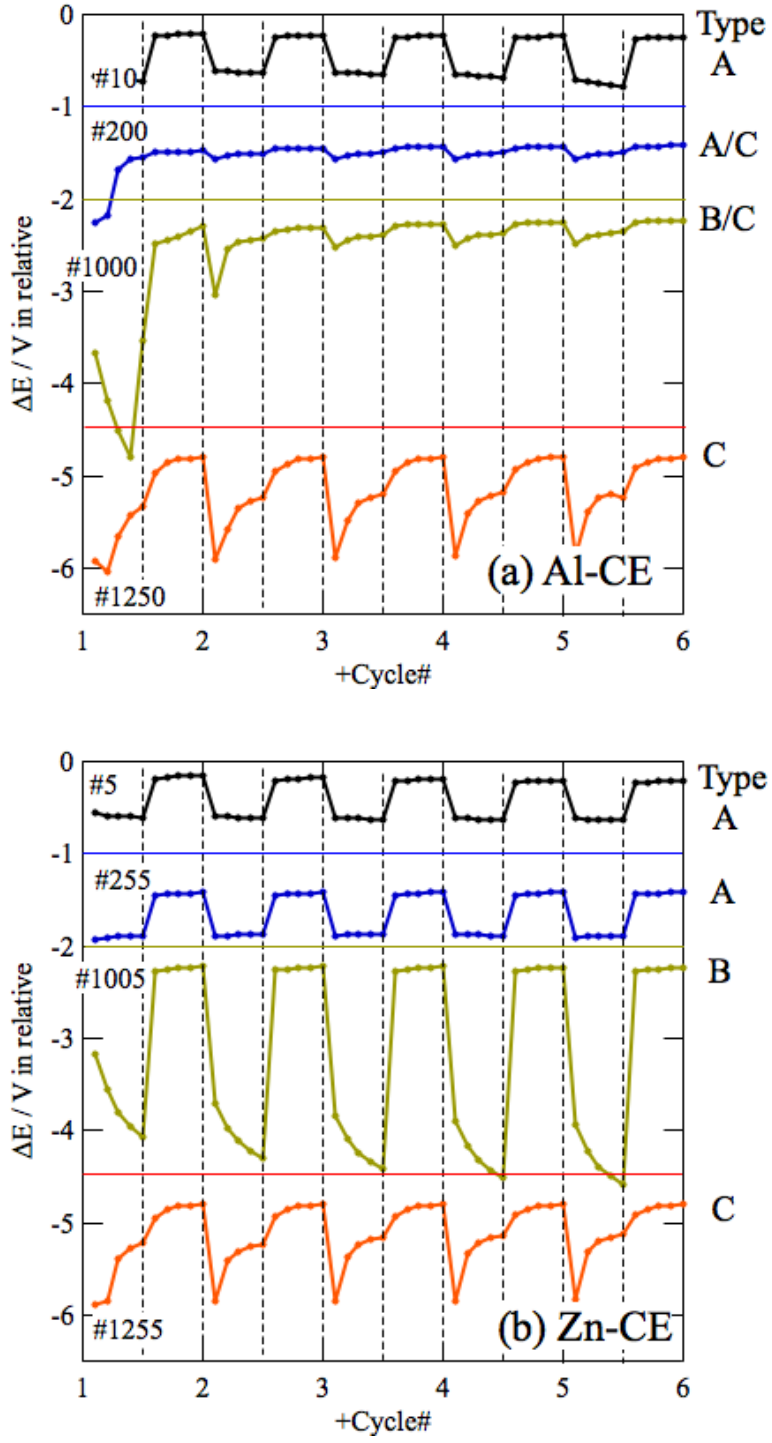


Fig. 4-4-3-4. Re-plot of the data of Fig. 4-4-3-3 to present each response separately. The vertical axis shows relative potential difference. Each potential response is referred to the zero value presented by straight line with same color.

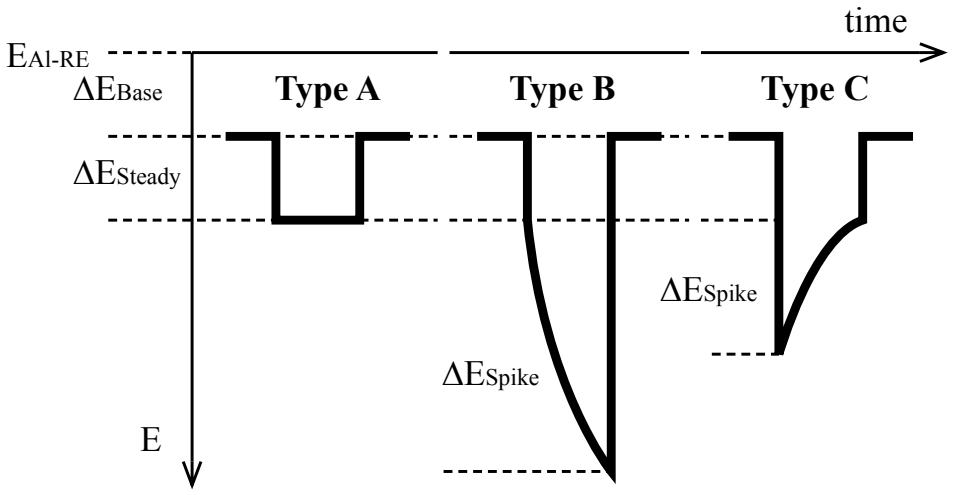


Fig. 4-4-3-5. Re-plot of the data of Fig. C to present each response separately.

Type A: Found in the initial potential response of Al-CE and Zn-CE. In this stage, The bath composition is EMIC(1/3) and $AlCl_3$(2/3). This means that the Al(III) complex is mainly $Al_2Cl_7^-$ and thus Al can be easily electrodeposited on WE.

Al electrodeposition on WE:

(1) $Al_2Cl_7^- + 3e^- \rightarrow Al + 3Cl^- + AlCl_4^-$

On Al-CE, however, dissolved Al^{3+} must be stabilized by forming complex with Cl^- as

Al dissolution on Al – CE:

(2) $Al \rightarrow Al^{3+} + 3e^-$

(3) $Al^{3+} + 4Cl^- \rightarrow AlCl_4^-$

(4) $Al^{3+} + 3Cl^- + AlCl_4^- \rightarrow Al_2Cl_7^-$

(5) $Al^{3+} + 3Cl^- + Al_2Cl_7^- \rightarrow Al_3Cl_{10}^-$

(6) $Al^{3+} + 10\,Al_2Cl_7^- \rightarrow 7\,Al_3Cl_{10}^-$

:

Reactions (3)-(5) requires Cl^- ions from WE formed by reaction (1) which may be yet reach the Al-CE surface. On the other hand, reaction (6) could proceed because much $Al_2Cl_7^-$ complex ions exists in the initial bath. Higher polymerization $Al_nCl_m^-$ complex may be also possible in high concentrated ionic liquid bath [14,15]. In other words, ionic liquid bath containing dense $Al_2Cl_7^-$ complex ions acts as a large reservoir of Cl^- ions to accept further dissolved metal ions by complex formation. In this condition the potential transition show

simply the rectangle form (Type A) with overpotential ΔE_{Steady} of dissolution reaction because only charge transfer resistance becomes obvious in the electrochemical dissolution process. Same condition can be proposed to the Zn-CE as

Zn dissolution on Zn – CE:

(7) $Zn \rightarrow Zn^{2+} + 2e^{-}$

(8) $2Zn^{2+} + 15Al_2Cl_7^{-} \rightarrow 10Al_3Cl_{10}^{-} + Zn_2Cl_5^{-}$

:

Higher polymerized $Zn_mCl_n^{-}$ complex may also be possible in high concentrated ionic liquid bath [15].

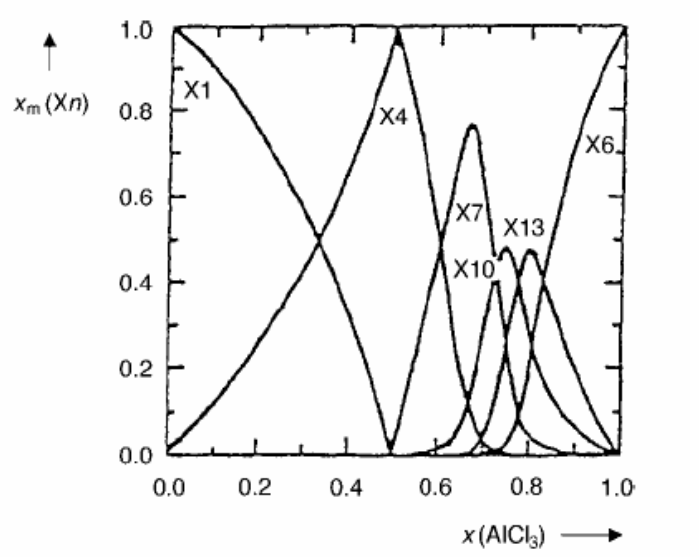


Figure 1.9. Mole fraction x_m of different anion species Xn in choroaluminates melts ($X1=Cl^{-}$; $X4=AlCl_4^{-}$; $X7=Al_2Cl_7^{-}$; $X10=Al_3Cl_{10}^{-}$;$X13=Al_4Cl_{13}^{-}$; $X6=Al_2Cl_6$).

Reprint from Ref. 14

Type B: Found in the initial pulse for Al-CE at #1000 cycle and for Zn-CE continuing after #1005 cycle. Gradual increase of the overpotential for dissolution reaction indicates that dissolution of metal ions from CE becomes difficult because free Cl^{-}, mono-complex ($AlCl_4^{-}$) or dimeric complex ($Al_2Cl_7^{-}$) depletes near the CE surface and thus complex formation of dissolved Al^{3+} (6) or Zn^{2+} (8) ions does not easily proceed. Increase in overpotential raised the electric field near the CE surface and accelerates electrophoretic migration of these species to maintain the dissolution reaction under galvanostatic polarization. In the rest period (t_{off}), concentration of these species near the surface recovered by migration / diffusion from the bulk of the bath and thus the overpotential at the start point

in the next pulse becomes small (solid arrows in **Fig. 4-4-3-6(a)**). However, the depletion of these species progresses with repetition of current pulse for Zn-CE dissolution and thus the overpotential on Zn-CE increases with pulse number (arrow with broke line). The difference in the potential transition between Al-CE (**Fig. 4-4-3-6(b)**) and Zn-CE (**Fig. 4-4-3-6(a)**) is reflected by the buffering ability of Al complex and non-buffering ability of Zn complex as Cl^- reservoir, as discussed below. In case of Al-CE, dissolved Al(III) ions join the complexes which can act as Cl^- reservoir and thus the overpotential after the first current pulse decreases.

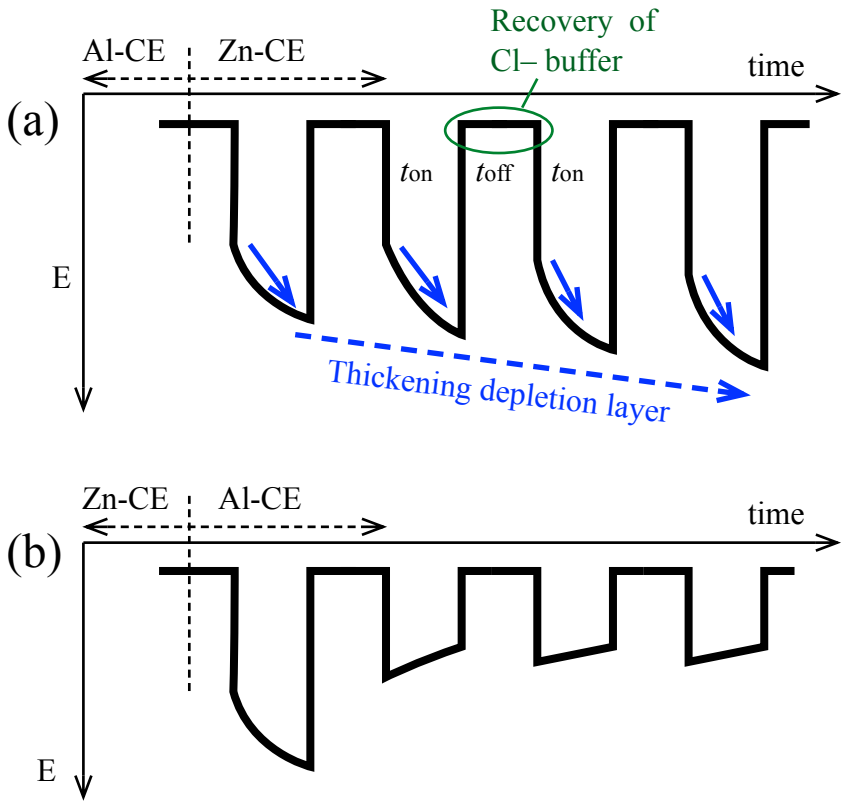


Fig. 4-4-3-6. Schematic presentation of Type B potential response for Zn-CE(a) and Al-CE(b).

Type C: Found in the final stage for Al-CE and Zn-CE. In this stage bath composition seems to reach a steady state of Al[III] and Z[II] species, *i.e.*, concentration of $Al_2Cl_7^-$ decreases and that of $Zn_2Cl_5^-$ increases. Role of Zn chloride differs from that of Al chloride that the reactions to provide Cl^- ions for new complex formation such as

$$(9)\ 2Al^{3+} + 14ZnCl_3^- \rightarrow Al_2Cl_7^- + 7Zn_2Cl_5^-$$

$$(10)\ 4Al^{3+} + 42Zn_2Cl_5^- \rightarrow 2Al_2Cl_7^- + 28Zn_3Cl_7^-$$

$$(11)\ 2Zn^{2+} + 10ZnCl_3^- \rightarrow 6Zn_2Cl_5^-$$

$$(12)\ 3Zn^{2+} + 21Zn_2Cl_5^- \rightarrow 15Zn_3Cl_7^-$$

:

are difficult to proceed. The spike type potential transition seems to be reflected by the absence of buffer ability of the bath for Cl^- ions. However, drop of the overpotential after the spike indicates the relaxation of tightened supply of Cl^- necessary for complex formation. This relaxation occurred after *ca.*1200 cycle (2400 s) and repeated every pulse cycle (**Fig. 4-4-3-7**) indicating that the source of this relaxation came from the bath composition. The origin of this relaxation is probably due to the side reaction of electrodeposition. As seen in Fig. 4-3-5-1, electrodeposition efficiency at d_{WC} = 1mm is around 80% and thus the electric charge loss was consumed by, for example, decomposition of EMI molecule at high overpotential condition in the Type B response as seen in **Fig. 4-4-3-4** and provided excess Cl^- ions to the bath.

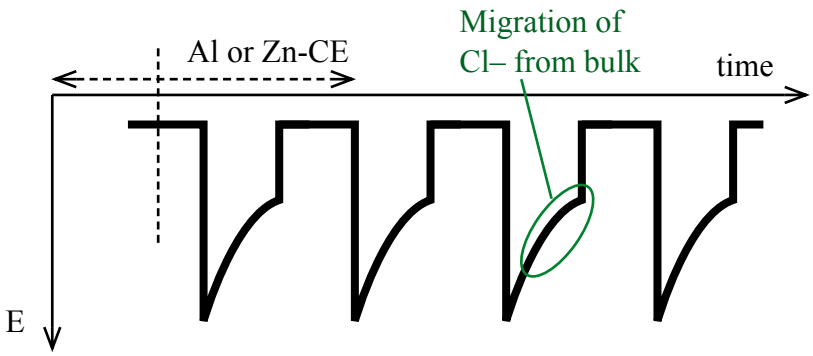


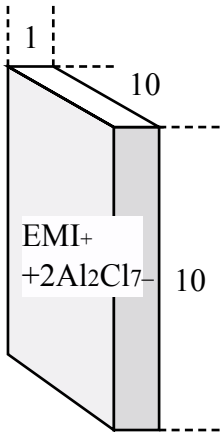
Fig. 4-4-3-7. Schematic presentation of Type C potential response.

In **Fig. 4-4-3-4(a)** at #1005 series of Al-CE current pulse, an initial pulse is enough to mitigate the depletion of Cl^- supply for the following dissolution pulses. Assuming reaction (6) for Al^{3+} dissolution on Al-CE in which dissolution of one Al^{3+} requires 10 x ($EMI^+ + Al_2Cl_7^-$ complex), and a probable density of ionic liquid bath of EMIC-$2AlCl_3$ (*i.e.*, EMI + $Al_2Cl_7^-$ complex) as ρ = 1.4 g cm^{-3}, that is provided by company (Sigma-Aldrich Co.) for EMIC-$3AlCl_3$ (*i.e.*, EMI + $Al_3Cl_{10}^-$ complex) instead, Al^{3+} dissolution at one current pulse (q_C = –10 mA cm^{-2} x 1 s = 0.01 C) corresponds to 3.06 μm in thickness of IL bath at the Al-CE surface. This looks fairly rapid for transportation of $Al_2Cl_7^-$ species in a stagnant electrolyte of a thin layer bath. In the EMIC-x$AlCl_3$ bath, however, transportation of Al(III)

ions can be achieved by the cascade exchange of $AlCl_3$ between the complexes with different polymerization number, as shown in **Fig. 4-4-3-8**. In this figure, $AlCl_3$ is transported sequentially by $Al_2Cl_7^-$ complexes in the form of intermediate $Al_3Cl_{10}^-$ complex ($AlCl_3 \bullet Al_2Cl_7^-$). When Al(III) discharges on WE surface, Cl– is released to form, for example, $AlCl_4^-$ from $Al_2Cl_7^-$. Because of anionic property of Al^{3+} complexes, negative electric field from CE surface to WE surface tends to prevent the electrophoretic migration of complexes ascending the field. Fortunately, high charge density of ionic liquid disables electric field in a bulk of the bath and applied potential difference appears only at the interface of WE/IL and IL/CE. As a result substantial transportation of $AlCl_3$ can be regarded as a migration of Al(III) from Al-CE to WE in a EMI^+-$Al_2Cl_7^-$ (or other complex) matrix medium with concentration distribution of Cl^- ions, as shown in **Fig. 4-4-2-1**.

Al dissolution on Al – CE:

(6) $Al^{3+} + 10\,Al_2Cl_7^- \rightarrow 7\,Al_3Cl_{10}^-$



From the discussion above, followings should be noted to design bath composition and electrodeposition condition using a thin electrolyte cell. In case of Zn-CE, lacking of buffer ability of Zn(II) complex for Cl^- ions reduces the range of proper operation condition of plating process such as electrodeposition current and concentration of Zn in the resultant deposits. Increase in an overpotential on Zn-CE also may cause decomposition of ionic liquid.

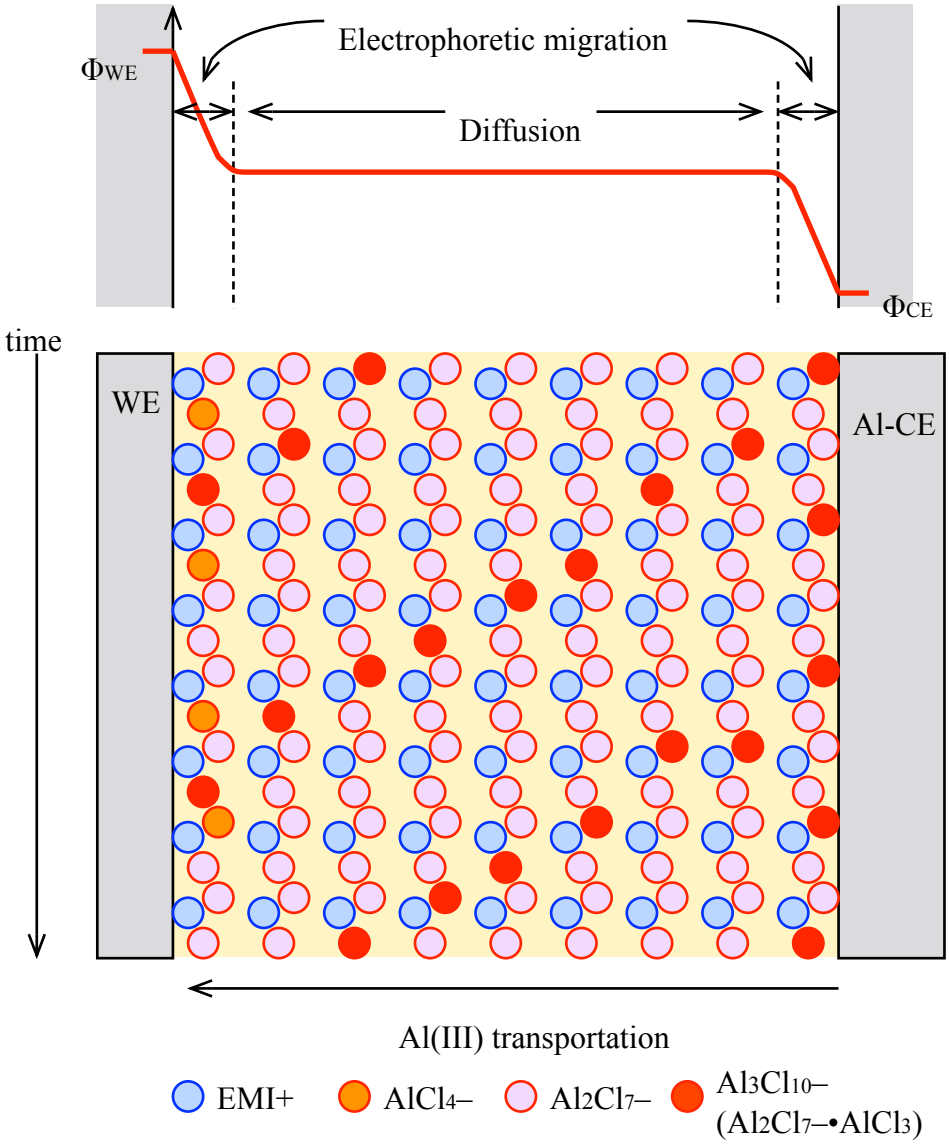


Fig. 4-4-3-8. Probable transportation model of Al(III) from Al-CE to WE through the matrix of ionic liquid bath.

4.5. Conclusions

In this work, a DCES was developed and applied to co-electrodeposition of Al-Zn coatings in an ionic liquid bath to evaluate its performance for control of coating composition. The results showed that the composition of coatings was influenced by deposition conditions including current density, charge ratio of active Al and Zn counter electrodes, and distance between the counter electrodes and working electrodes. Composition of coatings close to the theoretical value predicted from the charge ratio was obtained. Rapid response for changing the coating composition by changing the charge ratio was expected for a small volume of the bath. To confirm this the dependence of coating composition on the distance between the

counter and working electrodes was investigated. The results indicated that the coating composition reflects the transition of the transport mechanism of metal complex ions in the bath depending on the distance. Detailed analysis of galvanostatic pulse polarization deposition clarified the importance of dissolution process on CE. Buffering ability of bath species (metal-Cl^- complexes) as Cl^- reservoir has an important role in the successive metal dissolution on CE and transport of metal ions from CE to WE.

References

[1] T. Prosec, D. Persson, J. Stoulil, D. Thierry, Composition of corrosion products formed on Zn–Mg, Zn–Al and Zn–Al–Mg coatings in model atmospheric conditions, *Corrosion Science* **86** (2014) 231-238.

[2] H.C. Shih, J.W. Hsu, C.N. Sun, S.C. Chung, The lifetime assessment of hot-dip 5% Al–Zn coatings in chloride environments, *Surface Coatings and Technology* **150** (2002) 70-75.

[3] P.R. Seré, M. Zapponi, C.I. Elsner, A.R. Di Sarli, Comparative corrosion behaviour of 55Aluminium–zinc alloy and zinc hot-dip coatings deposited on low carbon steel substrates, *Corrosion Science* **40** (1998) 1711-1723.

[4] D. Laverde, j.C. Zubillaga, J.G. Sevillano, E. Vilaueva, The influence of the primer layer on mechanical damage and loss of corrosion protection of deformed painted Zn-0.16% Al and Zn-5% Al galvanized sheet steel, *Corrosion Science* **37** (1995) 79-87, 89-95.

[5] R. Sagl, A. Jarosik, D. Stifter, G. Angeli, The role of surface oxides on annealed high-strength steels in hot-dip galvanizing, *Corrosion Science* **70** (2013) 268-275.

[6] G.M. Song, T. Vystavel, N. van der Pers, J.Th.M. De Hosson, W.G. Sloof, Relation between microstructure and adhesion of hot dip galvanized zinc coatings on dual phase steel, Acta Mater. **60** (2012) 2973-2981.

[7] S. Prabhudev, S. Swaminathan, M. Rohwerder, Effect of oxides on the reaction kinetics during hot-dip galvanizing of high strength steels, *Corrosion Science* **53** (2011) 2413-2418.

[8] Q.X. Liu, S. Zein El Abedin, F. Endres, Electroplating of mild steel by aluminium in a

first generation ionic liquid: A green alternative to commercial Al-plating in organic solvents, *Surface Coatings and Technology* **201** (2006) 1352-1356.

[9] Y.F. Lin, I.W. Sun, Electrodeposition of zinc from a Lewis acidic zinc chloride-1-ethyl-3-methylimidazolium chloride molten salt, *Electrochimica Acta* **44** (1999) 2771-2777.

[10] J.K. Chang, S.Y. Chen, W.T. Tsai, M.J. Deng, I.W. Sun, Electrochem. Commun. **9** (2007) 1602-1606.

[11] T. jiang, M.J. Chollier Brym, G. Dubé, A. Lasia, G.M. Brisard, *Surface Coatings and Technology* **201** (2006) 1-9.

[12] S.I. Hsiu, J.F. Huang, I.W. Sun, C.H. Yuan, J. Shiea, *Electrochimica Acta* **47** (2002) 4367-4372.

[13] S.J. Pan, W.T. Tsai, J.K. Chang, I.W. Sun, *Electrochimica Acta* **55** (2010) 2158-2162.

[14] M. Ueda, Y. Tabei, T. Ohtuska, *ECS Transactions* **33** (2010) 563-570.

[15] Wasserscheid, P. and Keim, W., *Angew. Chem. Int*. (Ed.) 2000, 39, 3772- 3789. "*Ionic Liquids—New "Solutions" for Transition Metal Catalysis*"

[16] *Electrodeposition from Ionic Liquids*, F. Endres, D. MacFarlane, A. Abbott (Eds.), John Wiley & Sons, Inc., New Jersey, (2008). ISBN: 978-3-527-31565-9

Chapter 5. Summary

Corrosion protection of metals, monitoring, assessment and management of corrosion progress of them are the contemporary issues to maintain and further development of modern civilization. In this study, corrosion behavior and protection mechanism of ordinal zinc-galvanized steel were investigated by using multi-channel electrode technique to enable visualization of spatial distribution of anodic and cathodic reacting area and rate *in-situ*, and new electrodeposition method was explored to realize the high performance and material-resource saving corrosion protection alloy coatings using recently developed ionic liquid bath and a double-counter electrode method proposed by author to control the coating composition more flexibly than the conventional electrodeposition method. Achievement in each chapter of this thesis is described as followings.

In chapter 1, the general mechanism of corrosion especially non-uniform corrosion was described. Also a brier introduction of corrosion inhibition and manufacturing process of galvanized steel was presented. Based on the issue for evaluating non-uniform corrosion and manufacturing galvanic coatings, the objectives of this study are given in this chapter.

In chapter 2, to evaluate non-uniform corrosion of partially zinc coated galvanized steel, 100-multichannel electrode coupling current measurement system was developed. This system consists of electric circuit, microcontroller and 100-Fe wire electrode array to visualize spatial distribution of anodic and cathodic reaction on the steel substrate. Corrosion inhibition effects especially derived by zinc corrosion products were investigated by this system, indicating that Zn coating consumed preferentially at the edge of coating. The inhibition effect of corrosion products was observed at underneath of hydrozincite and simonkolleite corrosion products by calculating coupling charge during corrosion test.

In chapter 3, the fundamental of co-electrodeposition of Al-Zn from $AlCl_3$-$ZnCl_2$-EMIC was investigated. The deposition potential affect both composition of Al-Zn and structure of deposits in the coating. The noble deposition potential leads high Zn composition in the coatings. The electrodeposits consist of metallic Zn and Al. The heat treatment for electrodeposits at 350ºC, at which is lower than hot-dip process, generate $Al_{0.403}Zn_{0.597}$ alloy.

In chapter 4, the double counter electrode electrodeposition system was developed to realize arbitral electrodeposition of two elements, and was applied to the electrodeposition of Al-Zn from an $AlCl_3$-1-ethyl-3-methylimidazolium chloride ionic liquid bath. As a result, the composition of co-electrodeposits depends on the current density, total charge passing through counter electrodes, and electrodes distance. Especially, the distance between working

and counter electrodes have optimal distance to control the composition of co-electrodeposits arbitrarily.

These results shown in chapter 2 contribute to evaluate non-uniform corrosion, declare non-uniform corrosion phenomena. The results displayed in chapter 3 and 4 contribute to develop new method of co-electordeposition of metal, especially less noble metals.

Acknowledgement

I am grateful to Dr. Prof. Hiroki Habazaki for discussing phenomena caused on corroded surface. I appreciate Dr. Prof. Kei Murakoshi for discussing for electrochemical phenomena in ionic liquid bath. I am thankful to Dr. Associate Prof. Hitoshi Koizumi for his advise for designing electrodeposition bath containing organic materials. I am grateful to Dr. Associate Prof. Koji Fushimi for discussion of microelectrode effect. I am grateful to Dr. Prof. Mikito Ueda for advising for treatment of ionic liquid and electrodeposition from it. I appreciate Dr. Associate Prof. Masatoshi Sakairi, for his advice to improve electrodeposition method. I appreciate Dr. Assistant Prof. Atsushi Hyono for his support for evaluation and analysis of Raman spectroscopy. I appreciate all laboratory members for their daily discussion and advise for this study.

A part of this work in Chapter 4 was supported by the Japan Aluminium Association. In addition, this work was supported by the "Nanotechnology Platform" program of the Ministry of Education, Culture, Sports, Science and Technology (MEXT), Japan.

Finally, I am great thankful for Dr. Prof. Kazuhisa Azumi for his discussion, advise and support for whole part of this thesis.